

**IMPROVEMENT OF FLOW UNIFORMITY AND  
MODELING OF FILTRATION EFFICIENCIES  
FOR AUTOMOTIVE AIR FILTER  
TEST HOUSINGS**

**By**

**ROBERT DURAN**

**Bachelor of Science**

**The University of Texas**

**Austin, Texas**

**1993**

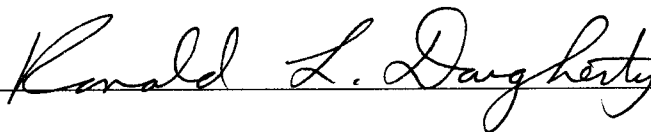
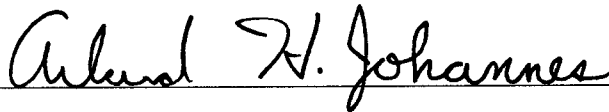
**Submitted to the Faculty of the  
Graduate College of the  
Oklahoma State University  
in partial fulfillment of  
the requirements for  
the Degree of  
MASTER OF SCIENCE  
July, 1995**

**IMPROVEMENT OF FLOW UNIFORMITY AND  
MODELING OF FILTRATION EFFICIENCIES  
FOR AUTOMOTIVE AIR FILTER  
TEST HOUSINGS**

**Thesis Approved:**



**Thesis Adviser**



**Dean of the Graduate College**

## ACKNOWLEDGMENTS

I wish to express my sincere appreciation to all of the individuals who were kind enough to assist me in completing this project. First, I would like to thank my major advisor, Dr. F.W. Chambers, for his guidance, support, and confidence in me. Thank you for always finding the time. I would also like to thank my other committee members, Dr. R.L. Dougherty, Dr. J.D. Spitler, and Dr. A.J. Johannes for their helpful advice and encouragement throughout my graduate studies.

I would like to thank all of my colleagues and friends at the university who were always willing to drop what they were doing to assist me. A sincere thanks goes to Dr. Jiaqi Cai and Rich Burgess for their continual help, friendship, and encouragement throughout my career as a graduate student. I would also like to thank my other colleagues, R.A. Newman, F. Liang, C. Tebbutt, Dr. G. Liu, B. Natarajan, and J. Williams for always having the time and not being afraid to get their hands dirty.

The financial support provided by Purolator Products, Inc. and the Oklahoma Center for the Advancement of Science and Technology (OCAST) is greatly appreciated. A special thanks goes to Dr. G. Ferrell and the personnel of Purolator Products, Inc. for their help and insight.

I would like to express my gratefulness to my parents, Felipe and Felicitas Duran, and to my sister and two brothers for their invaluable support and continuous encouragement throughout my life and college endeavors.

## TABLE OF CONTENTS

Chapter	
<b>I</b>	<b>INTRODUCTION..... 1</b>
1.1	Background..... 1
1.2	Objectives, Scope, and Limitations of Present Study..... 3
1.3	The SAE J726 Air Cleaner Test Code..... 5
<b>II</b>	<b>FIBROUS FILTRATION THEORY AND METHODOLOGY ..... 11</b>
2.1	Fibrous Filtration ..... 11
2.2	Fiber Representation and Filtration Efficiencies..... 15
2.2.1	<i>Single Fiber Representation of a Fibrous Filter</i> ..... 15
2.2.2	<i>Flow Around a Fiber</i> ..... 16
2.2.3	<i>Single Fiber Efficiency</i> ..... 17
2.2.4	<i>Isolated Fiber Efficiency</i> ..... 19
2.2.5	<i>Elemental Fiber Efficiency</i> ..... 20
2.2.6	<i>Overall Filter Efficiency</i> ..... 21
2.3	Mechanisms of Particle Capture and Combined Efficiencies ..... 23
2.3.1	<i>Overview</i> ..... 23
2.3.2	<i>Interception</i> ..... 23

2.3.3	<i>Inertial Impaction</i> .....	24
2.3.4	<i>Brownian Diffusion</i> .....	24
2.3.5	<i>Electrostatic Attraction</i> .....	25
2.3.6	<i>Combined Particle Collision Efficiencies</i> .....	25
2.4	<i>Kuwabara Flow Field Around a Fiber Cylinder</i> .....	27
2.5	<i>Filtration Efficiency Models</i> .....	29
2.5.1	<i>Lee and Liu Interception Model</i> .....	29
2.5.2	<i>Landahl and Herrmann Inertial Impaction Model</i> .....	31
2.5.3	<i>Combined Interception and Inertial Impaction Model</i> .....	32
2.5.4	<i>Interception and Inertial Modeling by Particle Trajectory</i> .....	34
2.5.5	<i>Other Collision Efficiency Models</i> .....	36
2.6	<i>Adhesion and Retention of Captured Particles</i> .....	39
2.6.1	<i>Discussion</i> .....	39
2.6.2	<i>Adhesion Forces</i> .....	40
2.6.3	<i>Conditions Affecting Particle Retention</i> .....	43
2.6.4	<i>Ptak and Jaroszczyk Adhesion Model</i> .....	45
2.7	<i>Pleated Air Filters</i> .....	48
2.7.1	<i>Discussion</i> .....	48
2.7.2	<i>Pleated Surface Area</i> .....	49

	2.7.3 <i>Air Velocities Inside Pleated Filter</i> .....	50
	2.7 Methodology.....	51
	2.8.1 <i>Typical Properties of Automotive Air Filtration Paper</i> .....	51
	2.8.2 <i>Fiber Diameter</i> .....	52
	2.8.3 <i>Packing Density</i> .....	54
	2.8.4 <i>Program "EFFMODEL.FOR"</i> .....	58
<b>III</b>	<b>EXPERIMENTAL SETUP</b> .....	<b>64</b>
	3.1 Experimental Apparatus.....	64
	3.2 Laser Doppler Velocimetry Diagnostics.....	66
	3.3 Principles of Laser Doppler Velocimetry.....	69
	3.4 Set-Up and Parameters of Laser Doppler Velocimetry Measurements.....	74
	3.5 Flow Visualizations.....	80
	3.6 Equipment Listing.....	81
<b>IV</b>	<b>RESULTS AND DISCUSSION OF FLOW VISUALIZATIONS AND LASER DOPPLER VELOCIMETRY MEASUREMENTS</b> .....	<b>88</b>
	4.1 Flow Visualizations.....	88
	4.2 Improvement of Flow Distribution.....	92
	4.2.1 <i>Spheres Positioned Near the Housing Inlet</i> .....	92
	4.2.2 <i>Spheres Positioned Upstream of the Filter Specimen</i> .....	96

	4.3 Three-Dimensional Axial Velocity Profiles .....	99
	4.4 Flowrate Comparison of Equally Sized Regions .....	106
	4.5 Three-Dimensional Transverse Velocity Profiles .....	109
	4.6 Turbulence Intensities Upstream of Filter Specimen .....	113
	4.7 Summary of Results .....	115
<b>V</b>	<b>FILTRATION EFFICIENCIES .....</b>	<b>117</b>
	5.1 General Overview .....	117
	5.2 Single Fiber Efficiencies within Pleated Air Filters .....	118
	5.3 Elemental Efficiencies Across Pleated Air Filter Beds .....	122
	5.4 Overall Elemental Efficiencies for the SAE Test Dust Particle Distributions .....	131
	5.5 Summary of Efficiency Results .....	142
<b>VI</b>	<b>SEPARATION AND CONTROL OF THE SAE PANEL FILTER TEST HOUSING .....</b>	<b>144</b>
	6.1 Flow Uniformity in Automotive Air Filter Test Housings .....	144
	6.2 Diffuser Performance and Characteristics .....	146
	6.3 Recommended Test Housing Designs .....	151
<b>VII</b>	<b>CONCLUSIONS AND RECOMMENDATIONS .....</b>	<b>155</b>
	7.1 Conclusions .....	155
	7.2 Recommendations .....	157

<b>REFERENCES</b> .....	158
<b>APPENDICES</b> .....	163
A. PUROLATOR AF3192 AIR FILTER SPECIFICATIONS .....	163
B. SOURCE CODE LISTING OF EFFMODEL.FOR.....	164
C. SAMPLE INPUT/OUTPUT FILES OF EFFMODEL.FOR .....	177
C.1 Sample Input File .....	177
C.2 Sample VELSTRE.OUT File .....	178
C.3 Sample EFFCOMP.OUT File .....	180
C.4 Sample SINGELEM.OUT File.....	181
C.5 Sample SAEDUST.OUT File.....	183
D. SOURCE CODE LISTING OF DATAPICK.FOR FOR DSA OUTPUT ....	185
E. PRELIMINARY CALCULATIONS OF DISPLACEMENT AND DISTORTION OF PROBE VOLUME.....	188
E.1 Source Code Listing of Refraction Program .....	188
E.2 Plots of Probe Volume Displacement.....	190
F. SMOKE GENERATOR .....	192
F.1 Smoke Generator Apparatus.....	192
F.2 Procedure.....	195



## LIST OF TABLES

Table	Page
1.1 SAE J726 Standard Particle Size Distribution of Test Dust.....	8
2.1 Average Fiber Diameter used in Automotive Air Filtration Paper.....	51
2.2 Typical Properties for Automotive Air Filtration Paper.....	52
5.1 Overall Filter Efficiencies Assuming a Monodisperse Particle Size Distribution .....	131
5.2 Standard SAE Polydisperse Test Dust Distributions by Percent Weight .....	134
5.3 Overall Filter Efficiencies for the Fine and Coarse SAE Test Dust Polydisperse Particle Distributions .....	142
A.1 Filter Specifications.....	163

## LIST OF FIGURES

Figure	Page
1.1 SAE (1987b) J726 Efficiency/Capacity Air Filter Element Test Set-up .....	9
1.2 SAE (1987b) J726 Panel Filter Universal Test Housing .....	10
2.1 Filter Media Structure of Packed and Single-Layer Filters: (a) Packed Filter (dust particles not shown) and (b) Single-Layer Filter with Dust Particles Shown in Interstitial Spaces (Crawford, 1976).....	13
2.2 Penetration of Monodisperse Particles Through a Simple Filter, 20 $\mu\text{m}$ Fiber Diameter and 0.05 Packing Fraction, as a Function of Particle Size (Brown, 1993).....	14
2.3 Section of a Filter Illustrating the Scale of Particles and Fibers (Brown, 1993)....	14
2.4 Single Fiber Representation of Particle Capture Illustrated by a Limiting Trajectory (Crawford, 1976).....	17
2.5 Typical Characteristics of $\eta_{coll}$ , $\eta_{adh}$ , and $\eta_s$ (Adapted from Stenhouse, 1975).....	19
2.6 Particle Capture Mechanisms: (A) Capture by Interception, (B) Capture by Inertial Impaction, and (C) Capture by Brownian Diffusion (Brown, 1993) .....	27
2.7 Comparison of Flagan and Sienfeld's (1988) Exact Solution to Sabnis' Combined Interception and Inertial Model (Newman, 1994).....	33
2.8 Comparison of Flagan and Sienfeld's (1988) Exact Solution to Isolated Collision Efficiency Models (Newman, 1994).....	39
2.9 Sphere Attached to a Plane by Capillary Forces (Brown, 1993) .....	43

Figure	Page
2.10 Distribution of Adhesion Energies of Quartz Particles Deposited at a Filtration Velocity of 0.42 m/s on Polyamide Fibers: (1) 15.1 $\mu\text{m}$ Particles; (2) 10.3 $\mu\text{m}$ Particles; (3) 8.3 $\mu\text{m}$ Particles; (4) 5.1 $\mu\text{m}$ Particles (Brown, 1993) .....	44
2.11 Filter Pleat Geometry (Newman, 1994) .....	49
2.12 Envelope Curves for $f(c)$ Verses Packing Fraction, $c$ , with Davies' (1973) Very Low Packing Fraction Empirical Formula Line Curve, Equation (2.52), (Brown, 1993) .....	57
2.13 Efficiency Curves Obtained from Program EFFMODEL at $R_p = 1.25 \mu\text{m}$ , $c = 0.345$ , and $D_{ef} = 51.78 \mu\text{m}$ . .....	62
2.14 Efficiency Curves Obtained from Program EFFMODEL with Parameters Used by Sabnis (1993), $R_p = 1.25 \mu\text{m}$ , $c = 0.230$ , and $D_f = 38.0 \mu\text{m}$ . .....	63
3.1 Experimental Apparatus .....	65
3.2 Schematic of the Laser Doppler Velocimetry System.....	67
3.3 An Example of a Raw Doppler Burst Signal (Hiatt, 1994) .....	73
3.4 Diagram of a Particle Passing through the Fringe Pattern.....	73
3.5 Sign Convention and Coordinate System for Velocity Measurements .....	77
3.6 Velocity Measurement Planes.....	78
3.7 Velocity Measurement Grid.....	79
4.1 Axial Laser Sheet Water Droplet Flow Visualization within the SAE Test Housing (Sabnis, 1993) .....	90

Figure	Page
4.2 Axial Laser Sheet Intermittant Smoke Flow Visualization within the SAE Test Housing with a 76.2 mm Dia Sphere Positioned 159 mm from the Housing Inlet .....	91
4.3 Center Line Axial Velocity Profiles Measured at 13 mm Upstream of the Filter, Plane I, with 50.8 to 76.2 mm Dia Spheres Positioned Near the Inlet.....	94
4.4 Center Line Transverse Velocity Profiles Measured at 13 mm Upstream of the Filter, Plane I, with 50.8 to 76.2 mm Dia Spheres Positioned Near the Inlet.....	95
4.5 Center Line Axial Velocities Measured at 13 mm Upstream of the Filter, Plane I, with 76.2 mm Dia Sphere Positioned at the Specified Distances from the Housing Inlet .....	97
4.6 Center Line Transverse Velocities Measured at 13 mm Upstream of the Filter, Plane I, with 76.2 mm Dia Sphere Positioned at the Specified Distances from the Housing Inlet .....	98
4.7 Non-Dimensional Axial Velocities in the Standard SAE Test Housing Measured at 13 mm Upstream of the Filter, Plane I .....	102
4.8 Non-Dimensional Axial Velocities in the Test Housing Measured at 13 mm Upstream of the Filter, Plane I, with a 76.2 mm Dia Sphere Positioned at 159 mm Downstream from Housing Inlet .....	103
4.9 Non-Dimensional Axial Velocities in the Test Housing Measured at 51 mm Upstream of the Filter, Plane II, with a 76.2 mm Dia Sphere Positioned at 159 mm Downstream from Housing Inlet .....	104
4.10 Non-Dimensional Axial Velocities in the Test Housing Measured at 13 mm Upstream of the Filter, Plane I, with a 76.2 mm Dia Sphere Positioned at 197 mm Downstream from Housing Inlet .....	105
4.11 Non-Dimensional Flow Rate Distribution in the Standard SAE Test Housing Measured at 13 mm Upstream of the Filter .....	108

Figure	Page
4.12 Non-Dimensional Flow Rate Distribution in the Test Housing Measured at 13 mm Upstream of the Filter with a 76.2 mm Dia Sphere Positioned at 159 mm Downstream from Housing Inlet .....	108
4.13 Non-Dimensional Flow Rate Distribution in the Test Housing Measured at 51 mm Upstream of the Filter with a 76.2 mm Dia Sphere Positioned at 159 mm Downstream from Housing Inlet .....	109
4.14 Non-Dimensional Transverse Velocities in the Standard SAE Test Housing Measured at 13 mm Upstream of the Filter, Plane I .....	111
4.15 Non-Dimensional Transverse Velocities in the Test Housing Measured at 13 mm Upstream of the Filter, Plane I, with a 76.2 mm Dia Sphere Positioned at 159 mm Downstream from Housing Inlet .....	111
4.16 Non-Dimensional Transverse Velocities in the Test Housing Measured at 51 mm Upstream of the Filter, Plane II, with a 76.2 mm Dia Sphere Positioned at 159 mm Downstream from Housing Inlet .....	112
4.17 Non-Dimensional Transverse Velocities in the Test Housing Measured at 13 mm Upstream of the Filter, Plane I, with a 76.2 mm Dia Sphere Positioned at 197 mm Downstream from Housing Inlet .....	112
4.18 Axial Turbulence Intensity in Test Housing at 13 mm Upstream of the Filter ....	114
4.19 Axial Turbulence Intensity at 13 mm Upstream of the Filter with a 76.2 mm Dia Sphere Positioned at 159 mm Downstream of the Housing Inlet ..	114
4.20 Axial Turbulence Intensity at 13 mm Upstream of the Filter with a 76.2 mm Dia Sphere Positioned at 197 mm Downstream of the Housing Inlet ..	115
5.1 Single Fiber Efficiency in Standard SAE Test Housing Assuming Perfect Adhesion, 5 $\mu$ m Particles .....	120
5.2 Single Fiber Efficiency in Standard SAE Test Housing, 5 $\mu$ m Particles .....	120

Figure	Page
5.3 Single Fiber Efficiency Assuming Perfect Adhesion with 76.2 mm Dia Sphere Positioned at 159 mm Downstream of the Housing Inlet, 5 $\mu$ m Particles .....	121
5.4 Single Fiber Efficiency with 76.2 mm Dia Sphere Positioned at 159 mm Downstream of the Housing Inlet, 5 $\mu$ m Particles.....	121
5.5 Elemental Efficiency in Standard SAE Test Housing, 1.0 $\mu$ m Particles.....	125
5.6 Elemental Efficiency with 76.2 Dia Sphere Positioned at 159 mm Downstream of the Housing Inlet, 1.0 $\mu$ m Particles .....	125
5.7 Elemental Efficiency in Standard SAE Test Housing, 2.5 $\mu$ m Particles.....	126
5.8 Elemental Efficiency with 76.2 Dia Sphere Positioned at 159 mm Downstream of the Housing Inlet, 2.5 $\mu$ m Particles .....	126
5.9 Elemental Efficiency in Standard SAE Test Housing, 5.0 $\mu$ m Particles.....	127
5.10 Elemental Efficiency with 76.2 Dia Sphere Positioned at 159 mm Downstream of the Housing Inlet, 5.0 $\mu$ m Particles .....	127
5.11 Elemental Efficiency in Standard SAE Test Housing, 7.5 $\mu$ m Particles.....	128
5.12 Elemental Efficiency with 76.2 Dia Sphere Positioned at 159 mm Downstream of the Housing Inlet, 7.5 $\mu$ m Particles .....	128
5.13 Elemental Efficiency of Unity Across Filter Assuming Perfect Adhesion with or without 76.2 Dia Sphere Positioned Either 159 mm or 197 mm Downstream of the Housing Inlet, for Particles $\geq$ 15.0 $\mu$ m .....	129
5.14 Elemental Efficiency in Standard SAE Test Housing, 15.0 $\mu$ m Particles.....	129
5.15 Elemental Efficiency with 76.2 Dia Sphere Positioned at 159 mm Downstream of the Housing Inlet, 15.0 $\mu$ m Particles .....	130

Figure	Page
5.16 Elemental Efficiency with 76.2 Dia Sphere Positioned at 197 mm Downstream of the Housing Inlet, 15.0 $\mu\text{m}$ Particles .....	130
5.17 Cumulative Mass Fraction Distribution of SAE Polydisperse Fine Grade Test Dust .....	133
5.18 Cumulative Mass Fraction Distribution of SAE Polydisperse Coarse Grade Test Dust .....	133
5.19 Overall Elemental Efficiency in Standard SAE Test Housing Assuming Perfect Adhesion, SAE Fine Grade Test Dust Distribution .....	136
5.20 Overall Elemental Efficiency in Standard SAE Test Housing, SAE Fine Grade Test Dust Distribution .....	136
5.21 Overall Elemental Efficiency in Standard SAE Test Housing Assuming Perfect Adhesion, SAE Coarse Grade Test Dust Distribution .....	137
5.22 Overall Elemental Efficiency in Standard SAE Test Housing, SAE Coarse Grade Test Dust Distribution .....	137
5.23 Overall Elemental Efficiency Assuming Perfect Adhesion with 76.2 mm Dia Sphere Positioned at 159 mm Downstream of the Housing Inlet, SAE Fine Grade Test Dust Distribution .....	138
5.24 Overall Elemental Efficiency with 76.2 mm Dia Sphere Positioned at 159 mm Downstream of the Housing Inlet, SAE Fine Grade Test Dust Distribution .....	138
5.25 Overall Elemental Efficiency Assuming Perfect Adhesion with 76.2 mm Dia Sphere Positioned at 159 mm Downstream of the Housing Inlet, SAE Coarse Grade Test Dust Distribution .....	139
5.26 Overall Elemental Efficiency with 76.2 mm Dia Sphere Positioned at 159 mm Downstream of the Housing Inlet, SAE Coarse Grade Test Dust Distribution .....	139

Figure	Page
5.27 Overall Elemental Efficiency Assuming Perfect Adhesion with 76.2 mm Dia Sphere Positioned at 197 mm Downstream of the Housing Inlet, SAE Fine Grade Test Dust Distribution.....	140
5.28 Overall Elemental Efficiency with 76.2 mm Dia Sphere Positioned at 197 mm Downstream of the Housing Inlet, SAE Fine Grade Test Dust Distribution.....	140
5.29 Overall Elemental Efficiency Assuming Perfect Adhesion with 76.2 mm Dia Sphere Positioned at 197 mm Downstream of the Housing Inlet, SAE Coarse Grade Test Dust Distribution.....	141
5.30 Overall Elemental Efficiency with 76.2 mm Dia Sphere Positioned at 197 mm Downstream of the Housing Inlet, SAE Coarse Grade Test Dust Distribution.....	141
6.1 Effect of Non-Uniform Flow through a Porous Foam Filter Tested in Layers: (a) Non-Uniform Flow, and (b) Uniform Flow ((Brown, 1993).....	145
6.2 Diffuser Geometry of a Flat Walled Diffuser (White, 1979).....	149
6.3 Schematic of Flat Walled Diffuser Operating Flow Regimes (Chang, 1970).....	149
6.4 Flat Walled Diffuser Operating Flow Regime Map (White, 1979).....	150
6.5 Shallow Angle Prototype Panel Filter Test Housing.....	153
6.6 Velocity Distribution 13 mm Upstream of Filter in Prototype Test Housing.....	154
E.1 Probe Volume Displacement for Axial (Blue) and Transverse (Green) Beams for a 6.4 mm (0.25 in.) Plexiglas with Varying Housing Angle.....	190
E.2 Probe Volume Displacement for Axial (Blue) and Transverse (Green) Beams for a 9.5 mm (0.375 in.) Plexiglas with Varying Housing Angle.....	191
F.1 Schematic of the Smoke Generator.....	197



## NOMENCLATURE

$a_e$	elemental area ( $m^2$ )
$a_o, b_o, c_o$	experimental parameters of adhesion model
$A$	area as specified ( $m^2$ )
$A_I$	Hamaker constant
$b$	radius of surrounding cell used in single fiber representation
$c$	dimensionless packing fraction or packing density of filter
$C_c$	Cunningham slip correction factor
$C_o$	particle concentration entering filter per unit volume ( $m^{-3}$ )
$C_{eo}$	elemental particle concentration entering filter per unit volume ( $m^{-3}$ )
$d$	distance between interference fringes (m)
$D_f$	fiber diameter (m)
$D_p$	particle diameter (m)
$f$	frequency (Hz)
$f(c)$	dimensionless packing density function
$F$	adhesion force (N)
$h$	filter depth (m)
$I_p$	interception parameter
$Kn$	Knudsen number
$Ku$	Kuwabara hydrodynamic factor

$L$	length of all fibers in a unit volume of filter media (m)
$N$	total number of samples
$p$	pitch of filter (m)
$P$	filter penetration
$P_o$	dimensionless porosity
$P_e$	elemental penetration
$q$	electrostatic charge
$Q$	volumetric flow rate ( $\text{m}^3/\text{s}$ )
$Q_f$	volumetric flow rate through filter ( $\text{m}^3/\text{s}$ )
$r, \theta$	Cylindrical coordinates
$R_a$	radius of the surface asperity
$R_f$	radius of fiber (m)
$R_p$	radius of particle (m)
$Re$	Reynolds number of flow
$Re_f$	Reynolds number based on fiber diameter
$Re_p$	Reynolds number based on particle diameter
$SF$	solidity factor
$St$	Stokes number
$St_c$	Stokes number corrected for slip
$t$	time (s)
$u$	velocity near filter pleats (m/s)

$u_o$	measured axial velocity upstream of the filter media (m/s)
$u_\infty$	velocity inside filter media (m/s)
$V$	fluid velocity (m/s)
$w_1, w_2$	diffuser inlet throat width (m)
$x, y$	Cartesian coordinates
$y_o$	distance between the center line of a fiber and the streamline below which all particles are collected by inertial impaction and interception (m)
$Y$	distance between the center line of a fiber and the streamline below which all particles are collected by interception (m)
$z_o$	distance between particle and fiber (m)
$\gamma$	Euler's constant
$\delta$	charge density depth (m)
$\epsilon_o$	permittivity of free space
$\eta$	efficiency as specified
$\eta_1, \eta_2$	independent collection efficiencies
$\eta_{adh}$	adhesion efficiency
$\eta_{coll}$	collision efficiency
$\eta_e$	elemental efficiency
$\eta_f$	overall filter efficiency
$\eta_I$	inertial impaction efficiency
$\eta_R$	interception efficiency

$\eta_s$	single fiber efficiency
$\lambda$	mean free path of air (m)
$\mu$	dynamic viscosity of air (Pa s)
$\rho$	density of air (kg/m <sup>3</sup> )
$\rho_p$	density of aerosol particle (kg/m <sup>3</sup> )
$\tau$	surface tension (N/m)
$\psi$	stream function

# CHAPTER I

## INTRODUCTION

### 1.1 Background

Automotive engines require a great quantity of air to properly burn the combustion fuel. Since engines are expected to operate under a large variety of conditions and atmospheres, the intake air must be filtered and cleaned. Automotive air cleaners allow intake air to pass freely while removing harmful dust and abrasive particles which may otherwise accelerate engine wear, and thus, limit engine performance and endurance. Most commonly used automotive air filters are round type and panel type filters that are dry and replaceable. Critical operating characteristics of filters include (McQuiston and Parker, 1994): filtration efficiency, air flow resistance, and dust-holding capacity. The filtration efficiency is the measure of the air cleaner's ability to remove particulate matter from an air stream. Smaller particles are typically the most difficult to filter, resulting in lower filtration efficiencies than larger particles. In general, the filtration efficiency of dry-type filters and filters exposed to low dust concentrations increase with dust loading. The air-flow resistance is the loss in total pressure at a specified air flow rate which typically increases with the amount of dust loading. Dust-holding capacity defines the amount of dust that the air cleaner can hold when it is operated at a specified air flow rate to some maximum resistance value.

To date, there are hundreds of different automotive engine air cleaners required to service numerous makes and models of vehicles. Major United States manufacturers of automotive air filters include Purolator Products Inc., AC Rochester, Fram, Motorcraft, and Wix. Due to the fact that filter performance may vary from different air intake systems and constricted housing designs dictated by limited underhood space, it is critical that manufacturers and designers understand the filtration parameters of importance and know how to control them. The Society of Automotive Engineers recognized the need for standardization of air cleaners and compiled a listing of recommended air cleaners (SAE, 1987a) and an air cleaner test code (SAE, 1987b). SAE J1141 Air Cleaner Elements (1987a) provides a listing of recommended round type and panel type filters for United States domestic passenger cars and light trucks. SAE J726 Air Cleaner Test Code (1987b) provides a standardized method of determining and reporting air cleaner performance. However, past and present work has shown that air filters tested in the SAE standardized test code housing experience very non-uniform flow [Sabnis, 1993; Newman, 1994; Liu et al., 1995]. For the past 3 years, in cooperation with Purolator Products Inc., the O.S.U. School of Mechanical and Aerospace Engineering has been working closely with the SAE Air Cleaner Test Code Subcommittee to aid in revising the current test code in efforts to achieve a testing system ensuring a more uniform flow throughout the filter specimens. Such communications have contributed to the development of the recently published SAE J1669 Passenger Compartment Air Filter Test Code (SAE, 1993).

This thesis primarily focuses on the non-uniformity effects and improvement of flow uniformity within the “universal” standardized SAE test housing for panel type filters. Focus is centered on pleated panel type filters, specifically, the Purolator AF3192 air filter for which this project has already developed much investigation. Purolator specifications for the AF3192 panel air filter are provided in Appendix A. Flow visualizations, velocity measurements, and efficiency calculations, all upstream of a pleated panel filter mounted within the SAE standard test housing and within an altered test housing were conducted and are presented within this thesis.

## 1.2 Objectives, Scope, and Limitations of Present Study

Automotive air filter testing is conducted in accordance with the SAE Air Cleaner Test Code J726. Past and present work in this project has shown that filters tested in the SAE test housing experience very non-uniform flow that resembles that of an impinging jet (Sabnis, 1993; Sabnis et al., 1994a and 1994b, Newman, 1994; Liu et al., 1995). Flow visualizations and velocity measurements have shown that the housing provides strongly recirculating separated flow at the walls of the housing and that the flow upstream of the filter is channelled through the central region of the filter. A testing system ensuring uniform flow throughout the filter would be ideal. In efforts to achieve a more uniform flow, attention is centered on the redesigning and/or recommending modifications to the “universal” SAE standard test housing. One alternative is to obstruct the inlet flow in

such a manner as to provide a more uniformly distributed flow pattern. This thesis primarily focuses on the non-uniformity effects of the standard SAE test housing and the improvement of the flow uniformity by obstructing the inlet flow with a sphere. The main objectives were to analyze the flow field within the altered SAE test housing and improve past modeling of filtration efficiency. Specifically, alternative efficiency models and parameters, such as, packing density, non-perfect adhesion, weight averaged fiber diameter, and effective fiber diameter, were investigated and implemented. Flow visualizations, laser Doppler velocimetry measurements, and efficiency calculations with modified parameters were used to achieve these objectives.

Liang et al. (1994) developed a low angle diffuser prototype panel filter test housing specifically designed for the Purolator AF3192 panel air filter. Due to the low angles of the diffuser section, separation along the walls of the housing was virtually eliminated and more uniform flows were achieved. Newman (1994) achieved similar results using the same prototype housing and extended the study to include filtration efficiencies. Throughout this formal report, reference to this prototype housing will be made as a comparison. However, the reader is referred to references (Liang et al, 1994 and Newman, 1994) for a detailed discussion and analysis of the prototype test housing flow field.

Sabnis (1993) developed a FORTRAN program incorporating a model for collection efficiencies and utilized it to analyze the efficiencies of pleated panel filters using measured velocity distributions within the SAE test housing. Newman (1994) developed a



similar C++ program for collection efficiencies and extended it to include an adhesion model. He then utilized the program to analyze the filtration efficiency through both the SAE test housing and the low angle prototype housing. For simplicity, a FORTRAN program, EFFMODEL.FOR, was recently developed to incorporate the same models used by Sabnis and Newman. Related filtration parameters were modified and added as needed to provide a more realistic filtration efficiency model. Neither program developed by Sabnis nor Newman was utilized in the work presented here. For our purposes, these programs and results will not be discussed.

The scope of this thesis has been limited to (1) initially clean pleated panel filters, (2) the non-uniformity effects of the standard SAE test housing, (3) the improvement of the flow uniformity by obstructing the inlet flow of the housing, (4) related filtration theory including perfect and non-perfect adhesion efficiency modeling, and (5) monodisperse and polydisperse test dust distributions as specified by SAE. Past work presented is used merely as a comparison of recent accomplishments. The reader is referred to (Sabnis, 1993; Sabnis et al., 1994a and 1994b; Liang et al., 1994; Newman, 1994) for detailed discussions of past work.

### 1.3 The SAE J726 Air Cleaner Test Code

Due to variations in air intake systems and constricted housing designs dictated by limited underhood space, performance testing under actual operating conditions is difficult

to conduct. However, by use of an ideal standard universal testing system ensuring uniform flow throughout the filter specimen, test conditions could be controlled, and accurate comparison of performance characteristics between different filter designs may be made among different manufacturers and laboratories. With this in mind, the Society of Automotive Engineers developed the SAE J726 Air Cleaner Test Code (SAE, 1987b). The air cleaner test code provides a uniform method of determining and reporting air cleaner performance characteristics on the specified laboratory testing set-up and equipment. The SAE test code includes testing of automotive air cleaners for passenger cars and light trucks, as well as, heavy trucks and industrial applications, and oil bath air cleaners. For our purposes, we are only concerned with the first two sections of the test code dealing with general information and automotive air cleaner test procedures.

The SAE J726 test code allows for uniform testing procedures, conditions, equipment, and standardized performance reports. Critical operating characteristics of the SAE test code include: (1) dust collection efficiency, (2) airflow restriction or pressure drop, (3) dust-holding capacity, and (4) air cleaner element structure. The standardized SAE test dust, typically comprised of 67-69% of SiO<sub>2</sub> by weight, is specified in two grades, fine and coarse. Note that a typical chemical analysis of test dust was obtained from AC Division, General Motors Corp. and is provided in the SAE test code. The particle size distribution is specified and described by percent volume and percent weight as listed in Table 1.1. Illustrations and descriptions of recommended test equipment to determine resistance to air flow, dust-holding capacity, dust removal characteristics,

sealing characteristics, and rupture/collapse characteristics are provide within the test code. A schematic of the efficiency/capacity air filter element test set-up is illustrated in Figure 1.1. The testing set-up consists of a dust metering and feeding system, a pressure drop measuring device, the specified filter housing, an absolute filter housing downstream of the filter specimen, a flowrate measuring system, and the required blower for induced air flow. A detailed drawing of the panel filter universal test housing is illustrated in Figure 1.2. Test procedures are specified for the (1) efficiency test, (2) air flow restriction and pressure drop test, (3) dust-holding capacity test, and (4) the three air filter element structure tests: flow pressure collapse test, seal effectiveness test, and temperature extreme test.

Table 1.1

## SAE J726 Standard Particle Size Distribution of Test Dust

Particle Size distribution by Volume		
Size [ $\mu\text{m}$ ]	Fine Grade Volume (% less than)	Coarse Grade Volume (% less than)
5.5	38 $\pm$ 3	13 $\pm$ 3
11	54 $\pm$ 3	24 $\pm$ 3
22	71 $\pm$ 3	37 $\pm$ 3
44	89 $\pm$ 3	56 $\pm$ 3
88	97 $\pm$ 3	84 $\pm$ 3
125	100	100
Particle Size Distribution by Weight		
Size Range [ $\mu\text{m}$ ]	Fine Grade % Weight	Coarse Grade % Weight
0-5	39 $\pm$ 2	12 $\pm$ 2
5-10	18 $\pm$ 3	12 $\pm$ 3
10-20	16 $\pm$ 3	14 $\pm$ 3
20-40	18 $\pm$ 3	23 $\pm$ 3
40-80	9 $\pm$ 3	30 $\pm$ 3
80-200	-	9 $\pm$ 3

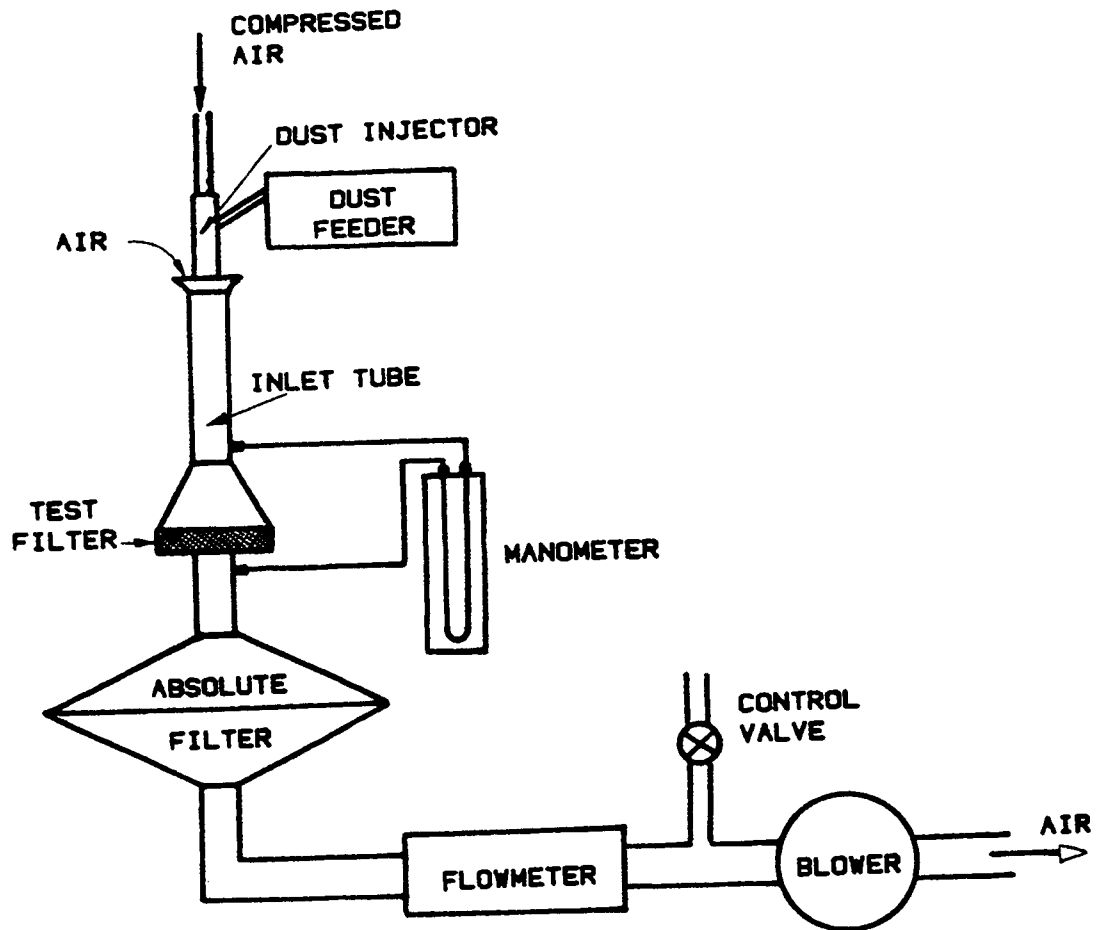


Figure 1.1 SAE (1987b) J726 Efficiency/Capacity Air Filter Element Test Set-up

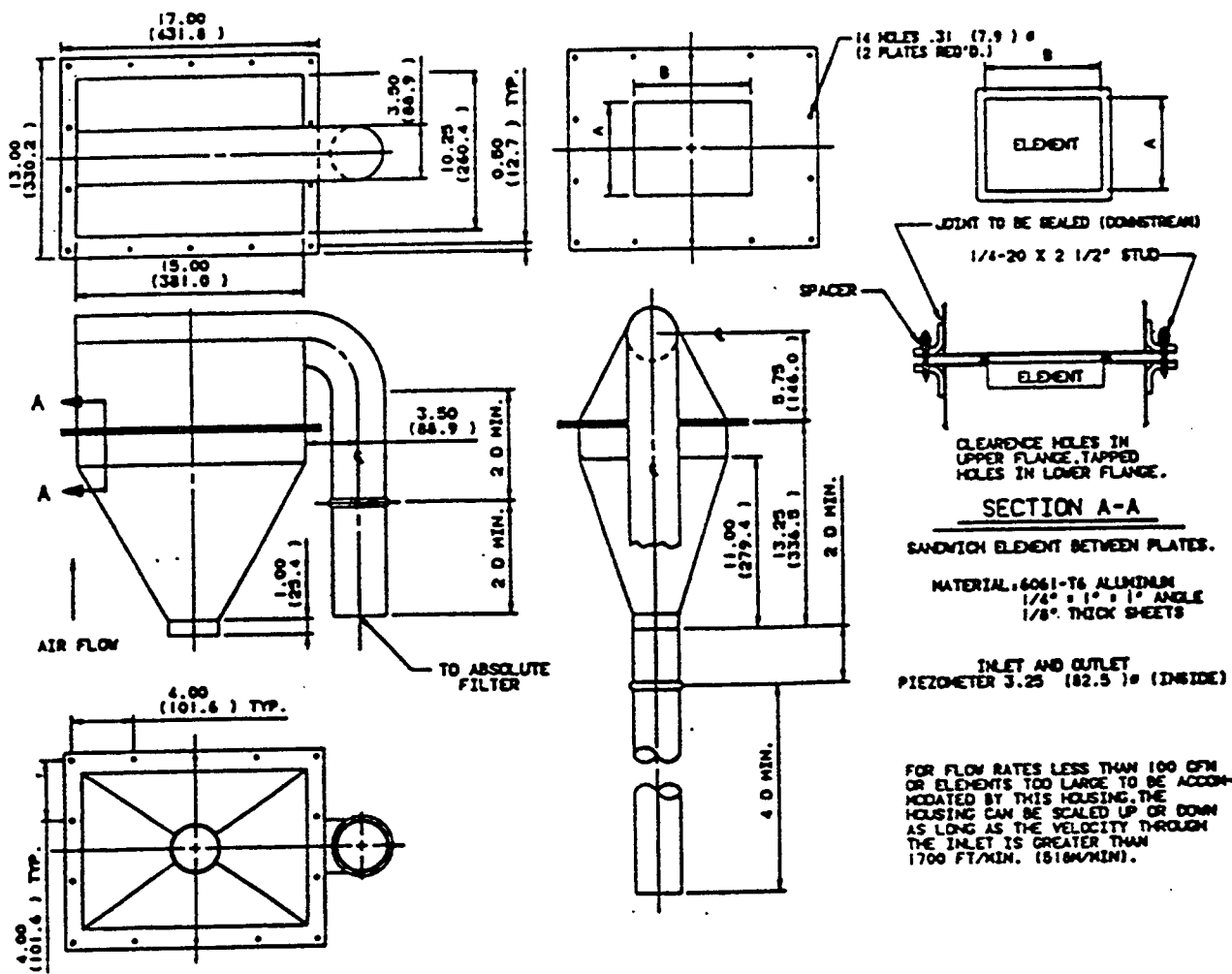


Figure 1.2 SAE (1987b) J726 Panel Filter Universal Test Housing

## CHAPTER II

### FIBROUS FILTRATION THEORY AND METHODOLOGY

#### 2.1 Fibrous Filtration

Fibrous filtration is a well known and accepted method for separating dry particles from a gas stream, usually of air or combustion gases. In fibrous filtration, the dusty gas flows into and through the filter, leaving the dust retained by the fabric. The fabric itself does some filtering of the particles; however, it serves more as a support medium for the layer of dust that quickly accumulates on it (Cooper and Alley, 1994). Filters can be classified as one of two types, packed filter and single-layer filter type, based on the way in which fibers are held in place (Crawford, 1976). Due to their open structure, both types offer a low resistance to airflow. In the packed filter type, the fibers are loosely and randomly packed into a substantial volume. In the single-layer filter, fibers are woven into a thin layer of cloth or paper. Packed filters and single-layer filters are commonly referred to as non-woven and woven fibrous filters, respectively. Refer to Figure 2.1 for an illustration of filter elements in packed and single-layer filters. Non-woven filters are typically used within the automotive and air conditioning industry, whereas, woven filters are commonly used in large industrial applications.

A useful way to think of a filter is as a large number of woven or non-woven layers, each sparsely populated with fibers (Brown, 1993). Even if an individual fiber layer has a very low capture efficiency, the filter as a whole will perform well due to the depth-filtration. Depth-filtration refers to the increase in filtration performance due to the increase in filter depth. Figure 2.2 shows that particles with diameters less than 10  $\mu\text{m}$  are efficiently captured by a filter with fibers of approximately 20  $\mu\text{m}$  in diameter and a packing density of 0.05. Packing density or packing fraction is defined as the volume fraction of the filter fibers. Even though the interfiber spaces of the filter were up to 100  $\mu\text{m}$  in size, the less than 10  $\mu\text{m}$  diameter particles were able to be captured due to the depth filtration. Points of fiber-fiber contact are relatively infrequent (Brown, 1993). Thus, it is very unlikely that the particles were captured by more than one fiber as illustrated in Figure 2.3. Consequently, the theory of particle capture is often discussed and analyzed in terms of a single fiber. Single Fiber Representation is discussed in the following section. Sabnis (1993) and Newman (1994) conducted an extensive review of relevant literature available on filtration theory through fibrous filters. Here, primary focus is given to filtration efficiency models. A number of simple and rigorous filtration efficiency models have been developed by different investigators over the past forty years (Landahl and Herrmann, 1949; Freshwater and Stenhouse, 1972; Suneja and Lee, 1974; First and Hinds, 1976; Lee and Liu, 1982a and 1982b; Flagan and Seinfeld, 1988; Ptak and Jaroszczyk, 1990; Wang and Kasper, 1991; Brown, 1993). The following sections of this chapter serve as a brief review of modern concepts of filtration which are referred to



throughout this thesis. The reader is referred to Davies, 1973; Crawford, 1976; Flagan and Seinfeld, 1988; and Brown, 1993 for detailed discussion of filtration theory and practice.

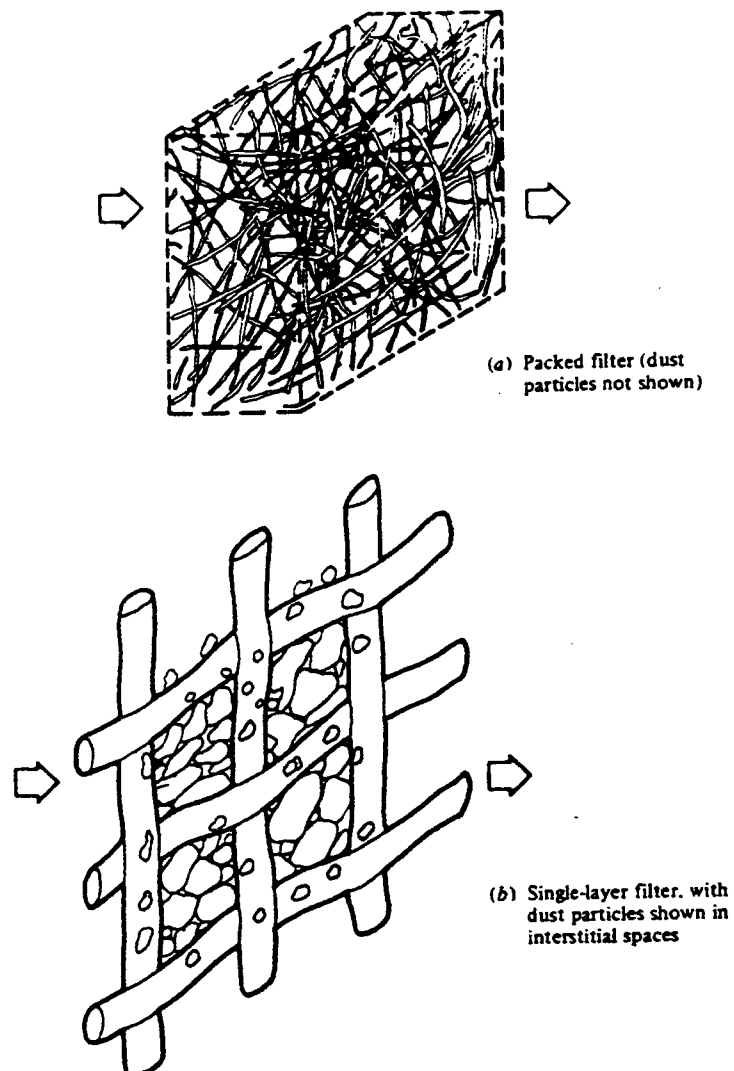


Figure 2.1 Filter Media Structure of Packed and Single-Layer Filters:

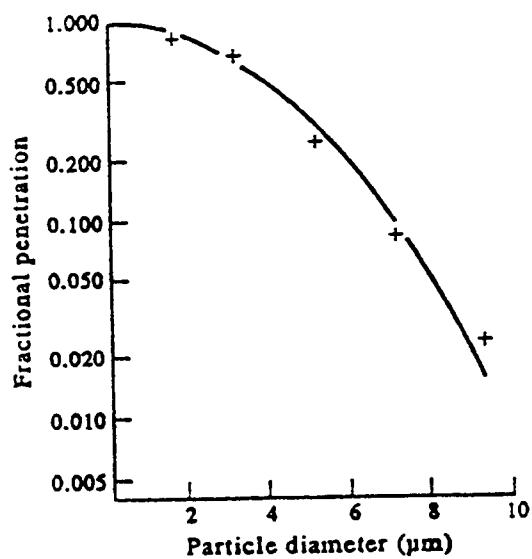


Figure 2.2 Penetration of Monodisperse Particles Through a Simple Filter, 20  $\mu\text{m}$  Fiber Diameter and 0.05 Packing Fraction, as a Function of Particle Size (Brown, 1993)

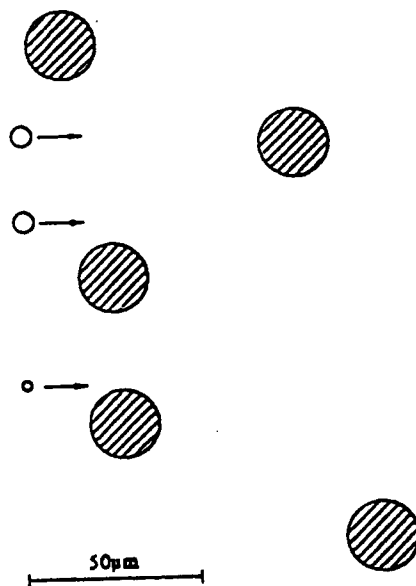


Figure 2.3 Section of a Filter Illustrating the Scale of Particles and Fibers (Brown, 1993)

## 2.2 Fiber Representation and Filtration Efficiencies

### 2.2.1 Single Fiber Representation of a Fibrous Filter

The behavior of a particle captured by a filter is often discussed and analyzed in terms of a single fiber within the depth of a filter and then related to the overall behavior of the filter. As discussed by Davies (1973), the dimensionless porosity,  $P_o$ , and the dimensionless packing density,  $c$ , solidity or volume fraction of the fibers, may be related as:

$$c = \pi R_f^2 L = 1 - P_o \quad (2.1)$$

assuming the media consists of fibers with uniform radius,  $R_f$ .  $L$  represents the length of all fibers in a unit volume of the media. The collision or collection efficiency of aerosol particles with a fiber,  $\eta_{coll}$ , depends on both particle and fiber parameters. Single fiber representation considers the effects of the surrounding fibers and packing density of the media by considering a cell surrounding the fiber. The radius of this surrounding cell,  $b$ , is related to the packing density and to the size of the fibers (Crawford, 1976).

$$b = \sqrt{\frac{1}{\pi L}} = \frac{R_f}{\sqrt{c}} \quad (2.2)$$

Figure 2.4 shows a fiber held normal to the flow of air at a distance  $b$  upstream from the center of the fiber cylinder. Note that  $D_f$  is the diameter of the fiber,  $2R_f$ , and  $D_p$  is the diameter of the particle,  $2R_p$ .

Fiber collection of particles may also be analyzed by isolated fiber representation. Isolated fiber representation differs from single fiber representation by not considering surrounding fiber effects and the effects of packing density. According to Davies (1973), this theory is accurate only for mechanisms of particle collection which operate very near to the fiber surface; such as, Brownian diffusion and electrostatic attraction. Mechanisms of particle collection are discussed in Section 2.3.

### 2.2.2 Flow Around a Fiber

In examining the flow field around the fiber cylinder, the velocity inside the filter,  $u_\infty$ , is greater than the velocity upstream of the filter media,  $u$ , due to the partial blocking of flow by the fibers (Crawford, 1976):

$$u_\infty = \frac{u}{(1-c)} \quad (2.3)$$

The Reynolds number of the flow through the filter,  $Re_f$ , is defined with respect to the velocity inside the filter media,  $u_\infty$ , and the fiber diameter,  $D_f$ :

$$Re_f = \frac{D_f u_\infty \rho}{\mu} \quad (2.4)$$

where  $\rho$  is the density of air, and  $\mu$  is the dynamic viscosity of air. Typical Reynolds numbers are in the order of one or smaller, for fibrous filters.

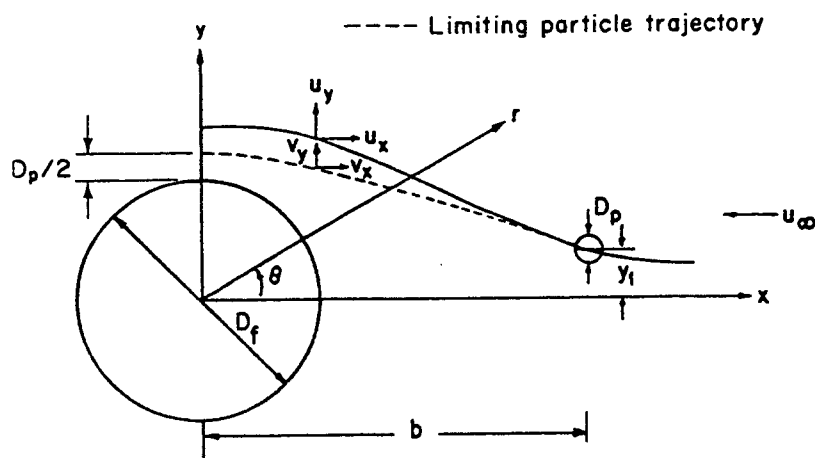


Figure 2.4 Single Fiber Representation of Particle Capture Illustrated by a Limiting Trajectory (Crawford, 1976)

### 2.2.3 Single Fiber Efficiency

Davies (1973) proposed that flow through a filter is nearly always laminar. Using simple geometry, Davies derived and then suggested that the single fiber efficiency is equal to the ratio of the distance between two limiting streamlines of the flow approaching a fiber,  $2y$ , to the diameter of the fiber,  $2R_f$ . Refer to Figure 2.4, Single Fiber Representation of Particle Capture Illustrated by a Limiting Trajectory. Davies assumes that all particles striking the fiber remain adhered to it, or perfect adhesion occurs. Perfect adhesion has generally been assumed in the vast amount of work reviewed. However, due to particle removal mechanisms such as aerodynamic drag; "blow-off", or simple rebound after impact; "bounce-off", it is certainly not always the case that once a particle touches a fiber it will permanently adhere to its surface (Freshwater and Stenhouse, 1972). Ptak and

Jaroszcyk (1990) recognized the importance of distinguishing the difference between collection efficiency and collision efficiency. The difference is associated with momentum of solid dust particles and their adhesion to the fiber surface. Collection efficiency refers to the degree of particles collected, adhered, and retained by the fibers, whereas, collision efficiency refers to the degree of particles merely making contact with a fiber. Thus, the single fiber collection efficiency is best expressed as:

$$\eta_s = \eta_{coll}\eta_{adh} \quad (2.5)$$

where  $\eta_s$  is the single fiber collection efficiency,  $\eta_{coll}$  is the collision, and  $\eta_{adh}$  is the retention or adhesion efficiency. Typical characteristics of  $\eta_{coll}$ ,  $\eta_{adh}$ , and  $\eta_s$  as presented by Stenhouse (1975) are shown in Figure 2.5.

Much work has been devoted to collision efficiency of small particles. Refer to the following sections. Some important parameters which determine particle adhesion and retention efficiency have been investigated experimentally (Krupp, 1967; Dahneke, 1971, 1973, and 1974; Freshwater and Stenhouse, 1972; Walkenhorst, 1972; First and Hinds, 1976; Ptak and Jaroszcyk, 1990). However, there is a very limited presentation of quantitative methods by which values of  $\eta_{adh}$  may be correlated or predicted (Ptak and Jaroszcyk, 1990; Wang and Kasper, 1991). For a more detailed discussion, refer to Section 2.6 Adhesion and Retention of Captured Particles.

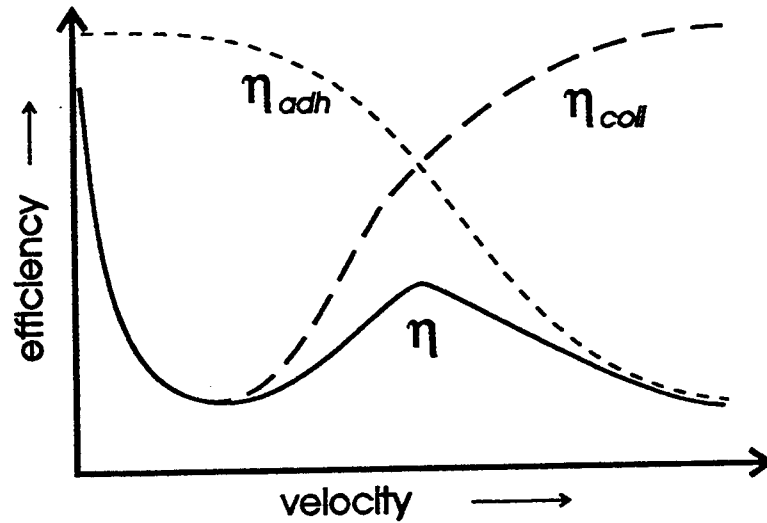


Figure 2.5 Typical Characteristics of  $\eta_{coll}$ ,  $\eta_{adh}$ , and  $\eta_s$   
(Adapted from Stenhouse, 1975)

#### 2.2.4 Isolated Fiber Efficiency

Recall from Sub-Section 2.2.1 that isolated fiber representation differs from single fiber representation by not considering surrounding fiber effects and the effects of packing density. To account for the effects of neighboring fibers on the efficiency of any given fiber, Ptak and Jaroszczyk (1990) experimentally determined a “solidity factor,” expressed as:

$$SF = \frac{0.9}{c^{0.3}} \quad (2.6)$$

The product of an isolated fiber efficiency,  $\eta_i$ , and the solidity factor is the single fiber collection efficiency,  $\eta_s$ :

$$\eta_s = SF\eta_i \quad (2.7)$$

Note that the authors do not specify any limitations or conditions for Equation (2.6). It is suggested here that possible limitations be investigated in future work.

### 2.2.5 *Elemental Fiber Efficiency*

As described by Crawford and other authors, a simple mass balance across a filter bed and integration through the filter bed thickness, from 0 to  $h$ , yields that the particle concentration entering a filter bed,  $C_o$ , and the particle concentration leaving a filter bed,  $C$ , are related by (Crawford, 1976):

$$\frac{C}{C_o} = \exp\left(-\frac{2c\eta_s h}{\pi(1-c)R_f}\right) \quad (2.6)$$

Where  $\eta_s$  is the single fiber efficiency and  $h$  is the filter thickness. This assumes the filter has uniform packing density  $c$  and fiber radius  $R_f$ , and that the filter efficiency is also uniform through the filter. Recall that for any filtering process, the ratio of particles leaving the system to particles entering the system defines the amount of particles penetrating through the filtering system. With this in mind, the above concentration ratio defines the penetration of the filter bed:

$$P = \frac{C}{C_o} \quad (2.9)$$



Furthermore, the efficiency of any filtering process is the ratio of particles collected to the particles entering the filtering process. Alternatively, the filtering efficiency may be expressed in terms of the fraction of particles penetrating the filter, the penetration:

$$\eta = 1 - P \quad (2.10)$$

Thus, combining the preceding three equations gives the following expression for the elemental fiber efficiency:

$$\eta_e = 1 - P_e = 1 - \exp\left(-\frac{2c\eta_s h}{\pi(1-c)R_f}\right) \quad (2.11)$$

The elemental fiber efficiency represents the overall efficiency of a small element of a filter having thickness  $h$ . Note that depending on how the single fiber efficiency is defined, the elemental fiber efficiency may or may not include the various mechanisms of particle collection or particle retention as discussed in later sections.

#### 2.2.6 Overall Filter Efficiency

Once the individual elemental efficiencies of a filter are all determined, an overall filter efficiency,  $\eta_f$ , may be calculated as a weighted average of the elemental efficiencies.

It is common to express this weighted average in terms of the elemental penetration.

From Equation (2.10) or (2.11), the elemental penetration,  $P_e$ , is given by  $P_e = 1 - \eta_e$ .

Let the elemental particle number density or the elemental dust concentration entering the filter element be  $C_{e0}$ , per unit volume. The particle number density at the exit of the filter element may then be expressed as  $C_{e0}P_e$ . If  $Q_f$  is the air volumetric flow rate through the

filter and  $C_o$  is the total particle number density entering the filter, the number rate of particles entering the flow is simply the product of these two terms. For  $n$  elements of elemental surface area,  $a_e$ , and elemental velocity inside the pleats,  $u_\infty$ , the total number rate of particles entering the filter flow is  $C_o \sum_{i=1}^n a_e u_\infty$ . For  $n$  elements, the overall efficiency of the filter,  $\eta_f$ , is expressed as one minus the ratio of the total number rate of particles penetrating each element to the number rate of particles entering the filter flow:

$$\eta_f = 1 - \frac{\sum_{i=1}^n [(C_{eo} P_e) a_e u_\infty]_i}{C_o \sum_{i=1}^n [a_e u_\infty]_i} \quad (2.12)$$

If we assume a uniform particle concentration per unit volume,  $C_o = (C_{eo})_i$  for any  $i$ , then Equation (2.12) may be rewritten as:

$$\eta_f = 1 - \frac{\sum_{i=1}^n [P_e a_e u_\infty]_i}{\sum_{i=1}^n [a_e u_\infty]_i} \quad (2.13)$$

The elemental surface area  $a_e$  and velocity  $u_\infty$  are defined specifically for a pleated air filter element in Section 2.7 Air Velocities of Pleated Air Filters.

## 2.3 Mechanisms of Particle Capture and Combined Efficiencies

### 2.3.1 Overview

The basis of predicting the collision efficiency,  $\eta_{coll}$ , of a filter bed has been well documented and investigated by several authors. The filter element is taken as a single fiber cylinder normal to the gas flow, as illustrated in Figure 2.4. As described by Flagan and Seinfeld (1988), there are four distinct mechanisms identified whereby particles in the gas can reach the surface of the fiber cylinder: interception, inertial impaction, Brownian diffusion, and electrostatic attraction. An illustration of the first three mechanisms is provided in Figure 2.6. Particle adhesion or retention is not discussed in this section, refer to Section 2.6 Adhesion and Retention of Captured Particles.

### 2.3.2 Interception

Particle capture due to direct interception occurs when a particle, following the streamlines of the flow around a fiber cylinder, is of a finite size sufficiently large that it touches the surface of the fiber cylinder. In other words, interception is said to occur if the streamline on which the particle center lies is within a distance  $D_p/2$  of the fiber cylinder. This mechanism is most important only for particle sizes of  $D_p > 1 \mu\text{m}$  (Flagan and Seinfeld, 1988). Note that the mechanism of interception assumes the particle has size but no mass. Without mass, there will not be any inertia effects and the particle is understood to follow the streamline. Refer to particle A of Figure 2.6.

### *2.3.3 Inertial Impaction*

Particle capture due to inertial impaction occurs when a particle is unable to follow the rapidly curving streamlines because of its inertia. Inertia effects lead the particle along a path of less curvature onto the fiber cylinder. Collision occurs due to momentum. This mechanism is most important only for particle sizes of  $D_p > 1 \mu\text{m}$  (Flagan and Seinfeld, 1988). Note that the mechanism of inertial impaction is based on the premise that the particle has mass but no size. Refer to particle B of Figure 2.6.

### *2.3.4 Brownian Diffusion*

Particle capture due to Brownian diffusion occurs when a particle's random motion of Brownian diffusion brings it into contact with the fiber cylinder. Brownian diffusion is caused by collisions of submicron particles with surrounding molecules. A concentration gradient is established once a few particles are collected. The concentration gradient acts as a driving force to increase the rate of deposition. These effects increase with decreasing particle size. This mechanism is most important for very small particle sizes,  $D_p < 0.5 \mu\text{m}$ , transported in a very low velocity flow fields (Flagan and Seinfeld, 1988). For automotive air filtering of particles greater than  $0.5 \mu\text{m}$ , Brownian diffusion is understood to be negligible. Refer to particle C of Figure 2.6.

### *2.3.5 Electrostatic Attraction*

Particle collection due to electrostatic attraction is driven by a static charge. The

electrostatic forces may be either direct or induced. Direct electrostatic attraction refers to both charged fibers and particles. Induced electrostatic attraction refers to either charged fibers or charged particles. The charging is usually not present unless introduced during the manufacture of the fiber. This mechanism is most important only for particle sizes from 0.01 to 0.5  $\mu\text{m}$  (Flagan and Seinfeld, 1988; Gillespie, 1955). Electrostatic attraction, is not predominantly employed in engine air filters by automotive air filter manufacturers. However, it is being considered in designs of passenger compartment cabin air filters (SAE, 1993). Consequently, primary focus is given to the first three mechanisms of filtration.

### 2.3.6 Combined Particle Collision Efficiencies

The overall particle collision efficiency,  $\eta_{coll}$ , for a fiber cylinder is commonly obtained by analyzing the mechanisms of particle collision separately and then combining the individual efficiencies (Flagan and Seinfeld, 1988). In considering two independent mechanisms of particle capture, the probability that a particle will escape capture by mechanism 1 is:  $(1 - \eta_1)$ . Likewise, the probability that a particle will escape capture by mechanism 2 is:  $(1 - \eta_2)$ . The probability that a particle will escape capture altogether is then the product of two probabilities:  $(1 - \eta_1)(1 - \eta_2)$ . Thus, the probability that a particle will be captured by mechanism 1 and 2 is:

$$\eta_{coll} = 1 - (1 - \eta_1)(1 - \eta_2) \quad (2.14)$$

or for  $n$  independent particle capture mechanisms:

$$\eta_{coll} = (1 - \eta_1)(1 - \eta_2) \cdots (1 - \eta_n) \quad (2.15)$$

Equation (2.14) may be expressed as  $\eta_{coll} = \eta_1 + \eta_2 - \eta_1\eta_2$ . Frequently one mechanism may dominate in a particular range of particle sizes and the third term,  $\eta_1\eta_2$ , will approach some small value compared to the other terms. Consequently, on occasion some authors will express the collection efficiency by two mechanisms as simply:  $\eta_{coll} = \eta_1 + \eta_2$ . Throughout this thesis, the overall particle collision efficiency,  $\eta_{coll}$ , for a fiber cylinder will be defined as in Equation (2.14) or (2.15), unless otherwise stated.

This combined efficiency assumes that the mechanisms are all independent. In other words, it assumes that collection by mechanism 1 occurred independently in series with collection by mechanism 2 and so on. In reality, a particle may be collected due to simultaneous effects of two mechanisms. For example, a particle of small size and mass may not be collected due to interception or inertial impaction alone. However, with combined effects a particle could be collected by inertial interception. Although, this method of combining collection mechanism effects is not thoroughly rigorous, it is an approximate approach and has been demonstrated to agree well with other efficiency models developed from empirical data (Sabnis, 1993; Newman, 1994).

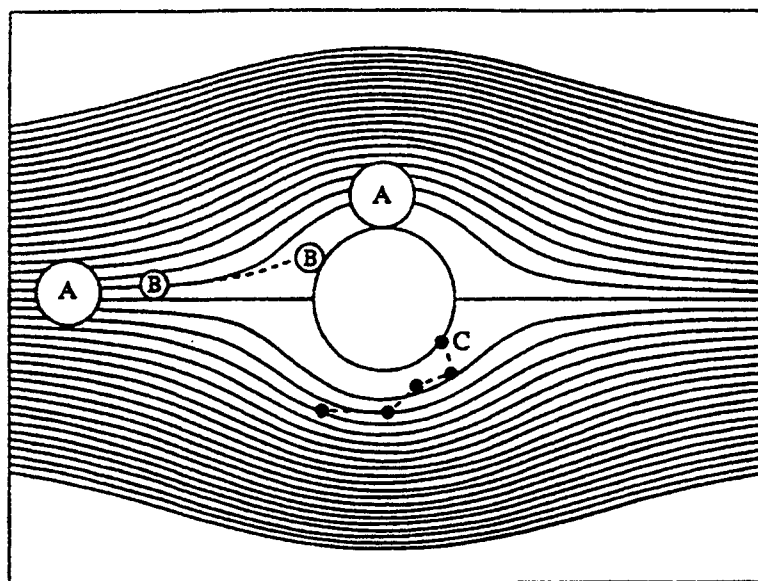


Figure 2.6 Particle Capture Mechanisms: (A) Capture by Interception, (B) Capture by Inertial Impaction, and (C) Capture by Brownian Diffusion (Brown, 1993)

#### 2.4 Kuwabara Flow Field Around a Fiber Cylinder

Particle capture theory requires a description of the flow field close to a fiber in a filter element. The most popular models used today are the models published by Happel (1959) and Kuwabara (1959) used to describe the flow pattern of a fluid through an array of parallel cylinders. Since 1959, alternative flow fields have been published (Brinkman, 1967; and Spielman and Goren, 1968). Davies (1973) has concluded that the Kuwabara flow solution gives the closest agreement to experimental results and makes the most sense to use. Referring back to single fiber representation, a fiber of radius  $R_f$  is assumed to be surrounded by an imaginary cell of radius  $b$ . Navier-Stokes equations for flow

transverse to the cylinders were used with the boundary condition of zero velocity at the surface of the fibers and zero vorticity on the surface of the b cell cylinder. The Kuwabara flow solution, as expressed by Flagan and Seinfeld (1988) in terms of the stream function  $\psi$  is:

$$\psi = \frac{u_{\infty} r}{2Ku} \left[ 2 \ln \frac{2r}{D_f} - 1 + c + \frac{D_f^2}{4r^2} \left( 1 - \frac{c}{2} \right) - \frac{2cr^2}{D_f^2} \right] \sin \theta \quad (2.16)$$

where  $r$  and  $\theta$  are the cylindrical coordinates. The  $Ku$  term is the Kuwabara hydrodynamic factor given as:

$$Ku = c - \frac{3}{4} - \frac{c^2}{4} - \frac{1}{2} \ln c \quad (2.17)$$

The radial and tangential velocity components are given in terms of the stream function which yield the following expressions:

$$u_r = \frac{1}{r} \frac{\partial \psi}{\partial \theta} = \frac{u_{\infty}}{2Ku} \left[ 2 \ln \frac{2r}{D_f} - 1 + c + \frac{D_f^2}{4r^2} \left( 1 - \frac{c}{2} \right) - \frac{2cr^2}{D_f^2} \right] \cos \theta \quad (2.18a)$$

$$u_{\theta} = -\frac{\partial \psi}{\partial r} = \frac{u_{\infty}}{2Ku} \left[ 2 \ln \frac{2r}{D_f} + 1 + c - \frac{D_f^2}{4r^2} \left( 1 - \frac{c}{2} \right) - \frac{2cr^2}{D_f^2} \right] \sin \theta \quad (2.18b)$$

Note that these equations are independent of viscosity and Reynolds number. Several filtration efficiency models are based on this flow field model as discussed in the following section.



## 2.5 Filtration Efficiency Models

### 2.5.1 Lee and Liu Interception Model

Particle capture due to direct interception occurs when a particle, following the streamlines of the flow around a fiber cylinder, is of a finite size sufficiently large that it touches the surface of the fiber cylinder. The single fiber collection efficiency due to interception,  $\eta_R$ , as defined by Lee and Liu (1982a) is:

$$\eta_R = \frac{Y}{R_f} \quad (2.19)$$

where  $Y$  is the distance between the center line and the streamline below which all particles are collected. In terms of the dimensionless stream function passing through a point at a distance of  $R_p$  from the fiber surface, Equation (2.19) becomes:

$$\eta_R = \frac{\psi}{u_\infty R_f} \quad (2.20)$$

Substituting the stream function expression (2.16), as defined by the Kuwabara flow model, Lee and Liu obtained:

$$\eta_R = \frac{1+I_p}{2Ku} \left[ 2 \ln(1+I_p) - 1 + c + \left( \frac{1}{1+I_p} \right)^2 \left( 1 - \frac{c}{2} \right) - \frac{c}{2} (1+I_p)^2 \right] \quad (2.21)$$

where  $Ku$  is the Kuwabara hydrodynamic factor as expressed in Equation (2.17).  $I_p$  is the interception parameter defined as the diameter ratio of particle to fiber, or dimensionless particle radius:

$$I_p = \frac{D_p}{D_f} = \frac{2R_p}{2R_f} \quad (2.22)$$

Equation (2.21) is a complete expression for the interception efficiency based on the Kuwabara flow field model. Lee and Liu found it useful to reduce Equation (2.21) to a simpler form using an approximate form of the stream function. As given by Lee and Liu (1982b), the semi-empirical approximation of Equation (2.21) is:

$$\eta_R = \frac{1-c}{Ku} \frac{I_p^2}{1+I_p} \quad (2.23)$$

This approximation was compared to others obtained by other investigators. In general, for both small  $c$  and small  $I_p$  values, all approximations gave efficiency values that are close to the value computed using Equation (2.21). However, when  $c$  becomes large, Equation (2.23) gives much closer values to Equation (2.21) than any other approximation equation studied (Lee and Liu, 1982b). Lee and Liu (1982b) concluded that the error for the approximations used to obtain the simplified stream function approaches zero as  $c$  increases and approaches 1/3.

### 2.5.2 Landahl and Herrmann Inertial Impaction Model

Particle capture due to inertial impaction occurs when a particle is unable to follow the rapidly curving streamlines because of its inertia. The efficiency of inertial impaction significantly increases with increasing filtration velocity and is a strong function of the Stokes number for particles in the size range of approximately 1 to 80  $\mu\text{m}$  (Jaroszczyk and

Wake, 1991; Landahl and Herrmann, 1949). The Stokes number as expressed by Brown (1993) is:

$$St = \frac{R_p^2 \rho_p u_\infty}{9 \mu R_f} \quad (2.24)$$

For small particles, the Stokes number may be corrected for slip using the Cunningham correction factor approximated as:

$$C_c = 1 + 1.257 Kn \quad (2.25)$$

where  $Kn$  is the Knudsen number expressed as:

$$Kn = \frac{\lambda}{R_p} \quad \text{for } R_p \gg \lambda \quad (2.26)$$

and  $\lambda$  is the mean free path of air. Thus, the Stokes number corrected for slip,  $St_c$ , is defined as:

$$St_c = C_c St = \frac{C_c R_p^2 \rho_p u_\infty}{9 \mu R_f} \quad (2.27)$$

The Landahl and Herrmann (1949) model for isolated fiber efficiency due to inertial impaction, as given by Jaroszczyk and Wake (1991) in terms of the corrected Stokes number, is as follows:

$$\eta_I = \frac{St_c^3}{St^3 + 0.77 St_c^2 + 0.22} \quad (2.28)$$

Recall that the isolated fiber representation differs from the single fiber representation by not considering surrounding fiber effects and the effects of packing density. Using the Ptak and Jaroszczyk (1990) "solidity factor" as in Equation (2.6):

$$SF = \frac{0.9}{c^{0.3}}$$

the Landahl and Herrmann (1949) model may be used to obtain the single fiber efficiency due to inertial impaction:

$$\eta_I = \frac{SF \cdot St_c^3}{St_c^3 + 0.77St_c^2 + 0.22} \quad (2.29)$$

### 2.5.3 Combined Interception and Inertial Impaction Model

If we consider the collision efficiency due to interception and the collision efficiency due to inertial impaction, we can determine the combined total collision efficiency by using Equation (2.14):

$$\eta_{coll} = 1 - (1 - \eta_1)(1 - \eta_2)$$

By substituting the Lee and Liu interception model, Equation (2.23), and the Landahl and Herrmann inertial impaction model, Equation (2.28), into Equation (2.14), one can obtain the following model for combined effects of interception and inertial impaction:

$$\eta_{IR} = 1 - \left( 1 - \frac{1-c}{Ku} \frac{I_p^2}{1+I_p} \right) \left( 1 - \frac{St_c^3}{St_c^3 + 0.77St_c^2 + 0.22} \right) \quad (2.30)$$

Recall that Equation (2.14) assumes that the occurrences of interception and inertial impaction are two independent occurrences. Nonetheless, this model is an approximate approach and has been demonstrated to agree well with other efficiency models developed from empirical data (Sabnis, 1993; Newman, 1994). This model is plotted in Figure 2.7 for a range of Stokes numbers. An exact solution and an approximate solution presented

by Flagan and Seinfeld (1988) as discussed in the following sub-section are also plotted. Note how much better this model compares to the exact solution as compared to the approximate solution. Refer to the next sub-section for a detailed description of the Flagan and Seinfeld (1988) solutions.

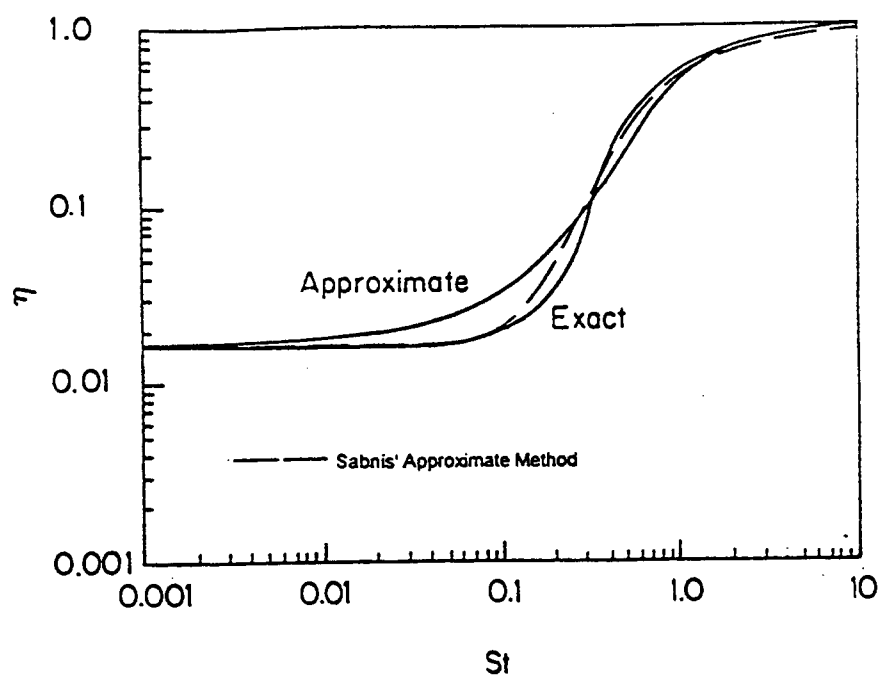


Figure 2.7 Comparison of Flagan and Seinfeld's (1988) Exact Solution to Sabnis' Combined Interception and Inertial Impaction Model (Newman, 1994)

Equation (2.30) is presented just as it was used by Sabnis (1993). The Lee and Liu interception model used is based on the single fiber representation. However, as mentioned earlier, the Landahl and Herrmann inertial impaction model is based on the isolated fiber representation. Thus, to account for neighboring effects within the Landahl and Herrmann inertial impaction model, it is proposed here to incorporate Equation (2.29) with the solidity factor rather than Equation (2.28):

$$\eta_{IR} = 1 - \left( 1 - \frac{1-c}{Ku} \frac{I_p^2}{1+I_p} \right) \left( 1 - \frac{SF \cdot St_c^3}{St_c^3 + 0.77St_c^2 + 0.22} \right) \quad (2.31)$$

One can expect slightly higher efficiencies with Equation (2.30). In general, differences between Equations (2.30) and (2.31) should be minor except in the case of high velocities where inertial impaction dominates.

#### 2.5.4 Interception and Inertial Impaction Modeling by Particle Trajectory

As presented by Flagan and Seinfeld (1988), the trajectory of a particle can be mathematically tracked by inserting the Kuwabara flow field velocities into the equation of motion of a particle. Flagan and Seinfeld present both an approximate solution, using average velocities, and an exact solution, using Kuwabara velocities, to obtain the isolated collision efficiency due to interception and inertial impaction.

The "approximation solution" requires simultaneously solving the following two equations:

$$\eta_{IR} = \frac{2y_1}{D_f} = \frac{1}{2Ku} \left( 1 + \frac{2y_2}{D_f} \right) \left[ \begin{aligned} & 2 \ln \left( 1 + \frac{2y_2}{D_f} \right) - 1 + c \\ & + \frac{1 - c/2}{\left( 1 + \frac{2y_2}{D_f} \right)^2} - \frac{c}{2} \left( 1 + \frac{2y_2}{D_f} \right)^2 \end{aligned} \right] \quad (2.32a)$$

$$\begin{aligned} \eta_{IR} = \frac{2y_1}{D_f} = & \left( 1 + \frac{D_p}{D_f} \right) + St\sqrt{c} \left[ \left( 1 + \frac{2y_1/D_f}{2y_2/D_f} \right) \left( 1 + \frac{2y_2}{D_f} - \frac{2y_1}{D_f} \right) \right] \\ & \times \left\{ 1 - \exp \left[ -\frac{1}{St\sqrt{c}} \left( 1 + \frac{2y_1/D_f}{2y_2/D_f} \right)^{-1} \right] \right\} - \left( 1 + \frac{2y_2}{D_f} - \frac{2y_1}{D_f} \right) \end{aligned} \quad (2.32b)$$

where  $y_1$  is the limiting streamline as in Figure 2.1 and  $y_2$  is some distance from the fiber surface. Note that  $y_1$  and  $y_2$  are the two unknowns. There is no interest in the value of  $y_2$ . The collision efficiency is obtained by solving for  $y_1$ .

An "exact solution" may be obtained by solving the next two second-order ordinary differential equations. Note that two second-order ordinary differential equations may be easily converted into four first-order ordinary differential equations and solved using an ordinary differential equation solving algorithm such as a fourth-order Runge-Kutta method:

$$\frac{d^2 z_1}{dt^{*2}} + \frac{dz_1}{dt^*} = -\frac{St}{2Ku} \left[ \begin{aligned} & \ln \left( 4(z_1^2 + z_2^2) \right) + c - 2c(z_1^2 + 3z_2^2) + \frac{z_2^2 - z_1^2}{z_1^2 + z_2^2} \\ & + \frac{1}{4} \left( 1 - \frac{c}{2} \right) \frac{z_1^2 - z_2^2}{(z_1^2 + z_2^2)^2} \end{aligned} \right] \quad (2.33a)$$

$$\frac{d^2 z_2}{dt^{*2}} + \frac{dz_2}{dt^*} = \frac{St}{2Ku} \left[ \frac{2z_1 z_2}{z_1^2 + z_2^2} - \left(1 - \frac{c}{2}\right) \frac{z_1 z_2}{2(z_1^2 + z_2^2)^2} - 4cz_1 z_2 \right] \quad (2.33b)$$

to be solved subject to the following boundary conditions:

$$z_1(0) = \frac{l}{2\sqrt{c}} \quad \frac{dz_1}{dt^*_{i=0}} = \frac{u_x(b, y_1)\tau}{D_f} \quad (2.34a)$$

$$z_2(0) = \frac{y_1}{D_f} \quad \frac{dz_2}{dt^*_{i=0}} = 0 \quad (2.34b)$$

Figure 2.7 shows plots of both the approximate solution and the exact solution. The maximum difference between the two efficiencies is about 75%, occurring in the vicinity of  $St = 0.1$ . Note how much better the model used by Sabnis follows the exact solution curve as compared to the approximation solution.

### 2.5.5 Other Collision Efficiency Models

Suneja and Lee (1974) derived an equation for isolated collision efficiency due to interception and inertial impaction:

$$\eta_{IR} = \frac{l}{\left[ I + \left( 1.53 - 0.23 \ln Re_f + 0.167 (\ln Re_f)^2 \right) \frac{1}{St} \right]^2} + \frac{2 I_p}{3 St} \quad (2.35)$$

for  $Re_f \leq 500$ . The complete Navier-Stokes equations were solved using a successive over-relaxation method to obtain the flow field around a fiber (Suneja and Lee, 1974).



The calculated flow field was then used in computing the particle trajectories and thereby the isolated collision efficiencies. According to this equation, the collision efficiency increases with decrease in Stokes number, increase in Reynolds number, and increase in the dimensionless particles size,  $I_p$ .

A second model investigated for isolated collision efficiency considering combined effects of interception and inertial impaction was the model developed by Ptak and Jaroszczyk (1990):

$$\eta_{IR} = \frac{(St - 0.75 Re_f^{-0.2})^2}{(St + 0.4)^2} + I_p^2 \quad (2.36)$$

Ptak and Jaroszczyk used a similar approach to that used by Suneja and Lee (1974) in deriving Equation (2.35).

A third model studied was Landahl and Herrmann's (1949) model for isolated collision efficiency due to interception and inertial impaction:

$$\eta_{IR} = \frac{St_c^3}{St^3 + 0.77 St_c^2 + 0.22} + I_p \quad (2.37)$$

Note that the only difference between Landahl and Herrmann's inertial impaction efficiency model, Equation (2.28), and their interception and inertial impaction model, Equation (2.37), is the added interception parameter,  $I_p$ .

Note that the three models discussed in this sub-section incorporate the relation of two mechanisms, interception and inertial impaction, using the simplified relation of Equation (2.14), as discussed in Section 2.3.5:  $\eta_{coll} = \eta_1 + \eta_2$ . Nonetheless, as illustrated

in Figure 2.7, Equation (2.30) implements the “non-simplified” relation of Equation (2.14) with good agreement to the exact solution presented by Flagan and Seinfeld (1988). The reader is reminded that both relations are approximate methods and that both relations are accepted practices within filtration efficiency modeling.

All models discussed in this sub-section are for isolated fiber efficiencies. The Ptak and Jaroszczyk (1990) solidity factor may be used to obtain the single fiber efficiencies accounting for neighboring fibers. A plot of these three isolated collision efficiencies along with Flagan and Seinfeld’s (1988) exact solution and the model used by Sabnis is provided in Figure 2.8. Note that for the large range of Stokes numbers, the model used by Sabnis, Equation (2.30), closely follows the exact solution and, for this reason, is by far the best model to use.

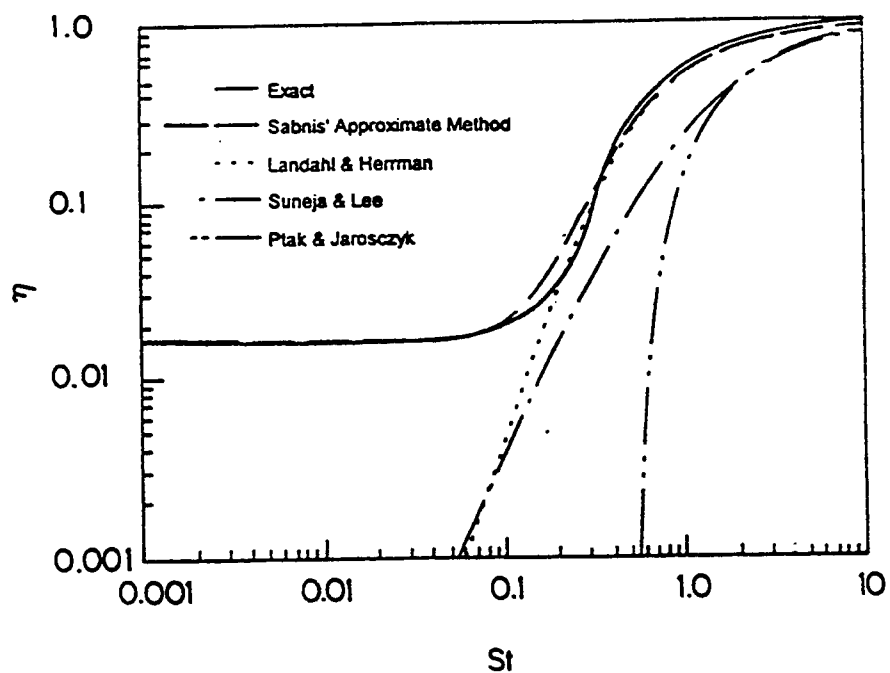


Figure 2.8 Comparison of Flagan and Seinfeld's (1988) Exact Solution to Isolated Collision Efficiency Models (Newman, 1994)

## 2.6 Adhesion and Retention of Captured Particles

### 2.6.1 Discussion

Most of the theory described so far has assumed that particles adhere perfectly to fibers on contact. Now the possibility of impact without capture is considered. Although some important parameters which determine particle adhesion and retention efficiency

have been investigated experimentally (Larsen, 1958; Krupp, 1967; Freshwater and Stenhouse, 1972; First and Hinds, 1976; Ptak and Jaroszczyk, 1990), very limited quantitative methods have been developed by which values of  $\eta_{adh}$  may be correlated or predicted (Wang and Kasper, 1991; Ptak and Jaroszczyk, 1990; Brown, 1993). There are two primary mechanisms of particle removal after contact: "bounce-off" or simple rebound after initial impact and "blow-off" or aerodynamic drag causing re-entrainment (Freshwater and Stenhouse, 1972; Brown, 1993). In the following sub-sections, to provide an understanding of adhesion and retention of particles, we shall discuss the principle forces of adhesion as applied to dry fibrous filters.

### 2.6.2 Adhesion Forces

By providing an understanding of adhesion forces and comparing recent publications on adhesion theories, it is hoped here to obtain some information on the adhesion mechanisms prevailing. As discussed by Krupp (1967), there are three types of forces of importance in the adhesion of dust particles to filter fibers:

- (1) van der Waals forces
- (2) electrostatic forces caused by excess charges
- (3) surface tension or capillary forces between liquid bridges

Van der Waals forces are interaction forces based on the attraction of dipoles between the atoms of the adhered surfaces. These interaction forces between atoms occur due to fluctuating electric dipole moments within the atoms. An electric field is induced by an

atom which then attracts a dipole of a neighboring atom. As presented by Loffler (1966; 1968) and Brown (1993), van der Waals forces between macroscopic bodies are expressed in terms of the Hamaker constant,  $A_1$ :

$$F = \frac{A_1 R_a}{6z_o^2} \quad (2.38)$$

where  $R_a$  is the radius of the surface asperity that is closest to the fiber, and  $z_o$  is the distance between the particle and the fiber. The Hamaker constant,  $A_1$ , depends on the number of atoms participating in the force transfer and upon their polarizability. This constant is not always easy to determine. Brown (1993) provides a listing of Hamaker constants for metallic and non-metallic materials.

Electrostatic forces are based on electrical excess charges of the adhered surfaces, particle or fiber. As given by Brown, the force of adhesion due to an electrostatic charge  $q$  of a particle with radius  $R_p$  is:

$$F = \frac{q^2}{16\pi\epsilon_o R_p \delta} \frac{\ln\left(1 + \frac{\delta}{z_o}\right)}{\left[\gamma + \frac{1}{2} \ln\left(\frac{2R_p}{z_o}\right)\right] \left[\gamma + \frac{1}{2} \ln\left(\frac{2R_p}{z_o + \delta}\right)\right]} \quad (2.39)$$

where  $\delta$  is the depth at which the charge density falls to  $e^{-1}$  of that at the surface,  $\epsilon_o$  is the permittivity of free space,  $\gamma$  is Euler's constant. Electrostatic adhesion charges can initially induce increased deposition of the dust particles on the fibers, if of sufficient magnitude and appropriate polarity (Loffler, 1966). However, experiments have shown that maximum adhesion forces due to electrostatic charges are much weaker (by a factor

of 100) than the measured total adhesion forces. Note that Equation (2.38) represents the adhesion force due to electrostatic charges once contact has taken place and does not represent the “collection force” induced by the electrostatic attraction mechanism discussed in Sub-Section 2.3.4.

Surface tension or capillary forces act in liquid bridges between the adhered surfaces. With sorption layers which are freely mobile, wedges of liquid can form at the contact points between particles and fibers. An underpressure prevails in these wedges. Figure 2.9 shows a sphere attached to a plane by means of a liquid bridge. If the angle of contact is zero, the force between them as expressed by Brown is:

$$F = 4\pi\tau R_p \quad (2.40)$$

where  $\tau$  is the boundary-surface tension of the liquid bridge and is independent of the particle radius. A calculation based on simple geometry yields that the force is independent of the amount of liquid present, so long as, a complete bridge is formed (Brown, 1993). As the area of contact decreases, the curvature increases, and the internal pressure of the liquid bridge also increases.

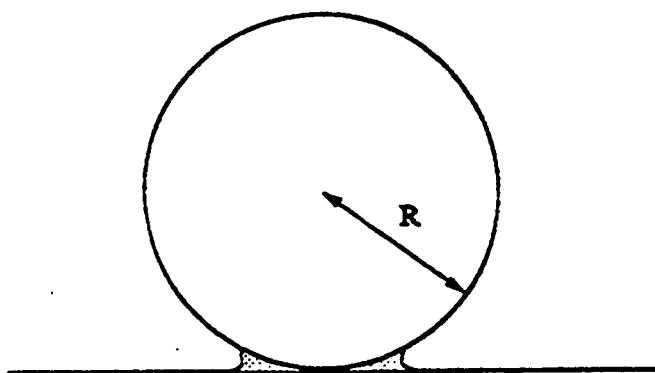


Figure 2.9 Sphere attached to a plane by capillary forces (Brown, 1993)

### 2.6.3 Conditions Affecting Particle Retention

Experimental measurements have shown that adhesion between particles and fibers is primarily caused by van der Waals forces (Loffler, 1966; 1968; 1971b). However, at relative humidities greater than 80%, the mechanism of adhesion most likely to prevail is that of capillary adhesion due to surface adsorbed water (Freshwater and Stenhouse, 1972, Brown, 1993). Adhesion forces are stronger when acting on large particles, as shown by Figure 2.10. However, larger particles are more likely to bounce at impact and the drag exerted on larger particles by an airflow is greater, which may allow larger

particles to be detached at a lower air flow (Brown, 1993). It is also easier to detach particles from thick fibers than from thin ones (Larsen, 1958).

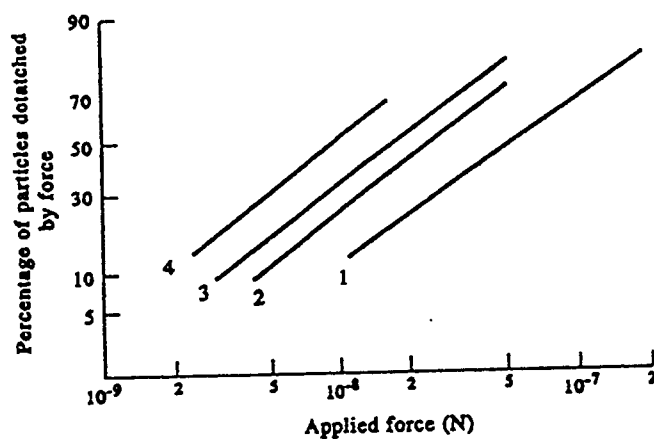


Figure 2.10 Distribution of Adhesion Energies of Quartz Particles Deposited at a Filtration Velocity of 0.42 m/s on Polyamide Fibers: (1) 15.1  $\mu\text{m}$  Particles; (2) 10.3  $\mu\text{m}$  Particles; (3) 8.3  $\mu\text{m}$  Particles; (4) 5.1  $\mu\text{m}$  Particles (Brown, 1993).

Dahneke suggests that for maximum retention ability, filters should contain fibers of small diameter made of material with low Young's modulus (Dahneke, 1971). Such a filter would have the best ability to capture the full range of particles sizes including the large solid dust particles. The degree of adhesion does not appear to depend on the hardness of the particles being filtered (Brown, 1993). Increasing relative humidity tends to improve particle adhesion due to slightly softer fibers and an increase in the degree of surface contact. Dahneke suggests that the flow velocity through the filter should not be too high, although, to catch the large particles by inertial interception, the flow velocity cannot be too low either. Furthermore, he indicates that the decrease of fiber diameter has two strong influences on the capture of large particles (Dahneke, 1971): lowers the



velocity range in which inertial interception is effective and raises the velocity at which the onset of bouncing occurs.

The adhesion of particles to fibers is greater for particles that have been captured at a higher filtration velocity. These particles captured at higher velocities are slightly tighter bound and often very difficult to remove. It has been stated by many investigators that the air velocity needed to re-entrain particles is several times the filtration velocity (up to 10 times for 50% removal): "Particle detachment is more likely to occur at the moment of impact, and it can be reasonably concluded that particles that do not initially bounce are unlikely to be re-entrained by the air flow from which they were captured," (Brown, 1993). Many investigators dating as far back as the 1950's have concluded similar findings that, although bounce may occur, blow-off is unlikely to occur: "Probably the most important point to note from these experiments is that no particles were removed from the fibers at air flows such as are used in commercial filters . . . (Larsen, 1958)."

#### *2.6.4 Ptak and Jaroszczyk Adhesion Model*

Although much work has been conducted on adhesion theory and adhesion measurements, only very limited quantitative prediction methods for  $\eta_{adh}$  are available (Wang and Kasper, 1991; Ptak and Jaroszczyk, 1990; Brown, 1993). The only authors known to have developed any correlation or model in predicting particle to fiber adhesion efficiencies are Wang and Kasper (1991) and Ptak and Jaroszczyk (1990).

The Wang and Kasper adhesion model is based on a wide range of actual empirical data and data extrapolated down to the molecular range. For a known value of impact velocity to critical velocity (maximum impact velocity above which bounce occurs) ratio, an adhesion efficiency may be determined from their universal curve, independent of particle size, specific adhesion energy, and other operating variables, assuming a Boltzmann velocity distribution (as an alternative to the Kuwabara flow field.) However, they stress that their curve is only valid for a particle range of 0.1 to 10.0 nm (0.01  $\mu\text{m}$ ). Particles greater than 0.01  $\mu\text{m}$  have a mean impact velocity significantly below their critical velocity; hence, most collisions are effective and  $\eta_{adh}$  approaches 1.0 as expected in classic filter efficiency theory (Wang and Kasper, 1991). For larger particles, greater than a few microns, particle bounce following impaction decreases the filter efficiencies (Wang and Kasper, 1991). The Wang and Kasper model is best suited for membrane filters where diffusion and interception prevail over inertial impaction.

Ptak and Jaroszczyk (1990) recognized the importance of distinguishing the difference between collection efficiency and collision efficiency. The difference is associated with the momentum of solid dust particles and their adhesion to the fiber surface. Collection efficiency refers to the amount of particles collected, adhered, and retained by the fibers, whereas, collision efficiency refer to the amount of particles merely making contact with a fiber. Referring back to Equation (2.5), Ptak and Jaroszczyk refer to  $\eta_{adh}$  as the adhesive probability factor:

$$\eta_s = \eta_{coll}\eta_{adh}$$

By considering common variables and parameters used in calculating and predicting adhesion forces, Ptak and Jaroszczyk concluded that they may be used to determine the adhesion probability factor or  $\eta_{adh}$ . Thus, the general dependence of adhesion probability is as follows:

$$\eta_{adh} = \eta_{adh}(\rho_p, D_p, u_\infty, D_f, \mu) \quad (2.41)$$

where  $\rho_p$  is the particle density. Using dimensional analysis, they incorporated the Reynolds number of the particle, similar to Equation (2.4), and the Stokes number as in Equation (2.24):

$$Re_p = \frac{D_p u_\infty \rho_p}{\mu} \quad (2.42)$$

and

$$St = \frac{R_p^2 \rho_p u_\infty}{9 \mu R_f}$$

By definition, the adhesion efficiency must fall in the range  $0 \leq \eta_{adh} \leq 1.0$ . Hence, Ptak and Jaroszczyk expressed this range as:

$$\eta_{adh} = \frac{\alpha_o}{(Re_p St)^{b_o} + c_o} \quad (2.43)$$

where the constants may be determined experimentally, such that,  $\alpha_o = c_o$  and  $b_o > 0$ .

The final form of the Ptak and Jaroszczyk adhesion model is given as:

$$\eta_{adh} = \frac{190}{(Re_p St_c)^{0.68} + 190} \quad (2.44)$$

The authors obtained good correlation between experimental results and their adhesion model, Equation (2.44), using their Interception and Inertial model of Sub-Section 2.5.5, Equation (2.36), with a solidity factor.

## 2.7 Pleated Air Filters

### 2.7.1 Discussion

All of the filtration theories and models discussed in previous sections have been based on a flat sheet of filtering media. However, most filters used in a variety of industrial applications are pleated. A pleated filter is more compact and allows for more filtration area. Increasing the filtration area allows more particles to be captured in a fixed volume and so reduces the filtration velocity which in turn reduces the pressure drop at a fixed volume (Brown, 1993). It is understood that the pressure drop should decrease as the number of pleats per unit length is increased. However, eventually the restricted space between pleats will cause the pressure drop to rise again due to the increased viscous drag (Chen et al., 1994). Although there are limited studies on pleated filter optimization, Chen et al. developed an analytical model which compares favorably with Yu and Goulding's (1992) semi-analytical model. Studies conclude that an optimum pleat count for minimum pressure drop exists at a certain pleat height for a specific filter medium type (Brown, 1993; Chen et al., 1994).

### 2.7.2 Pleated Surface Area

It is common to base all filtration theories and calculations on the surface area of the filtering media. Figure 2.6 illustrates a filter pleat geometry. The element of width  $x$ , length  $y$ , and thickness  $h$  represents an elemental filter bed. The elemental surface area,  $a_e$ , is defined by simple geometry:

$$a_e = x \sqrt{\left(\frac{2hy}{p}\right)^2 + y^2} \quad (2.45)$$

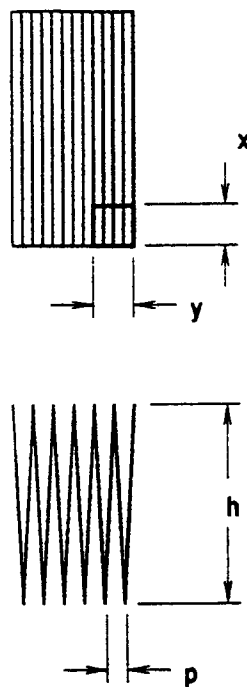


Figure 2.11 Filter Pleat Geometry (Newman, 1994)

### 2.7.3 Air Velocity Inside Pleated Filters

Although recent computational fluid dynamic calculations suggest non-uniform flow near the pleats of a filter (Cai, 1993; Tebbutt, 1995), for simplicity, it is assumed here that the velocity is uniform. Assuming uniform velocity, the velocity near the filter pleats,  $u$ , is obtained through simple geometry and continuity,:

$$u = u_o \frac{xy}{a_e} \quad (2.46)$$

where  $u_o$  is the axial velocity upstream of the filter. The velocity  $u_o$  is easily obtained experimentally, just upstream of a filter. Note that the velocity  $u$  as in equation (2.3) of Sub-Section 2.2.2 refers to the velocity upstream of the filter media; or rather, the velocity near the filter pleats. From Equation (2.3) the velocity within the filter media is obtained:

$$u_\infty = \frac{u}{1-c}$$

in terms of the measured upstream velocity,  $u_o$ :

$$u_\infty = \frac{u_o xy}{a_e(1-c)} \quad (2.47)$$

The air velocity inside the filter media is greater than the velocity near the filter pleats,  $u_\infty > u$ , and the measured axial velocity upstream of the filter is greater than the air velocity near the filter pleats,  $u_o > u$ . The filter media velocity required by all of the filtration efficiency models implemented was obtained directly from the measured axial velocity upstream of the filter using Equation (2.47).

## 2.8 Methodology

### 2.8.1 Typical Properties of Automotive Air Filtration Paper

Automotive air filtration media used in paper filters is typically cellulose wood pulp comprised of southern softwood kraft, SSK, mercerized SSK, northern and southern or eucalyptus hardwood kraft wood pulps. As obtained from Ahlstrom Filtration, the typical mixtures in automotive air filter paper range from a position of 80 percent mercerized SSK, 15 percent SSK, and 5 percent hardwood (for a very high permeability grade) to 50 percent hardwood SSK, 25 percent SSK, 25 percent hardwood (for a very high efficiency grade). The average fiber diameters as specified by Ahlstrom Filtration are provided in Table 2.1. Also provided by Ahlstrom Filtration is a range of typical properties for auto air filtration media. Refer to Table 2.2.

Table 2.1

Average Fiber Diameters Used in Automotive Air Filtration Paper

Fiber Type	Average Fiber Diameter [ $\mu\text{m}$ ]
SSK	45
Mercerized SSK	40 - 45
Northern US, Southern US, Eucalyptus Hardwood Kraft Pulp	18 - 30

Table 2.2  
 Typical Properties for Automotive Air Filtration Paper

Property	Property Range
Frazier Air Permeability (number of ft <sup>3</sup> /minute of air to pass through one ft <sup>2</sup> of media at a pressure drop of 0.5 inches of H <sub>2</sub> O)	60 - 120 [cfm]
Basis Weight	110 - 165 [g/m <sup>2</sup> ]
Media Thickness	450 - 700 [μm]
Unsaturated Paper Density	0.18 - 0.22 [g/cc]

### 2.8.2 Fiber Diameter

Most filtration efficiency models are based on the assumption that all fibers in a filter bed are of uniform diameter. With this in mind, a uniform equivalent fiber diameter must be determined and justified. Sabnis (1993) suggested that a uniform equivalent fiber diameter may be determined by calculating a weight averaged fiber diameter based on the composition of high permeability grade and high efficiency grade filters obtained from Ahlstrom filtration. Sabnis used the mean filter diameter of the diameter range presented in Table 2.1. Sabnis obtained  $D_f = 43.575 \mu\text{m}$  for high permeability grade filters and  $D_f = 39.125 \mu\text{m}$ , for high efficiency grade filters. Sabnis assumed that the Purolator



AF3192 filter is of a very high efficiency grade, and simply used a uniform equivalent fiber diameter of 38.0  $\mu\text{m}$ .

Licht (1980) provides an alternative method of determining a uniform equivalent diameter based on the weight fraction of the composition:

$$\log D_f^2 = \sum_{j=1}^n x_j \log D_{fj}^2 \quad (2.48)$$

Using this expression with the composition presented earlier gives a uniform equivalent diameter of 43.235  $\mu\text{m}$  for high permeability grade and 39.910  $\mu\text{m}$  for a high efficiency grade.

As referenced in Dorman (1966) and Licht (1980), Davies suggests that an "effective fiber diameter" may be determined based on the pressure loss through the filter media at a given flowrate:

$$D_{ef} = \sqrt{\frac{\mu Q h 70 c^{1.5} (1 + 52 c^{1.5})}{A \Delta P}} \quad (2.49)$$

This equation is applicable for high packing densities,  $c > 0.02$ . The effective fiber diameter is usually greater than that measured under the microscope (Dorman, 1966; Brown, 1993). Before an effective fiber diameter may be determined, the packing density of the filter must be known. The packing density and how it was determined is discussed in the following sub-section. An effective fiber diameter corresponding to the calculated packing density is given.

### 2.8.3 Packing Density

The dimensionless packing density or packing fraction,  $c$ , defined as the volume fraction of the fibers, is related in Equation (2.1):

$$c = \pi R_f^2 L = 1 - P_o$$

assuming the media consists of fibers with uniform radius,  $R_f$ . In order to find  $c$ , it is necessary to determine the density of the fibers,  $\rho_f$  (Davies, 1973). Then, as in Equation (2.1):

$$c = \frac{\text{Volume of Fibers}}{\text{Volume of Filter}} = \frac{w/\rho_f}{Ah} = 1 - P_o \quad (2.50)$$

However, the actual fiber density of a multi-component filter is not easily measured with high accuracy. Thus, an alternate method of determining the packing density of the filter,  $c$ , was incorporated.

In measurements of the resistance of filters, a unique dimensionless function exists (Davies, 1973; Brown, 1993):

$$f(c) = \frac{\Delta P A R_f^2}{\mu Q h} \quad (2.51)$$

This equation embodies the fundamental law of filtration theory, Darcy's Law, which states that the pressure across a filter is proportional to the rate of fluid flow through the filter. The quantity  $Qh/A\Delta P$  is referred to as the permeability and is a unique function of the packing density and fiber radius. Many correlations among a range of porous media have been developed and described by Equation (2.51). A very extensive study was

carried out by Jackson et al. (1986) in which the measurements for a variety of physical systems, both liquids and gases, by a large number of authors were plotted together. Figure 2.12 was taken from Brown (1993) and shows the envelope curves for  $f(c)$  based on the data comparison by Jackson et al. The bold line is the empirical formula developed by Davies (1973):

$$f(c) = 16c^{1.5}(1.0 + 56c^{3.0}) \quad (2.52)$$

This equation gives a good description of typical results expected at very low packing fractions,  $c < 0.02$ . Referring to Figure 2.12, the values of packing fraction vary by four orders of magnitude and the values of  $f(c)$  by almost six. It is clear that a strong correlation exists between  $c$  and  $f(c)$ .

In efforts to determine the packing density of the Purolator AF3192 filter, a pressure drop of 5767 Pa (23.15 in. H<sub>2</sub>O) was measured at an actual flow rate of 0.06 m<sup>3</sup>/s (126.5 cfm) through a 102 mm (4.0 in.) diameter section of flat filter media. Equation (2.51) was used to calculate a value of  $f(c)$  assuming a weight averaged uniform equivalent fiber diameter of 39.125 μm for a high efficiency grade filter, as estimated previously. (Refer to Sub-Section 2.8.2 Fiber Diameter.) At a value of  $f(c) = 23.303$ , a packing density range of 0.2113 to 0.5623 was obtained from Figure 2.12. The midpoint of this range corresponds to a packing density of 0.3447. A packing density of  $c = 0.345$  was used in all work presented in this thesis.

Previous work on this project has assumed a packing density of 0.23 based on an assumed Frazier air permeability of 150 cfm defined as the number of ft<sup>3</sup>/minute of air to

pass through one ft<sup>2</sup> of media at a pressure drop of 0.5 in. H<sub>2</sub>O (Sabnis, 1993; Newman, 1994). By conducting actual pressure measurements through the filter media, an actual permeability value was calculated eliminating the need to assume some value of Frazier air permeability. Consequently, it is understood here, that the determined packing density of  $c = 0.345$  better represents the true packing density of the filter media as compared to the previously assumed value of  $c = 0.23$ .

With the packing density known, an effective fiber diameter may be calculated using Equation (2.49):  $D_{ef} = 51.78 \mu\text{m}$ . This effective fiber diameter is higher than the average fiber diameters listed in Sub-Section 2.8.1. However, this value is realistic. The effective fiber diameter is typically higher than that measured under a microscope due to likely reasons being that in real filters the fibers are not all perpendicular to the airflow and the real fiber structures are not uniform (Brown, 1993).

In summary, for the Purolator AF3192 filter, a packing density value of  $c = 0.345$  and an effective fiber diameter of  $D_{ef} = 51.78 \mu\text{m}$  were used in all work presented.

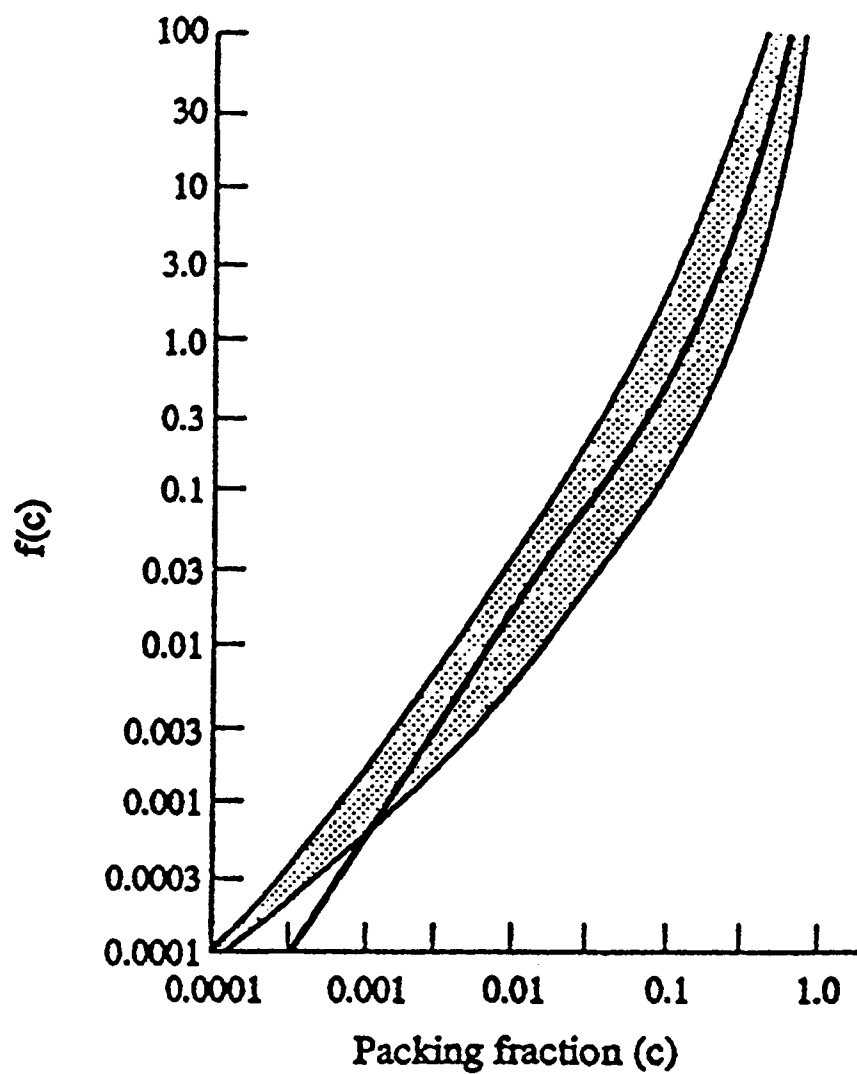


Figure 2.12 Envelope Curves for  $f(c)$  Versus Packing Fraction,  $c$ , with Davies' (1973) Very Low Packing Fraction Empirical Formula Line Curve, Equation (2.52), (Brown, 1993).

#### 2.8.4 Program "EFFMODEL.FOR"

The FORTRAN program EFFMODEL.FOR was developed to incorporate models presented in this chapter. EFFMODEL.FOR incorporates an individual efficiency component (interception, inertial impaction, and adhesion) subroutine, EFFRIA, a single fiber efficiency subroutine, SINGLEE, and an elemental fiber efficiency subroutine, ELEMENT. Program EFFMODEL was developed and implemented to obtain all computational results presented in Chapter V Filtration Efficiencies. All computations were conducted on Microsoft Programmer's WorkBench 1.10, 1990. A complete listing of the main program and subroutines source code is provided in Appendix B. Sample input and output files are provided in Appendix C.

Program EFFMODEL requires the user to supply an input file of upstream filter velocities arranged in ascending order corresponding to the 66 data point locations specified in Figure 3.7 of Chapter III Experimental Setup. Refer to the sample input file provided in Appendix C. Related elemental areas are tabulated per data point.

Subroutine EFFRIA implements three efficiency models for interception, inertial impaction, and adhesion. The interception model implemented is the semi-empirical model developed by Lee and Liu (1982b), as in Equation (2.23):

$$\eta_R = \frac{1 - c}{Ku} \frac{I_p^2}{1 + I_p}$$

The inertial impaction model implemented is the isolated fiber efficiency model developed by Landahl and Herrmann (1949), Equation (2.28). This model was corrected using the

Ptak and Jaroszczyk (1990) solidity factor of Equation (2.6). Thus as in Equation (2.29), the final form of the inertial impaction model is:

$$\eta_I = \frac{SF \cdot St_c^3}{St_c^3 + 0.77St_c^2 + 0.22}$$

The particle adhesion model implemented is the model developed by Ptak and Jaroszczyk, as in Equation (2.44):

$$\eta_{adh} = \frac{190}{(Re_p St_c)^{0.68} + 190}$$

At large particle diameters, the interception and the inertial impaction models may exceed unity. This is possible for large values of  $I_p$  such that  $R_p + R_f > b$ . For these conditions, the particles pass outside the Kuwabara flow field zone of radius  $b$ ; thus, the filtration models are no longer applicable. It may further be noted that, although the individual component efficiencies may exceed a value of one, the elemental fiber efficiency defined by Equation (2.11) will never exceed unity. Nonetheless, in efforts to avoid negative penetration values, all models implemented in subroutine EFFRIA were limited to efficiencies of unity or lower.

Subroutine SINGLEE implements the single fiber collection efficiency model, as in Equation (2.5):

$$\eta_s = \eta_{coll} \eta_{adh}$$

where  $\eta_{coll}$  is the collision efficiency, and  $\eta_{adh}$  is the retention or adhesion efficiency.

The collision efficiency is defined as in Equation (2.14) for interception and inertial impaction:

$$\eta_{coll} = 1 - (1 - \eta_R)(1 - \eta_I) \quad (2.53)$$

Thus, the final form of Equation (2.5) is as follows:

$$\eta_s = [1 - (1 - \eta_R)(1 - \eta_I)]\eta_{adh} \quad (2.54)$$

Single fiber efficiencies were calculated for both perfect adhesion and non-perfect adhesion as described by the Ptak and Jaroszczyk (1990) adhesion model, Equation (2.44).

Subroutine ELEMENT calculates the elemental fiber efficiency based on the single fiber efficiency due to interception, inertial impaction, and perfect and non perfect particle adhesion. This elemental fiber efficiency model is defined in Equation (2.11):

$$\eta_e = 1 - \exp\left(-\frac{2c\eta_s h}{\pi(1-c)R_f}\right)$$

Figure 2.13 is a plot of the individual efficiencies obtained from program EFFMODEL for a particle diameter of 2.5  $\mu\text{m}$ . Note that the models follow the typical characteristics of filtration efficiencies as illustrated in Figure 2.5. Measured upstream velocities presented within this thesis typically range from 0.0 to less than 7.0 m/s. The interception efficiency does not vary with velocity. With increasing upstream velocities, the inertial impaction efficiency eventually reaches unity and the adhesion efficiency approaches zero. For larger particle diameters, the peaks and end bounds of the curves



represented in Figure 2.5 and Figure 2.13 are achieved at lower velocities. Similarly, with a smaller fiber diameter and a smaller packing density, as used by Sabnis, the peaks and end bounds of the curves are achieved at lower velocities. Refer to Figure 2.14.

Within the main program, overall filter efficiencies are calculated assuming a uniform particle concentration per unit volume using Equation (2.13):

$$\eta_f = 1 - \frac{\sum_{i=1}^n [P_e a_e u_{\infty}]_i}{\sum_{i=1}^n [a_e u_{\infty}]_i}$$

Note that a uniform particle concentration does not imply a uniform volumetric flow rate of particles.

The user may specify an optional SAE fine test dust, SAE coarse test dust, or a simple particle radius input. The SAE test dust distributions refer to the two grades of particle size distributions by percent weight listed in Table 1.1. Overall elemental efficiencies and overall total elemental efficiencies for the specified SAE test dusts are calculated. A total of four output files are generated: VELSTRE, EFFCOMP, SINGELEM, and SAEDUST (when applicable). Refer to Appendix C for sample output files.

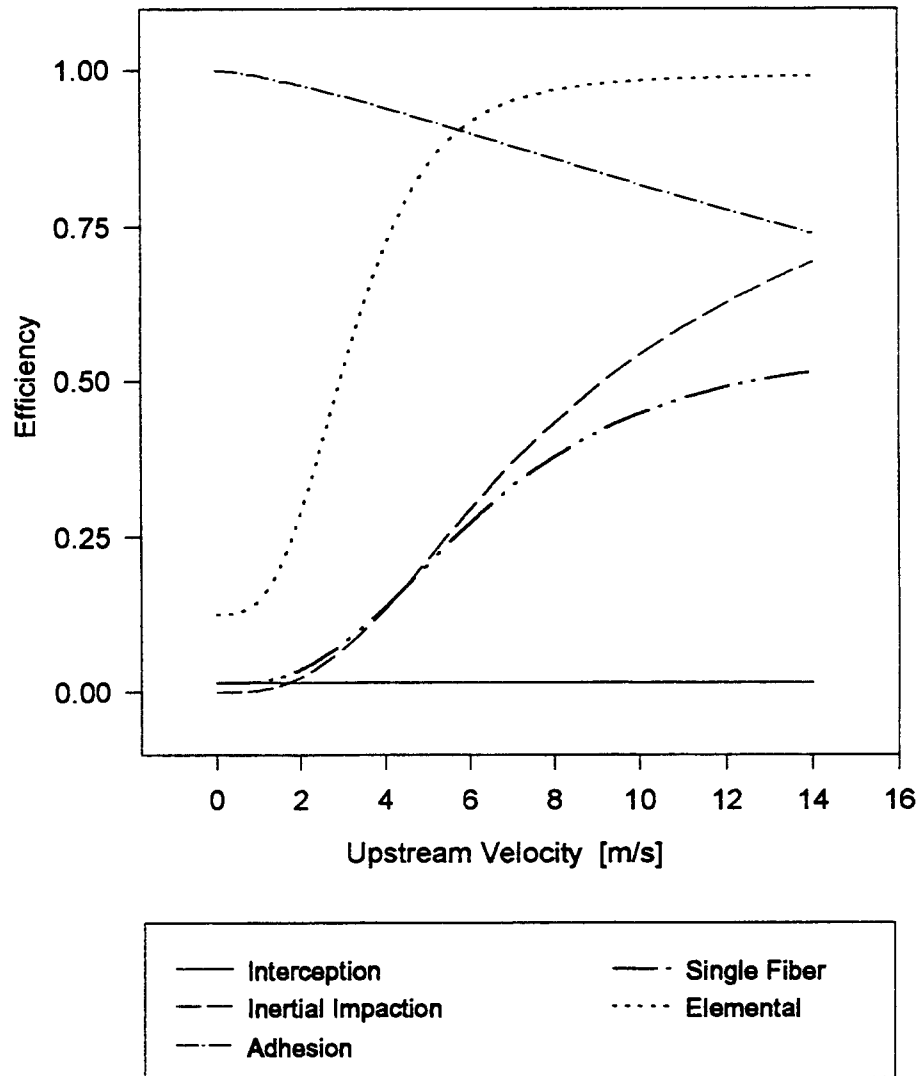


Figure 2.13 Efficiency Curves Obtained from Program EFFMODEL  
 at  $R_p = 1.25 \mu\text{m}$ ,  $c = 0.345$ ,  $D_{ef} = 51.78 \mu\text{m}$ .

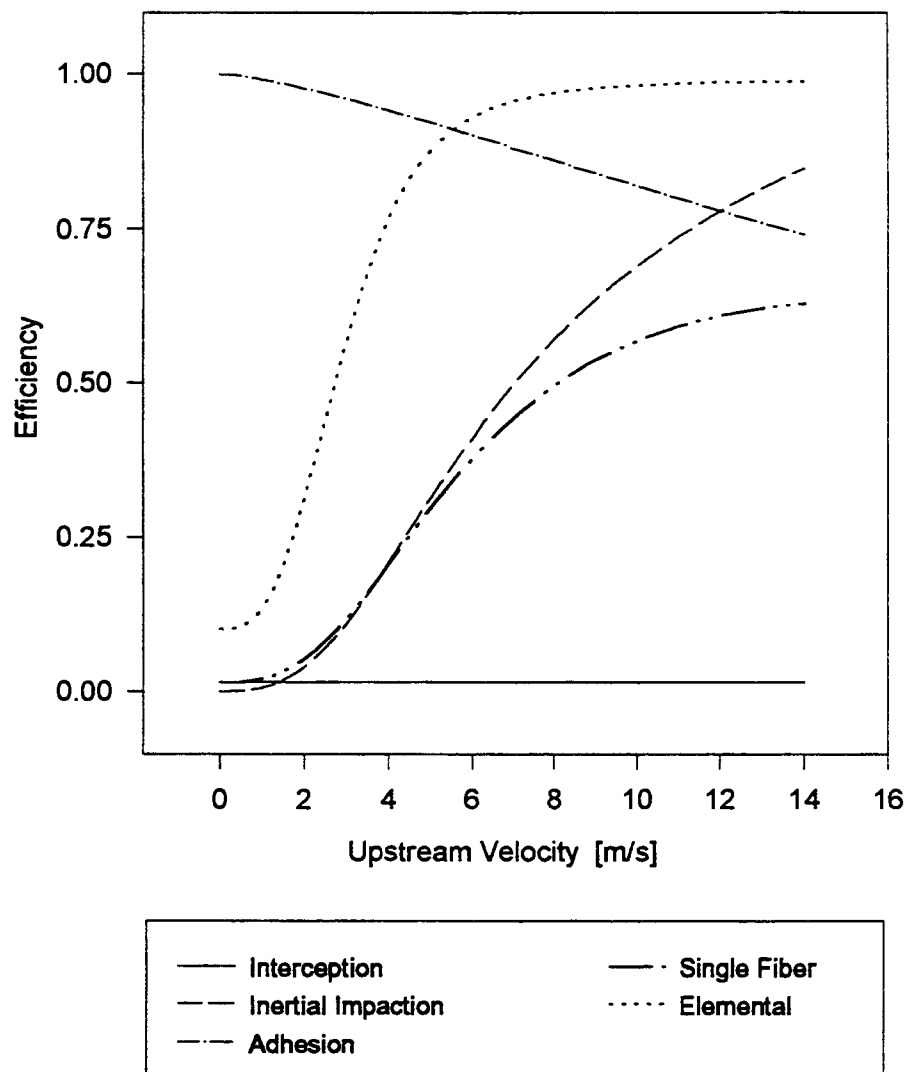


Figure 2.14 Efficiency Curves Obtained from Program EFFMODEL with Parameters Used by Sabnis (1993),  $R_p = 1.25 \mu\text{m}$ ,  $c = 0.230$ ,  $D_f = 38.0 \mu\text{m}$ .

## CHAPTER III

### EXPERIMENTAL SETUP

#### 3.1 Experimental Apparatus

An experimental setup was assembled to pass air flow into the SAE J726 test housing and through the filter specimens. Laser Doppler Velocimetry, LDV, was used to measure the velocities of the flow field at two separate upstream horizontal planes. A schematic of the experimental apparatus is shown in Figure 3.1. The air flow was drawn through the test housing by a downstream centrifugal multistage exhauster (also referred to as a blower). The centrifugal multistage exhauster has a maximum flow rate of 1000 scfm and was set to run at the SAE specified test flow rate of 125 scfm. Upstream of the apparatus, a 6-Jet atomizer (TSI Incorporated MODEL 9306) was used to generate the 0.966  $\mu\text{m}$  Polystyrene Latex, PSL, aerosol particles used for seeding. A separate compressed air supply passed through the atomizer. In efforts to avoid introducing water droplets and condensation into the flow stream, the PSL particles were heated with a fan heater just after leaving the atomizer. A flow distributor chamber was constructed in efforts to redirect the flow stream and avoid potential flow swirls prior to entering the plexiglas tubing upstream of the test housing. It was found to be convenient to mount the tube to housing flanges with four quick release clamps. A wooden sphere used to obstruct the inlet flow, in efforts to provide a more uniformly distributed flow, was

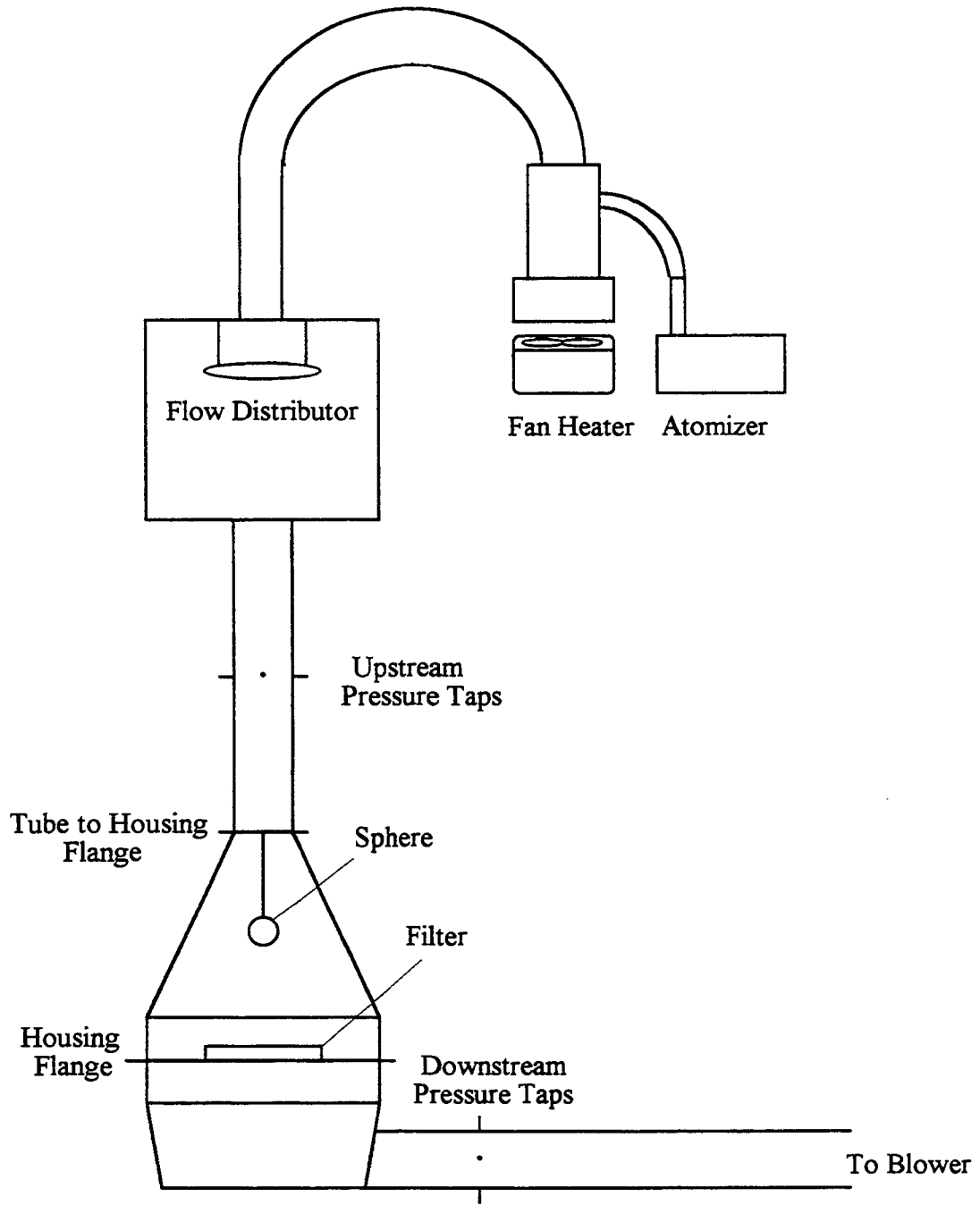


Figure 3.1 Experimental Apparatus

easily mounted and suspended from the tube to housing flanges, as shown in Figure 3.1. The SAE test housing was constructed as specified in Figure 1.2 using quarter inch Plexiglas. The filter specimen is centered and mounted between the top and bottom portions of the test housing, as shown in Figure 1.2. The housing is conveniently mounted with four easy release clamps securing both the housing and the filter specimen. The flow leaving the test housing entered a section of PVC pipe connected to the downstream blower. Pressure taps located both upstream and downstream of the test housing were used to monitor the differential pressure through the filter specimen.

The test housing was mounted on a stand allowing for adjustable vertical positioning. During actual testing, the test housing was stationary. The laser transceiver was mounted on a three axis automated traverse table. The horizontal translations were controlled by two stepper motors driven by a separate personal computer. Vertical translations were performed manually, allowing for measurements at separate horizontal planes.

### 3.2 Laser Doppler Velocimetry Diagnostics

The measurement instrument used in this experiment was a dual component laser Doppler velocimetry system incorporating fiber optics. A schematic of the laser Doppler velocimetry system is provided in Figure 3.2. A Coherent Innova 70-A, 4 watt, argon ion

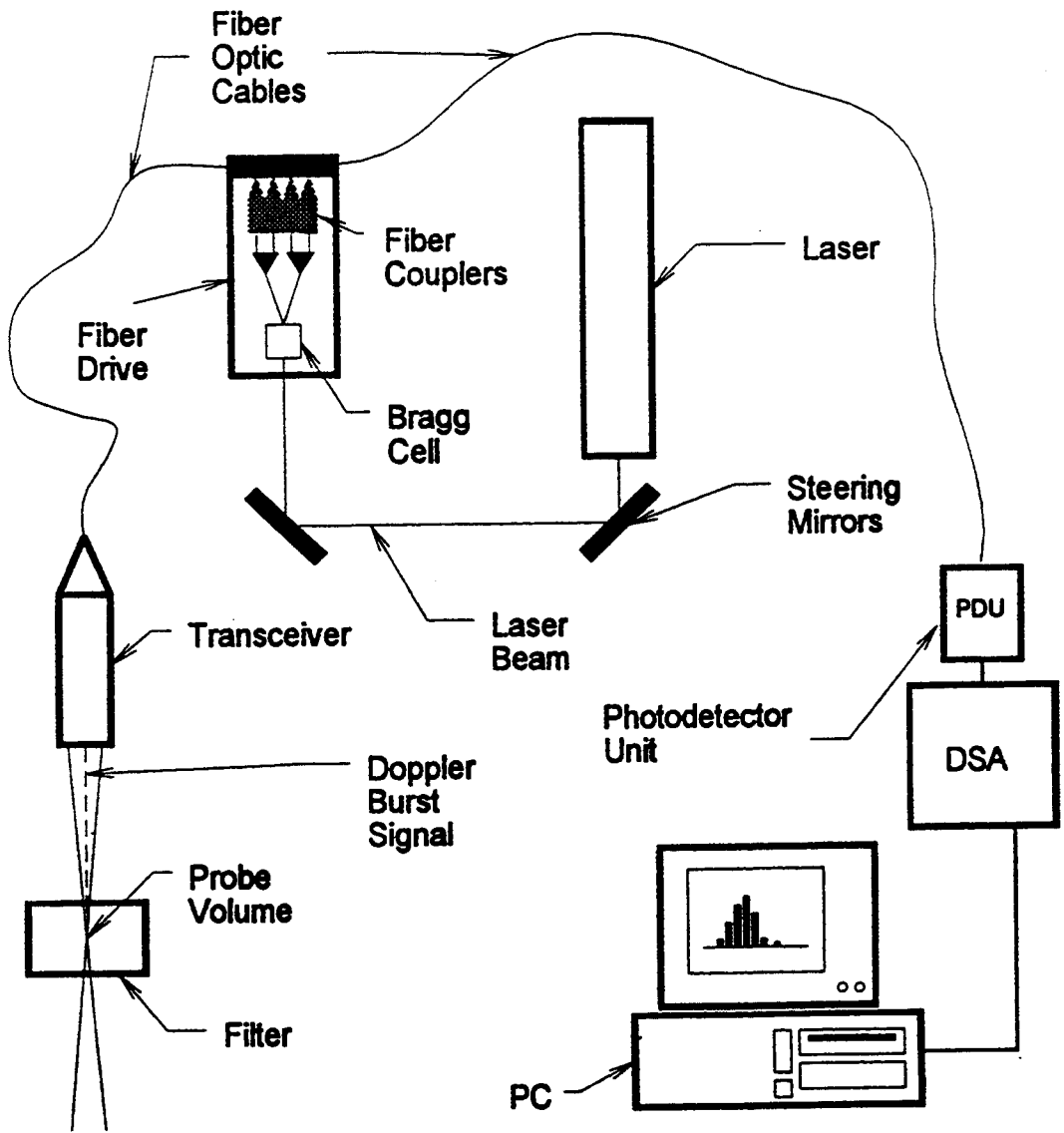


Figure 3.2 Schematic of the Laser Doppler Velocimetry System.

laser was operated at a wavelength of 488 nm. A Bragg cell within the system fiber drive applies a 40 MHz frequency shift to the beam. (Note that a Bragg cell will generate several ordered beams of multiple shifts: +80 MHz, +40MHz, 0MHz, -40MHz, -80MHz.) The frequency shifting produces a moving fringe pattern which eliminates directional ambiguity from velocity measurements of reversing flows. The 1st order, +40 MHz shifted, beam and the 0th order, non-shifted, beam produced by the Bragg cell are then separately split into two blue and two green beams of wavelengths 488 nm and 515 nm, respectively. This gives a total of four beams, one shifted and one unshifted beam for each color. An Aerometrics, Inc. Doppler Signal Analyzer, DSA, processing Doppler bursts was used and operated by a 486DX/2-66 MHz personal computer. For ease in managing and organizing the DSA processed data, I developed a simple program to select and arrange the off line DSA data series output. A source code listing of this program is provided in Appendix D Source Code Listing of PICKDATA.FOR.

Within the fiber drive, the four beams are aligned by the fiber couplers and transmitted to the fiber optic transceiver through separate fiber optic cables. The fiber optic transceiver both focuses the four beams and collects back-scattered light reflected by the seeding particles passing through the probe volume. The transceiver has a 500 mm focal length lens producing a probe volume 737  $\mu\text{m}$  in length and 66  $\mu\text{m}$  in diameter. The collected light is transmitted through a fifth fiber optic cable to the photodetector unit. The photodetector unit contains two photomultipliers one sensing the detected light from the green beams and the other sensing the detected light from the blue beams. The two



photomultipliers translate the detected light into an analog voltage signal and send it to the DSA processing system. A complete listing of the DSA processing system and other equipment used is provided in Section 3.6 Equipment Listing.

### 3.3 Principles of Laser Doppler Velocimetry

The scattered light signal, called the Doppler burst signal, contains intensity maximas and minimas. An example of a raw Doppler burst is given in Figure 3.3. The signals are a result of the seeding particles passing through the probe volume and crossing the brighter and darker bands of the interference fringe pattern of the beam intersections. The low frequency component of the signal is the pedestal. The pedestal is created when the particle passes through the Gaussian intensity distribution of the laser beams, resulting in a low frequency signal. The Doppler bursts are superimposed on the pedestals and caused by the seeding particle passing through the interference fringe pattern of the beam intersections, as described by Hall and Hiatt (1994). Other authors may consider the pedestals as part of the Doppler burst.

A diagram illustrating a particle passing through a probe volume is provided in Figure 3.4. The fringe spacing,  $d$ , is a function of the beam crossing angle and the laser beam wavelength. The photomultipliers translate the detected light signals to an analog voltage signal. The LDV Doppler Signal Analyzer detects the Doppler bursts and

performs a Fast Fourier Transform, FFT, of the digitized burst signal. The DSA processor performs validation tests on the individual spectra, rejecting low quality noisy data. The peak frequency in the spectrum resulting from the FFT may be considered to be the rate at which the particle is crossing the interference fringes in the probe volume. With the Doppler frequency shift,  $f$ , known and the fringe spacing,  $d$ , known from the LDV's optical parameters, the velocity of the particle, and hence the velocity of the air stream, is obtained:

$$V = fd \quad (3.1)$$

The frequency shifting producing the moving fringe pattern eliminates directional ambiguity from velocity measurements of reversing flows. The measurement of reversing flows is a strong advantage in that it does not require prior knowledge of the complex velocity flow field directions. No calibration of the LDV system is needed. Another advantage of using an LDV system is that the flow is not disturbed. However, seeding particles are required and caution must be used in selecting a particle and a particle size which ensures that the particle is large enough to provide a reflecting light signal yet small enough to follow the flow without disrupting the flow stream. The back-scatter arrangement allows the transeiver to serve as both focusing beam optics and light collecting optics.

The disadvantages of using an LDV system include that the apparatus must allow for light to be transmitted and reflected easily. Thus, the apparatus in which velocity measurements are to be conducted must be constructed of transparent material with

uniform transparency to pass the laser beam and to receive the reflected signal. Furthermore, for large wall angles displacement of a transmitted light beam due to material refraction and the incidence beam angle may not only distort the probe volume but may also displace the dual beam probe volumes to a point where the two probe volumes no longer cross. If the probe volumes do not properly cross, the signal will be distorted and the blue and green sampling volumes will be at different locations.

All measurements presented in this thesis were measured at two different horizontal planes in the test housing where the wall angle is  $0.0^\circ$  and  $18.7^\circ$ . For simplicity, it was assumed here that the effects of the displaced and distorted probe volume were insignificant. However, preliminary calculations indicate that the  $737 \mu\text{m}$  probe volume of the dual component laser system transmitted through the SAE Test Housing with a diffuser wall angle of  $18.7^\circ$  may experience a displacement of as much as  $1000 \mu\text{m}$ . Assuming that the reflected light scatter will be counter displaced, this displacement may not pose major bias error other than a drop in intensities of the reflected light. However in addition to the total probe volume displacement, the two probe volumes may be displaced from each other by as much as  $100 \mu\text{m}$ . Preliminary calculations of the probe volume displacements for  $9.5 \text{ mm}$  ( $0.375 \text{ in.}$ ) and  $6.4 \text{ mm}$  ( $0.25 \text{ in.}$ ) thick Plexiglas with varying housing angles are presented in Appendix E. It is recommended here that these effects be further investigated and that such necessary off/on line corrections be implemented. Note that the velocity measurements presented in this thesis which are used for the filtration efficiency models were all measured downstream of

the diffuser section at a wall angle of  $0.0^\circ$  and do not pose any bias errors due to refraction and incidence beam angle effects.

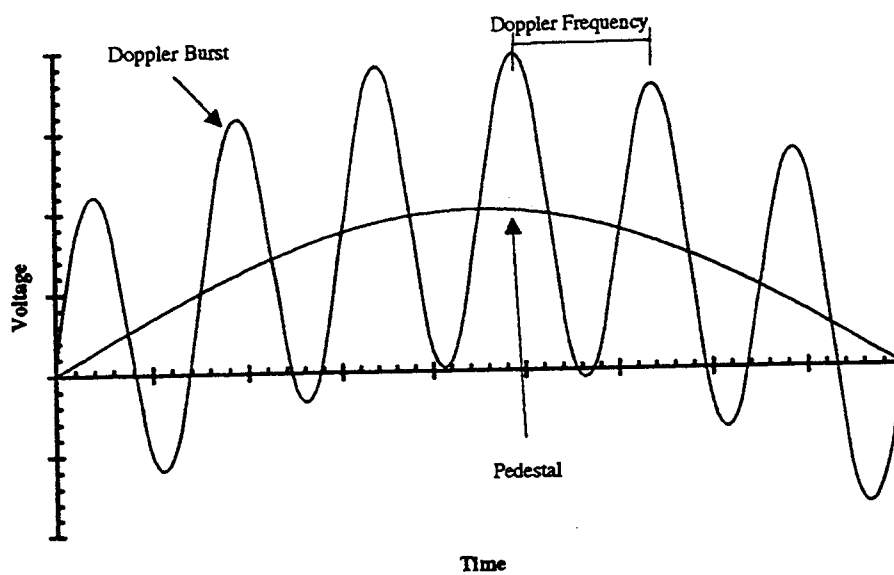


Figure 3.3 An Example of a Raw Doppler Burst Signal (Hiatt, 1994).

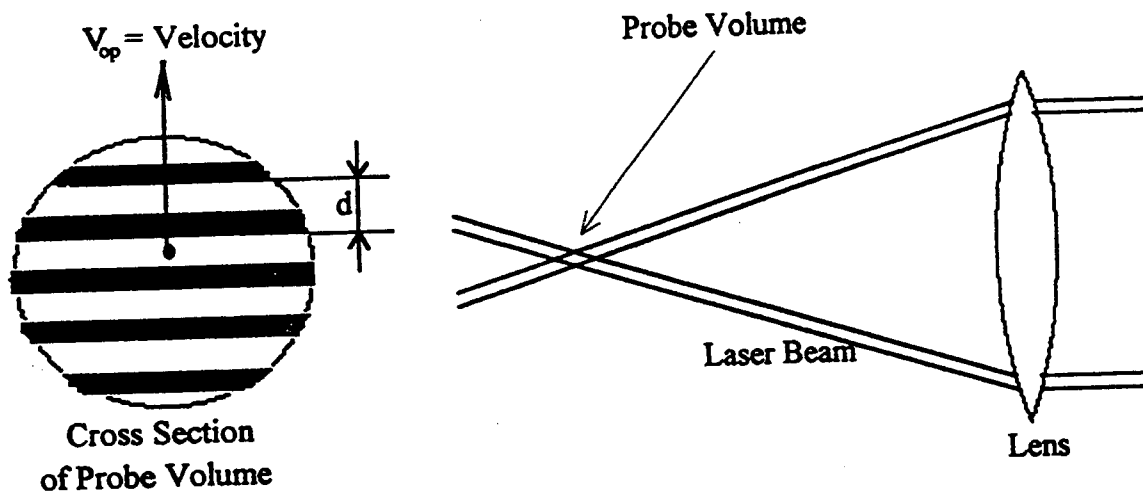


Figure 3.4 Diagram of a Particle Passing Through the Fringe Pattern.

### 3.4 Set-Up and Parameters of Laser Doppler Velocimetry Measurements

The flow stream was seeded with 1  $\mu\text{m}$  (0.966  $\mu\text{m}$ ) diameter polystyrene latex particles produced from a 250 PPM water solution by a 6-Jet Atomizer with the pressure regulator set at 60 psig. The seed particles were introduced to the flow stream through the flow distributor as illustrated in Figure 3.1. In efforts to avoid introducing water droplets and condensation into the flow stream, the flow stream was heated with a fan heater just after leaving the atomizer. The four laser beams of the LDV system were aligned so that measurements were performed in agreement with the sign convention and coordinate system illustrated in Figure 3.5. The axial velocity component is normal to the plane of the filter and is positive downward through the filter. The transverse velocity component is in the direction of the long axis of the filter and is positive towards the exit of the flow leading to the exhaust blower.

The measurements presented in this thesis were conducted in either of the two horizontal planes illustrated in Figure 3.6. Plane I is approximately 12.7 mm (0.5 in.) upstream of the filter pleat peaks and Plane II is approximately 50.8 mm (2.0 in.). Any plane between Plane I and II would be physically impossible for proper beam transmission due to the plexiglas interface and adhesive used to join the diffuser section with the zero angle wall of the test housing. Furthermore, to avoid complex probe volume distortion due to wall angles, all four beams must be entering the housing at the same wall angle. Note that at all measurements were downstream of any sphere positioned within the test

housing. The measurement grid was spaced at increments of 12.7 mm (0.5 in.) across the short axis of the filter and 19.0 mm (0.75 in.) across the long axis of the filter, as illustrated in Figure 3.7. Measurements were only performed in one half of the filter region corresponding to positive Y-coordinates. This allowed for measurements to be as close to the filter as possible. The restriction is due to the lowest of the four beams needing to clear the filter edge. At Plane II, measurements can be conducted across the full filter region. Nonetheless, for simplicity and convenience, all measurements conducted were limited to the positive X-coordinates.

The non-uniform test housing flow required the DSA processing parameters to be adjusted as the sampling probe volume was transversed to different locations in the flow field. The different mean velocities, flow directions, and seed particle concentrations all contributed to the need to adjust the DSA parameters accordingly. The reader is referred to the Aerometrics Applications User's Manual (Aerometrics, 1992) for a detailed description of the parameters and settings. These variations resulted in data rates and validation rates that were different in different regions of the flow field.

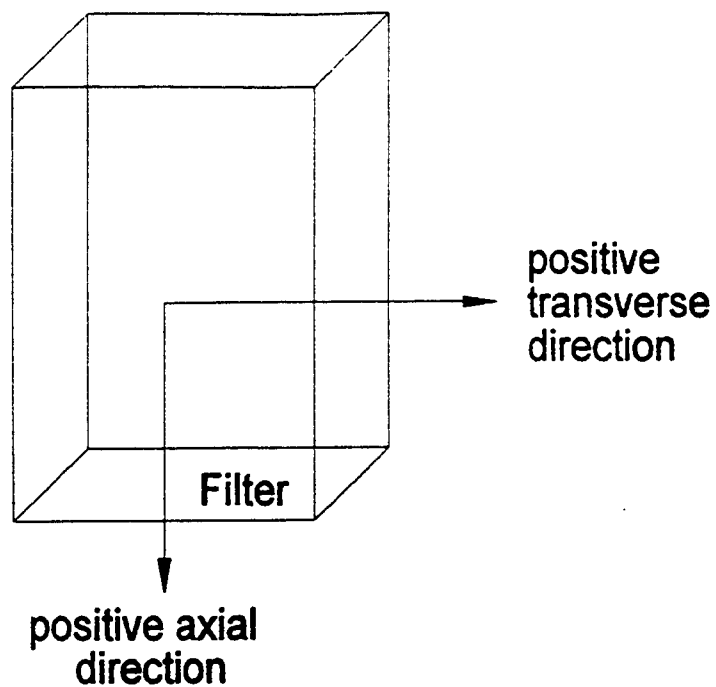
In efforts to provide consistent velocity measurements across the flow field, all measurements presented were obtained from the average of 500 validated samples with coincidence on. In working with Newman (1994), we determined that for PSL particles of 100 PPM to 300 PPM a total of 500 samples per data point would be the least number of points that could be used and still obtain a reliable run with an uncertainty of  $\pm 2\%$  of the average flow velocity. At a 500 sample validation, data within the SAE test housing

was obtained within 30 seconds to 300 seconds, actual DSA run time per data point. Newman achieved data just under 200 seconds with a 1000 sample validation for a reliable run within  $\pm 1\%$  of the average flow velocity. The difference can be attributed to the much more uniform flow through the prototype test housing used by Newman. In the central region of the SAE test housing, the number of validations is easily achieved within 60 seconds. In the slower, more lightly seeded flow away from the centerline, a much longer total time is required to obtain the 500 samples. No corrections were applied here for the velocity biases that may enter into the LDV measurements within the varied flow regions.

Bias errors include velocity bias, gradient bias, fringe bias, and filter bias errors. Velocity bias simply means that regions of faster velocity fluid will carry more fluid ( $Q = VA$ ) through the probe volume than regions of slower velocity fluid. Assuming the fluid is uniformly seeded, the regions of faster velocity will be sampled more than the regions of slower velocity in a given time interval resulting in higher mean velocity readings. Velocity bias is corrected by using residence time weighting. It is recommended here that such velocity bias corrections be investigated and implemented if velocity bias errors are determined to be large. Gradient bias occurs when there is a velocity gradient across the probe volume. It is assumed here that no velocity gradient is present within the small region of the probe volume. Thus, no corrections were applied for gradient biases. Fringe bias is related to the fact that the probability of a particle generating a measurable signal depends on the direction of the particle relative to the laser beams. This bias was solved by using a frequency shift system which creates a moving fringe pattern eliminating



Velocity  
Sign  
Convention



Positioning  
Coordinate  
System

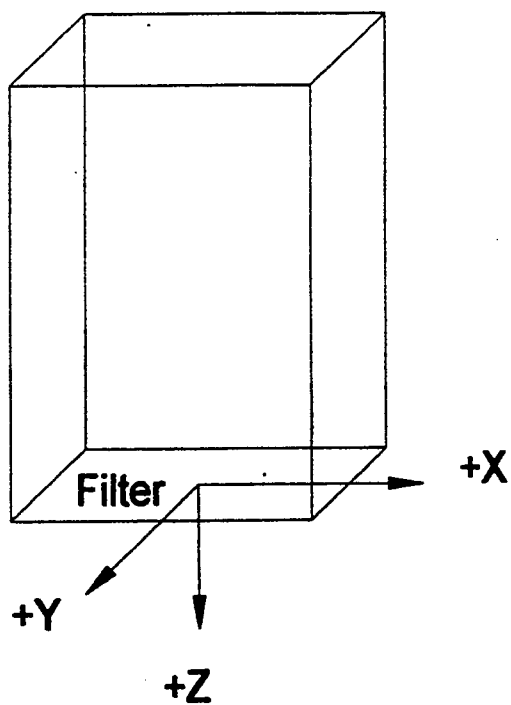


Figure 3.5 Sign Convention and Coordinate System for Velocity Measurements

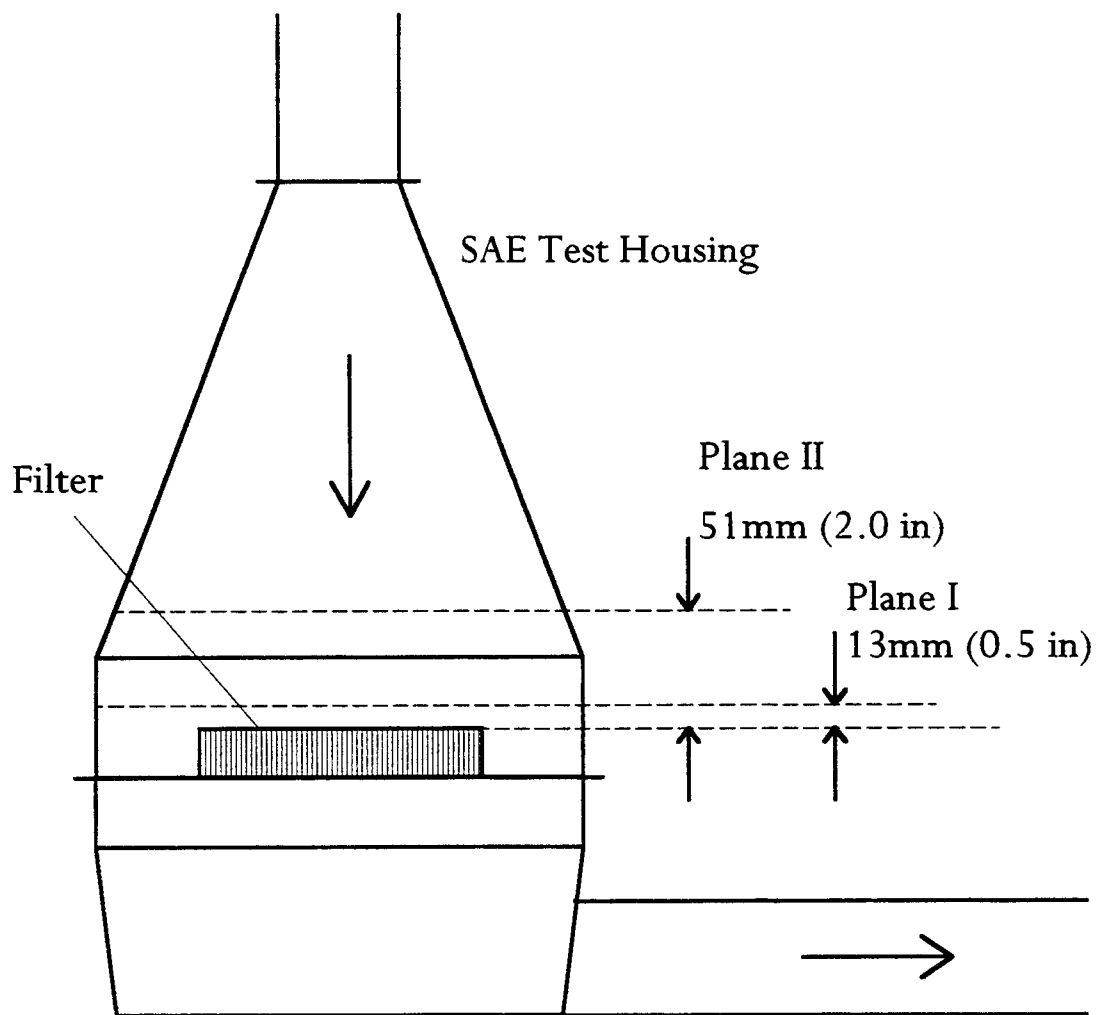


Figure 3.6 Velocity Measurement Planes

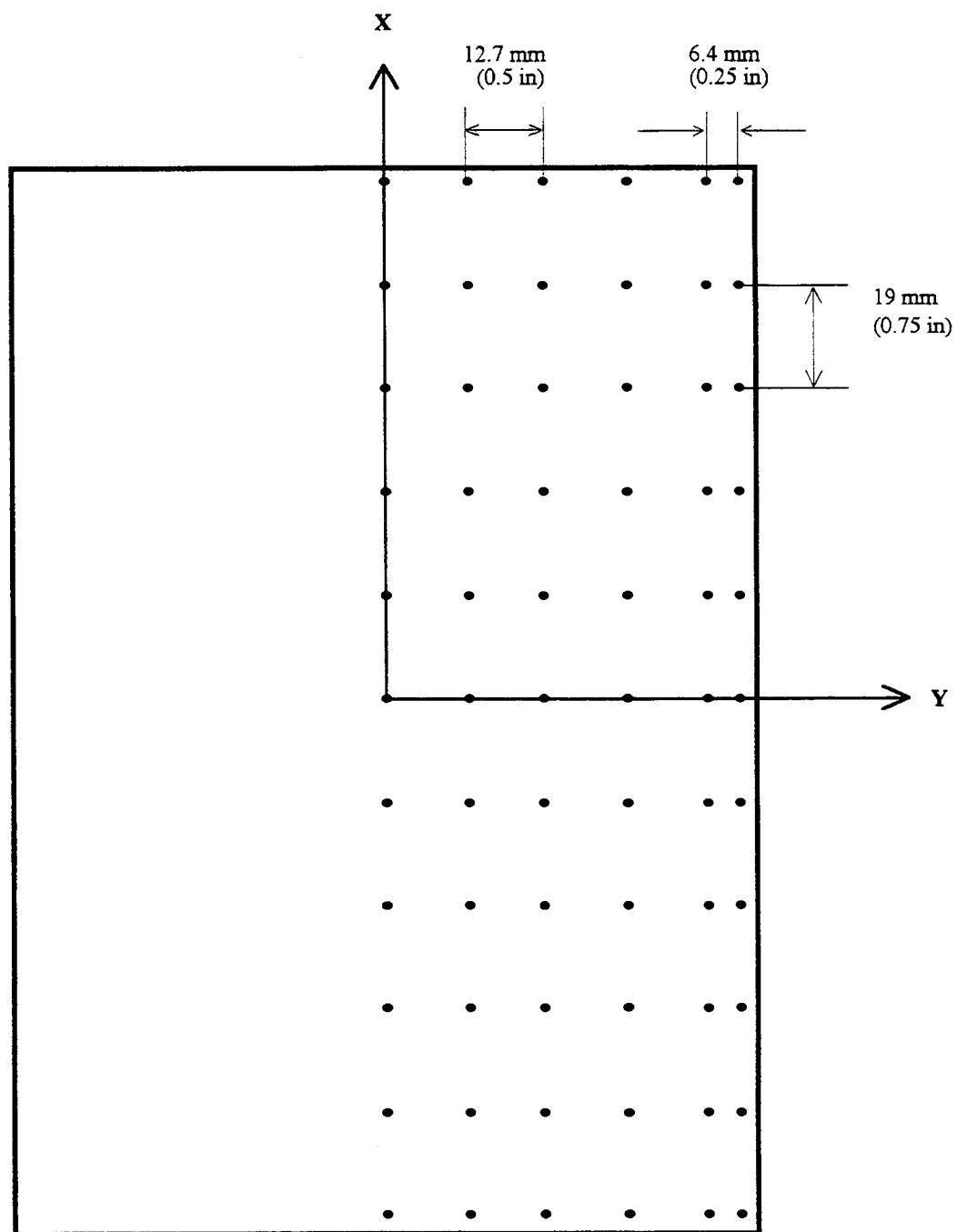


Figure 3.7 Velocity Measurement Grid

directional ambiguity from velocity measurements of reversing flows. Filter bias is related to the filtering settings which filter out some velocity measurements. Filters were set at a level to ensure that only low and high noise was filtered. Furthermore, histograms of velocity measurements were viewed to ensure that a full approximate Gaussian distribution was present indicating that no flow velocities were being filtered.

### 3.5 Flow Visualizations

Flow visualization techniques are commonly used to provide a qualitative insight of a flow field. These techniques may provide a quick and easy overall perspective of the flow field. The insight gained from the flow visualizations, may justify the need for further investigations and the need for quantitative measurements of the flow field, LDV measurements. Flow visualizations help complement LDV measurements and aid in the understanding of a flow field. It has been determined from past work that some of the conventional flow visualization techniques do not work well for the separated and highly turbulent flow within the SAE test housing (Sabnis, 1993). Water droplet and intermittent smoke visualizations have been found to be an effective method of qualitatively analyzing the flow field within a filter test housing (Newman, 1994; Sabnis, 1993). Intermittent smoke flow visualizations using laser sheet lighting were conducted and are presented within this thesis. The smoke generator described in Appendix F was found to be an

effective system for smoke flow visualizations using axial and transverse laser sheets. Smoke generating procedures are outlined and provided in a step process in Appendix F. All flow visualizations were captured on still photography and video tape.

With the laser power controller set at a range of 0.8 Watts to over 2.0 Watts, a sheet of laser light was produced by projecting a beam of the laser through a cylindrical lens. The lens creates a sheet of laser light that fans out from the lens in a plane of Gaussian distributed intensities. The laser sheet was positioned horizontally and vertically through the test housing. A two dimensional plane or "slice" of the flow field was visible for qualitative analysis.

### 3.6 Equipment Listing

PSL particles: Polystyrene Latex, PSL, Microspheres of 0.966  $\mu\text{m}$  in diameter were used as seeding particles for the LDV system. The uniform latex microspheres were purchased from Duke Scientific Corp. The particles are packaged in a 10% solid to water solution. To obtain a 250 PPM solution, 2.5 cc of the 10% solution was mixed with 1000 ml of distilled water. For best results, care should be taken to ensure that the water droplets evaporate before reaching the test housing. For velocity measurements within the SAE test housing, PSL particles were found to be more reliable seeding particles than water droplets (Newman, 1994).

Atomizer: A TSI Incorporated Model 9306 6-Jet Atomizer was used to generate the PSL aerosol. The atomizer was operated using all six jets at a regulated air pressure of 60 psig.

Plexiglas SAE Universal Air Filter Test Housing: The original transparent housing constructed by Sabnis (1993) was used. In efforts to achieve a smoother clean surface for LDV measurements the original housing was altered by replacing one of the long axis vertical walls with a 6.4 mm (0.25 inch) thick glass. Sabnis constructed the housing as specified in the SAE J726 Test Code. A detailed drawing of the housing specifications is provided in Figure 1.2. The housing can house any size panel air filter as specified in SAE J1141 provided that the aluminum support is sized accordingly. For easy mounting, the flange between the entrance tube and the housing and the flange between the top and bottom portion of the housing are each secured using four easy release vise-grip clamps. Consistent alignments were ensured using push pins through the flanges. All other joints are permanently glued and are periodically checked for leaks using soapy water. The inlet plexiglas pipe has a diameter of 88.9 mm (3.5 in.) and is 889 mm (35 in.) in length. For test purposes, the housing is mounted upside down, as compared to the SAE J726 Test Code.

Filter Specimen: Purolator AF3192 (recently replaced by Purolator A13192) panel air filters were supplied by Purolator Products Inc. for all velocity measurements presented in this thesis. The reader is referred to Appendix A for a complete

listing of the AF3192 filter specifications. These filters are made from a resin impregnated cellulose fiber paper mat that is first embossed and scored. An adhesive is then applied and the paper is folded, creating the pleats. The pleats are counted, cut, sealed at the ends, and mounted to a rubber holder or gasket. The filter is then heated to cure the resin and secure the strength of the pleats. A screen is then mounted on the back of the filter for additional support. This screen helps the filter maintain its structure integrity in the event of engine backfire and moisture.

Centrifugal Multistage Exhauster/Blower: In the past, a 1.5 hp centrifugal blower capable of producing a maximum flow rate of 225 scfm was used for velocity measurements of clean filters. Due to the joint efforts of me and my colleagues, separate clean filter tests and dirty filter tests were conducted periodically. The testing of dirty filters requires a much stronger blower to achieve a flow rate of 125 scfm through the filter due to the increase in pressure drop through the filter (Liu et al, 1995). Consequently, it was convenient to run all experiments with the use of a larger blower, the multistage centrifugal exhauster. The multistage centrifugal exhauster is part of the Automotive Air Filter Test Stand. The multistage centrifugal exhauster is powered by a 40 hp induction motor and can achieve flow rates ranging from 25 scfm to 1000 scfm. All flow rates are easily measured with corrections for operating temperatures and barometric pressure.

Automotive Air Filter Test Stand: The Automotive Air Filter Test Stand was designed

and built by Facet Enterprises, Inc. in 1976 and is comprised of a multistage centrifugal exhauster, laminar flow element, high efficiency absolute filter, elevated test stand area, and a control panel. This test stand was designed and built for dust loading and testing of dirty automotive air filters, both round and panel type. This complete system is on an extended loan from Purolator Products Inc.

Mass Flow Rate Sensor: In the past, a TSI Incorporated Series 2010 Mass Flowmeter was used to measure the flow rate through the test housing. On occasion, this flowmeter was used to verify the settings and readings of the Automotive Air filter Test Stand. The flow sensor has a maximum measurable flow rate of 500 SCFM and is easily calibrated with a 76 mm ASME flow nozzle.

Laser: A Coherent 4 watt laser, Innova 70 Model, consisting of an argon ion plasma tube powered by an Innova 70-A power supply was used. During actual testing, the intensity of the beam ranged from 0.2 Watts to 1.2 Watts and was controlled by a remote controller. Note that the 515 nm green beams are not visible below a power setting of 0.4 Watts.

Bragg Cell & Driver: An IntraAction Bragg cell driver model ME-40H controlled the Bragg cell mounted inside the fiber drive. The light beam from the plasma tube was directed by steering mirrors into the fiber drive and through the Bragg cell. The 40 MHz Bragg cell splits the beam into several beams of different multiple shifts and one of zero shift. The +40MHz shifted beam and the non-shifted beam are used downstream of the Bragg cell.



Fiber Drive: An Aerometrics Model FBD.1240 fiber drive was used and consists of the Bragg cell, laser optics, beam splitters, fiber couplers, and fiber cables. The beam splitting prisms split the unshifted and shifted beams into two separate beams of different wavelengths, for a total of four beams. Resulting in one unshifted and one shifted beam for each color. Mirrors direct each of the beams into the fiber couplers which align and focus the beams onto the fiber cables leading to the transceiver. The fiber drive allows for easy and consistent alignment, as long as the laser beam is aligned properly into the Bragg cell, one merely needs to adjust the fiber couplers for maximum intensity out through the transceiver.

Transceiver: An Aerometrics model XRV.1212 transceiver receives the four beams through fiber optic cables. The beams are transmitted through a 500 mm lens producing a probe volume of 737  $\mu\text{m}$  in length and 66  $\mu\text{m}$  in diameter. The transceiver collects the back-scattered light reflected from seeding particles passing through the probe volume. The collected light is then transmitted through a fifth fiber optic cable to the photodetector unit which distinguishes the blue and green light scatter.

Photodetector Unit: The Aerometrics photodetector unit model ROM.2200.L contains two photomultipliers, one for each wavelength light, blue and green. The photomultipliers convert the optical light scatter signal into an analog voltage signal and pass it on to the DSA.

Doppler Signal Analyzer, DSA: The raw Doppler burst signal is analyzed by the

Aerometrics Doppler Signal Analyzer model DSA.3220, Version 4.18s DSA D, Copyright 1989, 1991, 1992, with revisions updated April 1993 (Aerometrics, 1992 and 1993). The signal is first high pass filtered to remove the low frequency pedestal from the Doppler burst signal then low pass filtered to remove high frequency noise. A peak detector in conjunction with a burst detector locates the center of the signal. Programmable mixers are used to reduce the signal frequency before it is presented to the Analog to Digital Converter, ADC. The ADC converts the complex, filtered, sampled signal to a 1 bit digital representation of the input signal. A Digital Signal Processor, DSP, is used in the computer to perform Discrete Fourier Transforms, DFT, using the Fast Fourier Transform, FFT, algorithm. The DSP is programmed to compute the Fourier transforms at a high rate and pass the results to the system software for statistical analysis and presentation of the velocity information of the particles in histogram form. Validation tests are performed on individual spectra, rejecting low quality noisy data.

Personal Computer I: An Intel 486 DX/2 compatible personal computer running at 66 MHz was used to control the entire DSA system. Aerometrics DSA software performs statistical analysis of processed data from the DSA hardware. For ease in managing and organizing the DSA processed data, I developed a simple program to select and arrange the off line DSA data series output. A source code listing of this program is provided in Appendix D.

Personal Computer II: A Gateway 2000 486 compatible personal computer running at 33 MHz was used to control the Automated Traverse Table. Two horizontal stepping motors are controlled through a computer program developed by Newman. The program is written so that a user can move the traverse in either X or Y axis direction by steps or to an absolute location.

Automated Traverse Table: The transceiver is mounted on a recently constructed vertical axis translation stage which is mounted on a Daedal two component traverse table system. The vertical axis translation stage was controlled manually. Two component translation in the horizontal plane was provided by stepping motors under computer control.

Smoke Generator: A smoke generator was used to aid in the flow visualizations. Refer to Appendix F Smoke Generator.

## CHAPTER IV

### RESULTS AND DISCUSSION OF FLOW VISUALIZATIONS AND LASER DOPPLER VELOCIMETRY MEASUREMENTS

#### 4.1 Flow Visualizations

Flow visualization techniques provide a quick and easy overall perspective of the flow field. The qualitative insight gained from the flow visualizations may justify the need for quantitative measurements of the flow field, such as laser Doppler velocimetry measurements. Water and intermittent smoke visualizations have been found to be effective methods of qualitatively analyzing the flow field within a filter test housing. Intermittent smoke flow visualizations using laser lighting were conducted and are presented within this section. The smoke generator described in Appendix F was found to be an effective system for smoke flow visualizations using axial and transverse laser sheets. All flow visualizations were captured on still photography film and video tape.

A vertical or axial laser sheet with water droplet flow visualization is shown in Figure 4.1. The photograph reveals the separated and recirculating nature of the flow within the SAE test housing. The central part of the housing is densely filled with water droplets indicating more particles in the central region. The curved streaks toward the corners of the laser sheet indicate the recirculating regions. The straight

streaks within the central region indicate a high concentration of particles within the central region with jet like flow.

Figure 4.2 illustrates an intermittent smoke flow visualization of the SAE test housing with a 76.2 mm diameter sphere positioned 159 mm from the housing inlet. Note that the additional supports used to mount the sphere were added due to the flow induced vibrations of the sphere observed in earlier experiments. This photograph reveals an improved inlet distribution with a smaller region of separation along the walls of the housing. Due to the redistribution of flow by the sphere, the central flow region appears to be wider, reducing the region of separation near the walls.

Similar flow visualizations were extensively conducted for various sized spheres positioned at the housing inlet to just upstream of the filter specimen. Actual balls/spheres used include Ping-Pong balls, golf balls, racket balls, and wooden spheres of diameters up to 76.2 mm (3 in.). Flow visualizations with the spheres positioned at the inlet indicated that the inlet flow was re-distributed away from the central inlet region. However, due to the high inlet velocities at a flowrate of 125 cfm, the inlet flow downstream of the spheres is re-channelled back to the central region. At this high flowrate the spheres' wake region is short. Consequently, the larger sized spheres positioned downstream of the inlet appeared to be most effective. Based on these findings, laser Doppler velocimetry measurements were conducted on selective sphere sizes at various positions downstream of the housing inlet.



Figure 4.1 Axial Laser Sheet Water Droplet Flow Visualization within the SAE Test Housing (Sabnis, 1993).

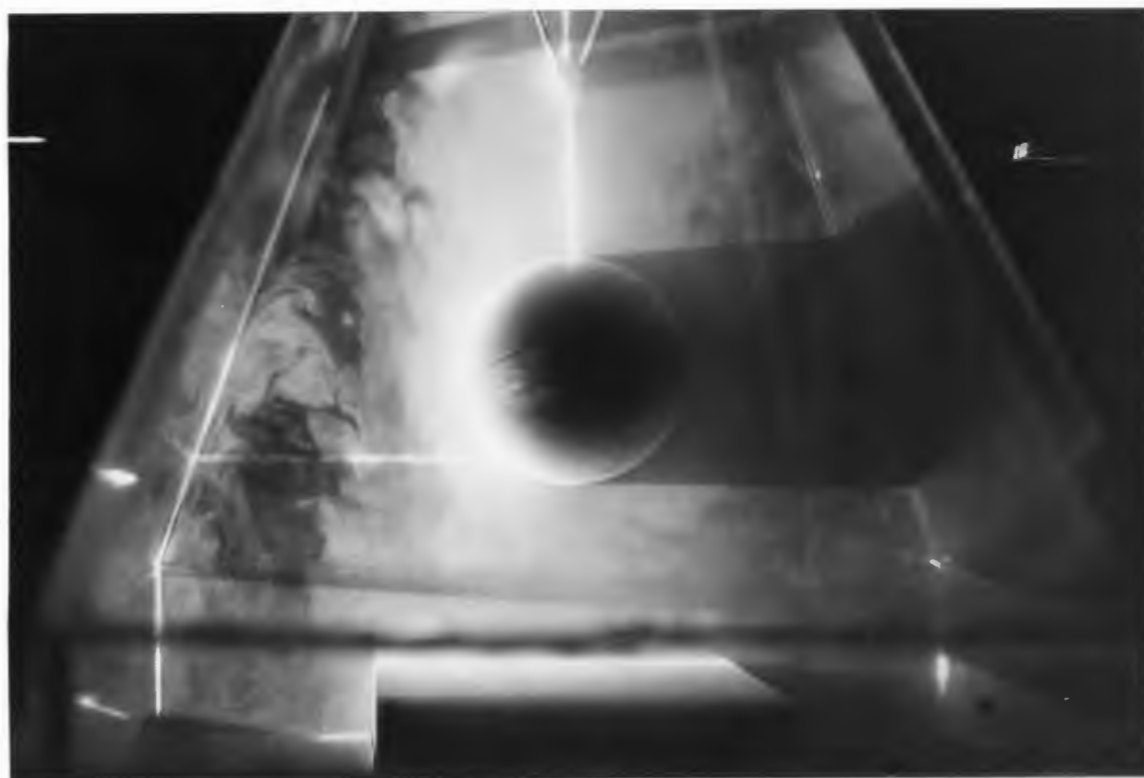


Figure 4.2 Axial Laser Sheet Intermittent Smoke Flow Visualization within the SAE Test Housing with a 76.2 mm Dia Sphere Positioned 159 mm from the Housing Inlet.

## 4.2 Improvement of Flow Distribution

### 4.2.1 *Spheres Positioned Near the Housing Inlet*

In efforts to achieve a more uniform flow, attention was centered on redesigning and/or recommending modifications to the standard SAE test housing. One alternative is to obstruct the inlet flow in such a manner as to provide a more uniformly distributed flow pattern. Laser Doppler velocimetry measurements were conducted on different sized spheres positioned at or near the housing inlet. Figure 4.3 is a plot of the axial velocities at the center line measured 13 mm upstream of the filter, Plane I. All axial velocity measurements are positive going into the filter and span across the entire filter length, the plane of  $Y = 0.0$  mm. Note that axial velocities are highest at the central region and lowest near the edges. An ideal uniform flow would provide a constant upstream velocity throughout the filter specimen.

Referring to Figure 4.3, the larger sized spheres positioned near the inlet reveal a lower center velocity, at  $X = 0.0$  mm. Note that the velocities near the edges of the filter are increased. As observed from the flow visualizations conducted, due to the high inlet velocities, the spheres' wake region is short and the flow downstream of the spheres is re-channelled back to the central region. Furthermore, the walls of the housing seem to delay separation along the sphere's surface, allowing the flow about the sphere to stay attached longer, as compared to a sphere not confined within a diffuser housing. Due to this short wake region, a more uniformly distributed flow



pattern upstream of the filter is best achieved by obstructing the flow downstream of the inlet, or rather, by obstructing the flow upstream of the filter specimen. Improvement of flow distribution upstream of the filter is presented in the following sub-section.

The transverse velocity measurements simultaneously measured with the axial velocities provided in Figure 4.3 are plotted in Figure 4.4. Transverse velocity measurements on the left side of the filter tend to be negative while those on the right side of the filter tend to be positive. This shows that as the flow nears the filter it fans out, like an impinging jet. The SAE test housing exit leading to the downstream induction blower is positioned to the left of the filter resulting in slightly higher positive velocities on the left side of the filter. Obstructing the inlet flow still provides a similar and consistent flow pattern of transverse velocities indicating an impinging jet like pattern near the filter.

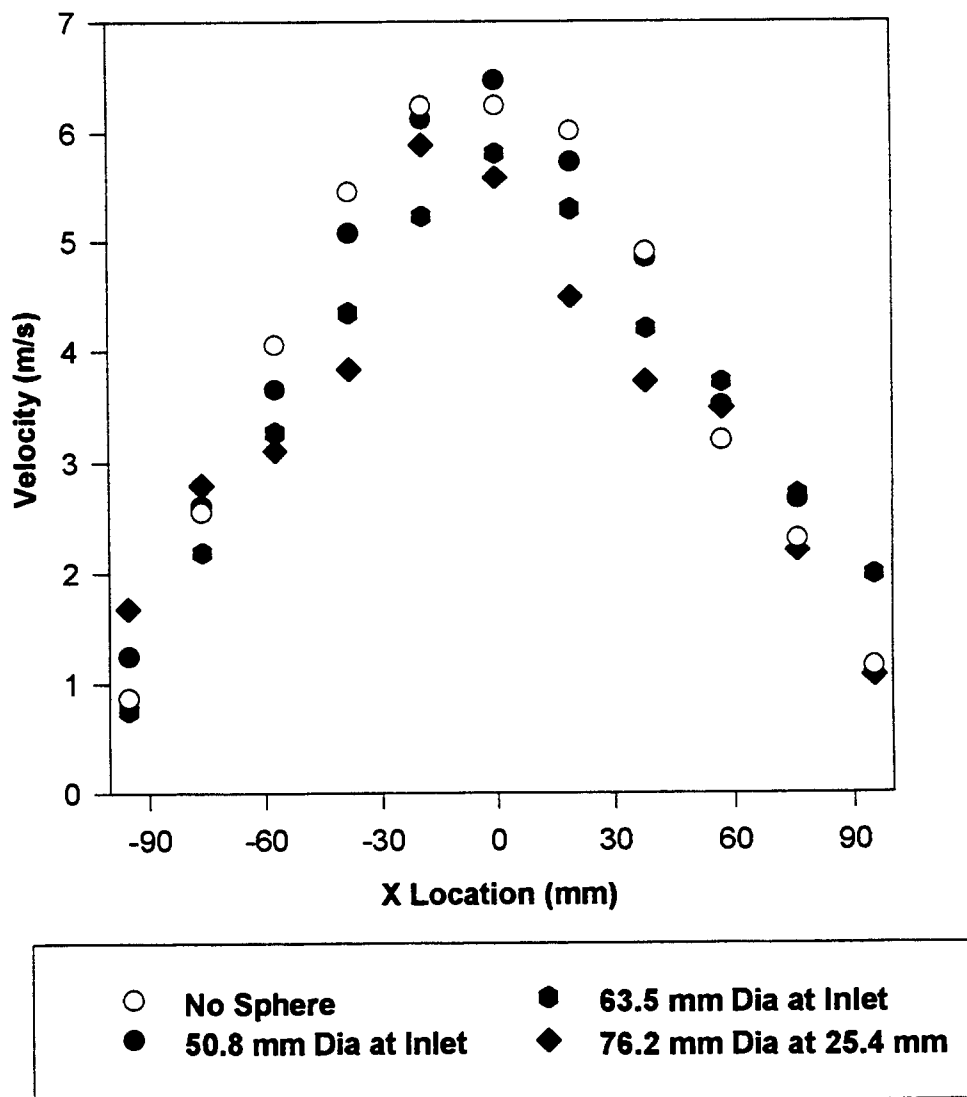


Figure 4.3 Center Line Axial Velocity Profiles Measured at 13 mm Upstream of the Filter, Plane I, with 50.8 to 76.2 mm Dia Spheres Positioned Near the Inlet.

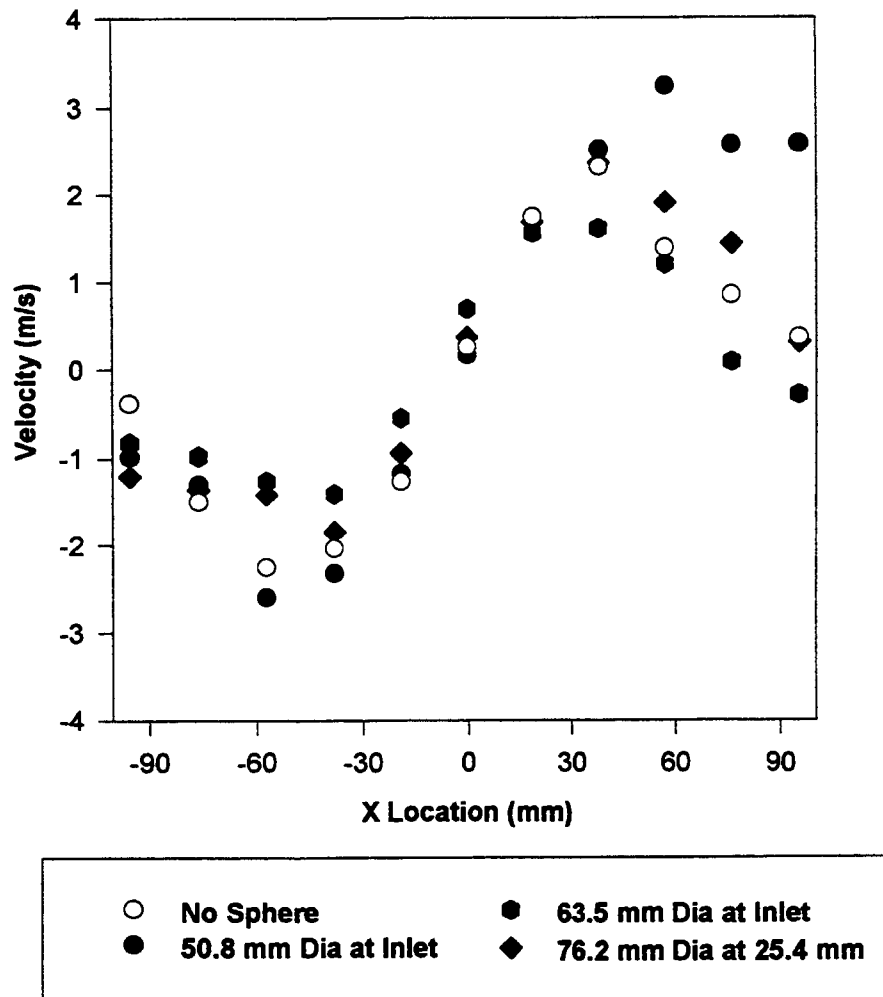


Figure 4.4 Center Line Transverse Velocity Profiles Measured at 13 mm Upstream of the Filter, Plane I, with 50.8 to 76.2 mm Dia Spheres Positioned Near the Inlet.

#### 4.2.1 Spheres Positioned Upstream of the Filter Specimen

Based on the flow visualizations and LDV measurements presented in the previous sub-section, it was determined that the flow pattern upstream of the filter specimen may be best improved by obstructing the flow further downstream of the housing inlet. Center line axial velocities of a 76.2 mm (3 in.) diameter sphere positioned 197 mm (7.75 in.), 171.5 mm (6.75 in.), and 159 mm (6.25 in.) from the housing inlet are presented in Figure 4.5. The distances between the filter and sphere range from 32 mm (1.25 in.) to 70 mm (2.75 in.), respectively. All velocity measurements were conducted at 13 mm (0.5 in.) upstream of the filter, Plane I. All three sphere positions result in lower center velocities, at  $X = 0.0$  mm. The sphere positioned at 197 mm results in the lowest center velocity of 0.747 m/s. The center line velocity measurements are clearly within the wake region of the spheres resulting in lower axial velocities approaching the central region of the filter. Velocities near the edges of the filter slightly increase as the velocities in the central region decrease, due to continuity. (The fact that the axial velocities at the far left side of the filter only slightly increase merely suggests a slight misalignment.) Note that the peaks of the velocity profiles occur at approximately one half of the sphere diameter from the center of the filter, at  $X = \pm 38$  mm.

The transverse velocity measurements are presented in Figure 4.6. Unlike Figure 4.4, these transverse velocities are much more scattered. These transverse component measurements reveal a complex flow field with variations in transverse flow direction. This may be attributed to the increase in turbulence intensity in the near wake region of the spheres. However, although the transverse flow is somewhat complex, the general trend is still that the flow fans out like an impinging jet.

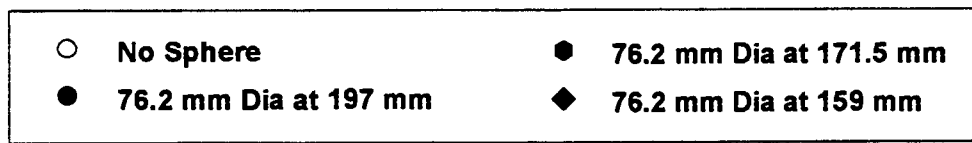
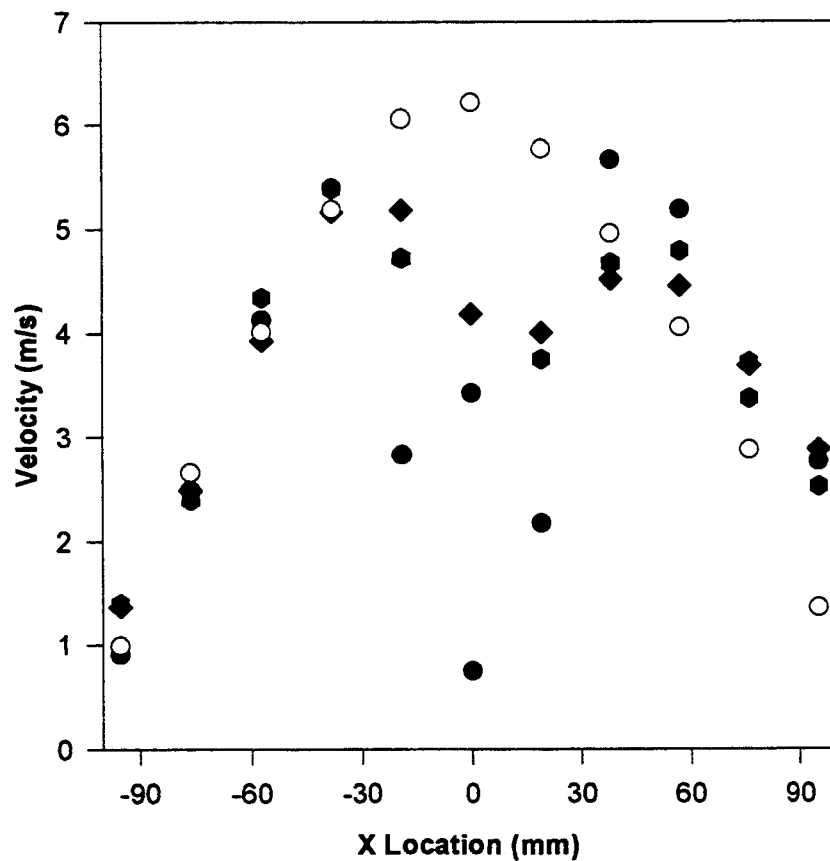


Figure 4.5 Center Line Axial Velocities Measured at 13 mm Upstream of the Filter, Plane I, with a 76.2 mm Dia Sphere Positioned at the Specified Distances from the Housing Inlet.

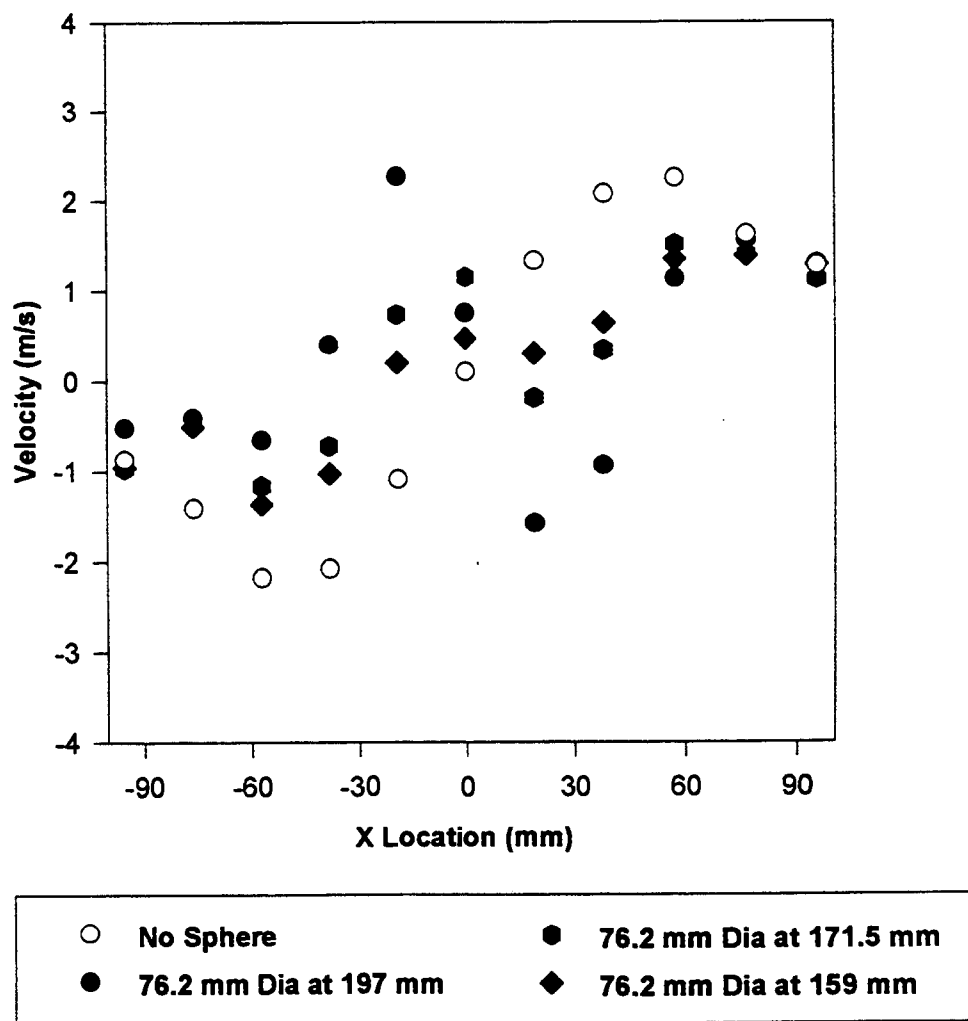


Figure 4.6 Center Line Transverse Velocities Measured at 13 mm Upstream of the Filter, Plane I, with 76.2 mm Dia Sphere Positioned at the Specified Distances from the Housing Inlet.

### 4.3 Three-Dimensional Axial Velocity Profiles

In all of the data presented in this chapter, the edges of the X and Y axes represent the edges of the filter. Data taken in this study represents only the front half of the filter,  $Y \geq 0.0$  mm, as illustrated in Figure 3.7. The collected data is represented in three-dimensional form. Figure 4.7 is a three-dimensional axial velocity plot of the velocities 13 mm upstream of a filter within the SAE test housing. The data was nondimensionalized by dividing each data point by  $U_{mean} = 2.567$  m/s. This mean velocity value represents the calculated average velocity through the filter area at a flow rate of 125 cfm;  $U_{mean} = Q/A$ . All axial velocities measured above the filter specimen are positive with the strongest flow being concentrated in the central region. The surface representing the non-dimensionalized axial velocities is shaped like a dome indicating non-dimensional velocities greater than 2.0 in the central region and gradually reducing to non-dimensional velocities below 1.0 towards the edges of the filter. An ideally uniform flow pattern would reveal a flat and straight velocity profile across the entire region above the filter area. However, not necessarily of unity, due to inconsistencies of actual operating flow rates. Inconsistencies of actual operating flow rates are primarily attributed to undetected leaks. It was assumed here that (1) all flow going through the filter goes through the measurement grid region and (2) recirculating flow along the sides of the filter is negligible. A maximum and minimum non-dimensionalized velocity of 2.57 (6.6 m/s) and 0.12 (0.32 m/s) were measured at the central region and at the front right edge of the filter, respectively.

Figure 4.8 is a three-dimensional axial velocity plot of the velocities measured 13 mm upstream of a filter with a 76.2 mm sphere positioned 159 mm downstream from the housing inlet. The axial flow in the central region is strongly reduced. A

maximum and minimum non-dimensionalized velocity of 2.22 (5.69 m/s) and 0.19 (0.48 m/s) was measured at the left edge of the central region and at the front right edge of the filter. The decrease in velocities within the central region causes the velocities near the edges of the filter to increase, due to continuity. Furthermore, also due to the decrease in flow within the central region, the maximum velocities occur at approximately one half the sphere diameter. The non-dimensionalized velocity at the center of the filter,  $X = 0.0$  and  $Y = 0.0$ , is 1.59 (4.08 m/s). The profile of the center line axial velocities is illustrated in Figure 4.5.

Figure 4.9 is a three-dimensional axial velocity plot of the flow velocities measured 51 mm, Plane II, upstream of a filter with the same 76.2 mm sphere positioned 159 mm downstream from the housing inlet, as in Figure 4.8. At Plane II, closer to the sphere, the velocities tend to fluctuate more. As in Figure 4.8, the axial flow in the central region is strongly reduced. A maximum and minimum non-dimensionalized velocity of 2.51 (6.4 m/s) and 0.09 (0.22 m/s) were measured at the right edge of the central region and at the front right edge of the filter. Note that at Plane II, the velocities above the edges of the filter tend to be lower. Actual measurements at Plane II with  $X$  and  $Y$  locations not above the filter area (data not shown) reveal low values of negative and positive velocities indicating a recirculation region.

Figure 4.10 is a three-dimensional axial velocity plot of the flow velocities measured 13 mm, Plane I, upstream of a filter with the same 76.2 mm sphere positioned 197 mm downstream from the housing inlet. As in Figures 4.8 and 4.9, the axial flow in the central region is strongly reduced. The non-dimensionalized velocity at the center of the filter is 0.36 (0.92 m/s) as compared to 1.59 (4.08 m/s) of Figure 4.8 with the sphere positioned at 159 mm. The profile of the center line axial



velocities is illustrated in Figure 4.5. Maximum and minimum non-dimensionalized velocities of 2.37 (6.08 m/s) and 0.27 (0.68 m/s) were measured at the left edge of the central region and at the front right edge of the filter, respectively. Note the close resemblance of Figures 4.9 and 4.10. Both sets of data for the two figures are at two different planes. However, both sets of data were taken at the same distance downstream of the sphere, 19 mm.

By obstructing the flow upstream of the filter with a 76.2 mm diameter sphere, the central region velocities are lowered and the edge velocities are slightly increased. Furthermore, the maximum velocities measured are lower than the maximum velocity obtained without any obstruction of flow. The difference in the maximum velocities is as much as 16%, at 13 mm upstream of the filter. Although a truly uniform flow pattern is not achieved, moderate flow improvement is apparent: the central region flow upstream of the filter is reduced and lower variations in the axial velocities are achieved. To better illustrate the improvement in flow uniformity, the data presented in Figures 4.7 to 4.10 was used to generate the non-dimensionalized flow rates of eight equally sized regions above the front half of the filter. These flow rate comparisons are presented in the following section.

Low axial velocities tend to occur near the edges of the filter. Furthermore, it may be noted that the lowest of these velocities tend to be in the front right edges of the filter. This occurrence may be attributed to an undetected leak or to the exit downstream of the filter located on the right side, as illustrated in Figure 3.6. The location of the exit tends to increase the positive transverse velocities on the right side and, as a result, the axial velocities are lower on the right side. Consequently, axial velocities tend to be lower in the front right corner of the filter. Three-dimensional transverse velocities are presented in Section 4.5.

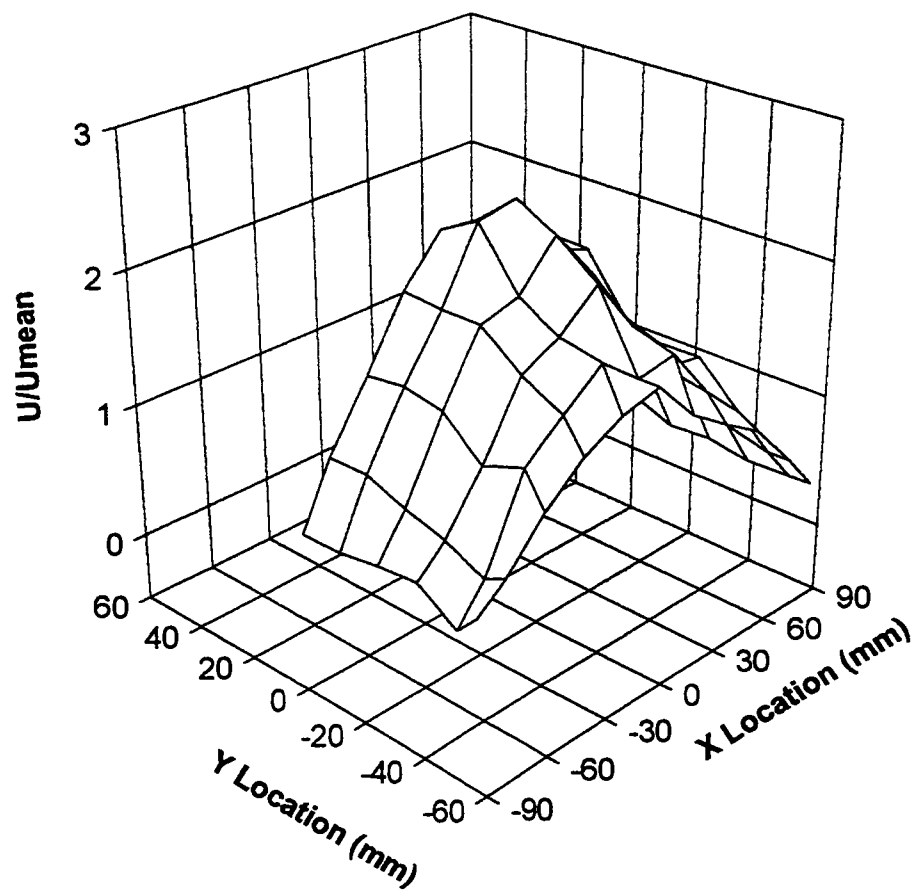


Figure 4.7 Non-Dimensional Axial Velocities in the Standard SAE Test Housing Measured at 13 mm Upstream of the Filter, Plane I.

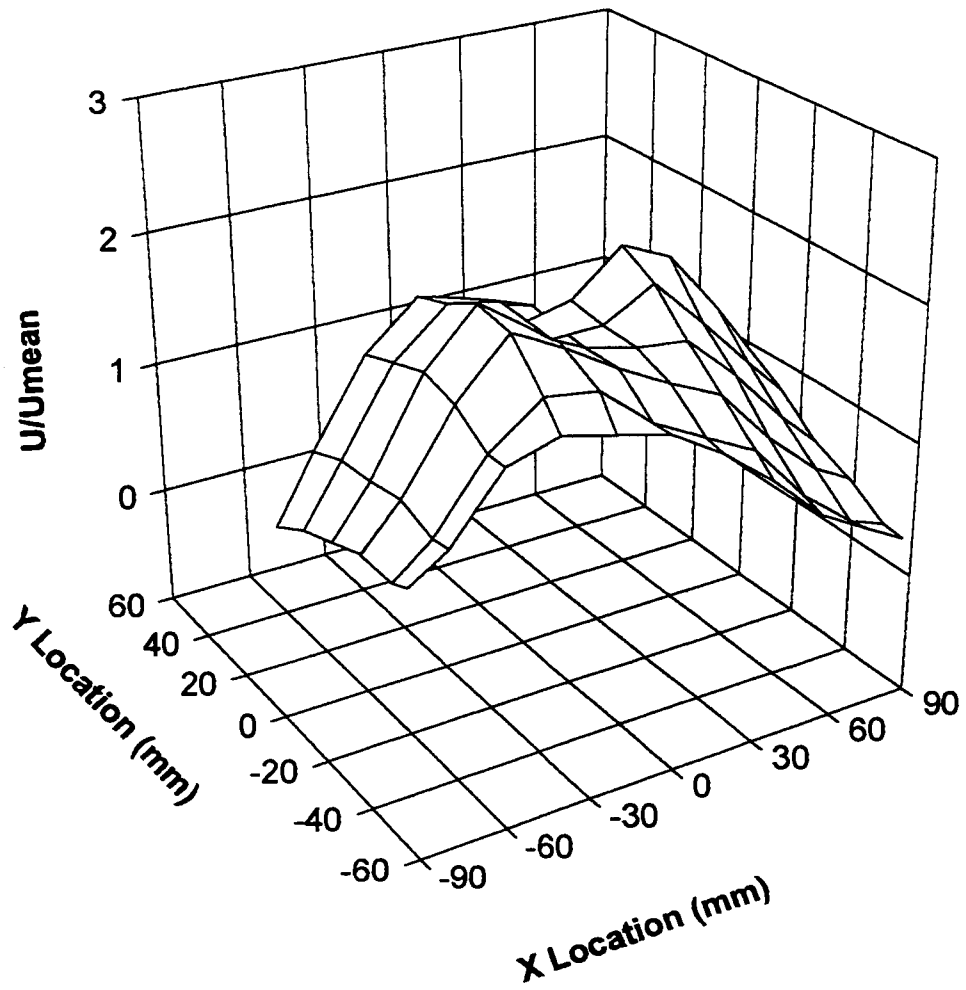


Figure 4.8 Non-Dimensional Axial Velocities in the Test Housing Measured at 13 mm Upstream of the Filter, Plane I, with a 76.2 mm Dia Sphere Positioned at 159 mm Downstream from Housing Inlet.

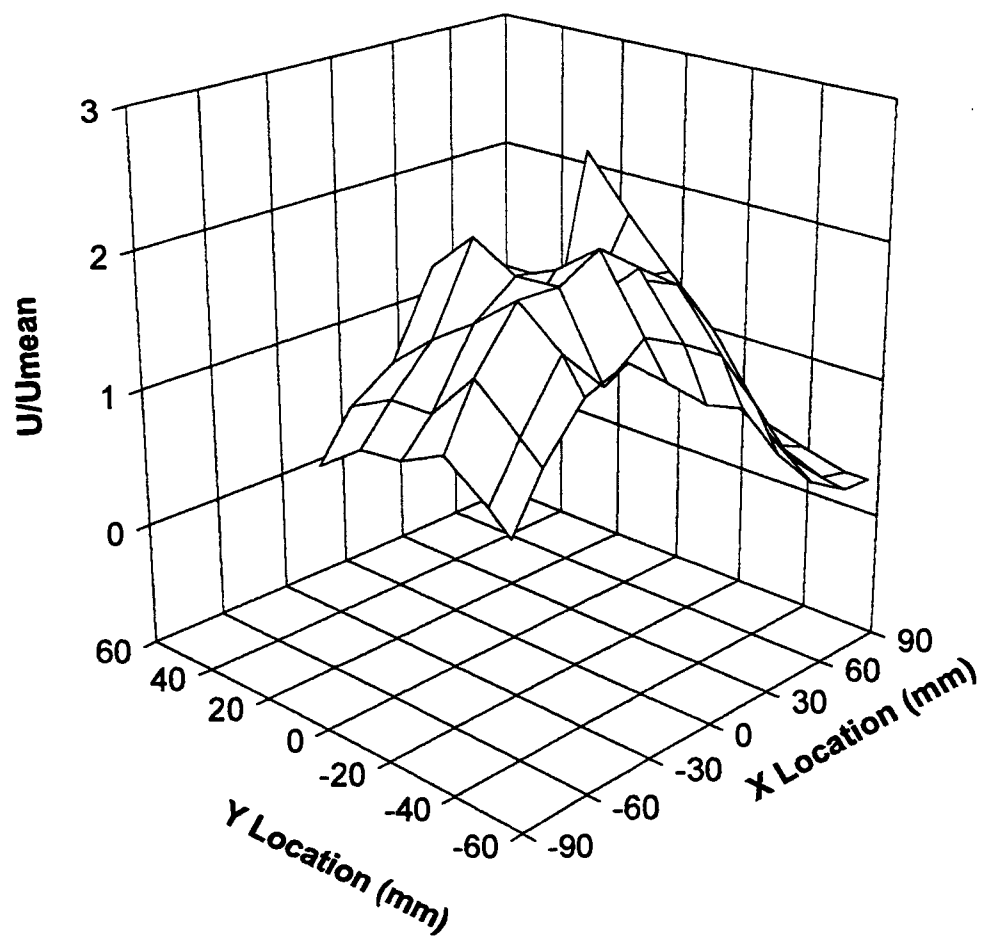


Figure 4.9 Non-Dimensional Axial Velocities in the Test Housing Measured at 51 mm Upstream of the Filter, Plane II, with a 76.2 mm Dia Sphere Positioned at 159 mm Downstream from Housing Inlet.

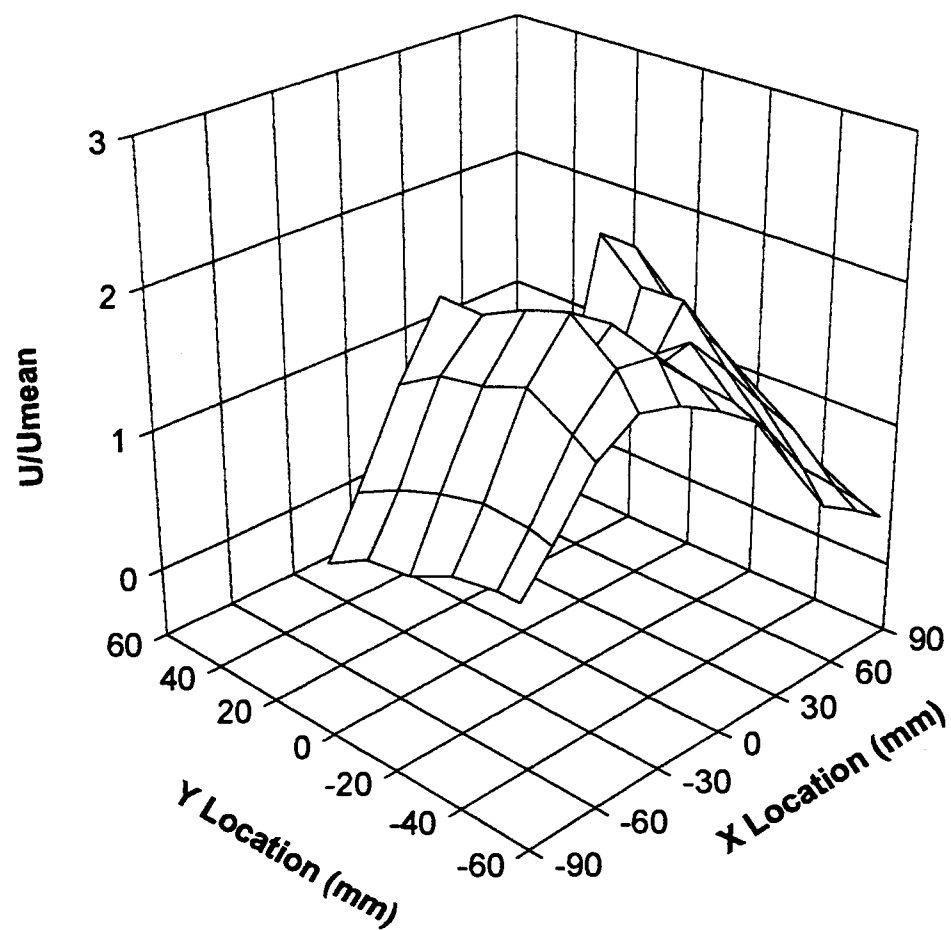


Figure 4.10 Non-Dimensional Axial Velocities in the Test Housing Measured at 13 mm Upstream of the Filter, Plane I, with a 76.2 mm Dia Sphere Positioned at 197 mm Downstream from Housing Inlet.

#### 4.4 Flowrate Comparison of Equally Sized Regions

To better provide an understanding of the flow distribution within the standard SAE test housing, the filter area was divided into sixteen equally sized regions of 30 mm by 48 mm. Only the front eight regions are considered, for  $Y \geq 0.0$  mm. In general, eight regional flow rates may be easily analyzed as compared to sixty-six elemental flow rates. The measured velocities represented in Figures 4.7 to 4.10 from Section 4.3 were integrated across the elemental areas to obtain the elemental flow rates. It was assumed here that (1) all flow going through the filter goes through the measurement grid and (2) recirculating flow along the sides of the filter is negligible. These elemental flow rates were area weighted to obtain the regional flow rates of the eight equally sized regions. The flow rates were then nondimensionalized by dividing all regional flow rates by an operating flow rate of 125 cfm. Note that the non-dimensional flow rates also represent non-dimensional velocities, due to the cancellation of regional areas. For Regions 1 to 4, regions closest to the center line of the filter, a total of 9 data points contributed to each region. For Regions 5 to 8, regions closest to the front edge of the filter, a total of 12 data points contributed to each region. The velocity measurement grid is provided in Figure 3.7.

Figure 4.11 is a non-dimensional plot of the flow rate distribution in the standard SAE test housing with the velocity measurements taken at 13 mm upstream of the filter. As in Figure 4.7, the strongest flow is concentrated in the central region.

An ideally uniform flow pattern would be represented by equal regional flow rates (not necessarily of unity, due to inconsistencies of actual operating flow rates). A maximum and minimum non-dimensional flow rate of 2.24 and 0.74 is obtained in Regions 2 and 8, respectively.

Figure 4.12 is a non-dimensional plot of the flow rate distribution in the test housing with the velocity measurements taken at 13 mm upstream of the filter with a 76.2 mm sphere positioned 159 mm downstream from the housing inlet. Maximum and minimum non-dimensional flow rates of 1.98 and 0.57 are obtained in Regions 2 and 8, respectively. Center Regions 2 and 3 were lowered by 11.8 and 18.6 percent compared to Figure 4.11 without the obstructing sphere. Note the increase in regional flow rates of the front left edge Regions 5 and 6. Furthermore, positioning a sphere downstream of the housing inlet tends to magnify the apparent trend of higher axial velocities along the left side of the filter center line, Regions 1 and 2, and lower axial velocities in the front right corner of the filter, specifically Region 8. As discussed in the previous section, this may be attributed to the exit downstream of the filter located on the right side. This occurrence is present in the three-dimensional velocity profiles of Figures 4.8 to 4.10 and the flow rate distributions of Figures 4.12 to 4.13.

Figure 4.13 is a similar plot with the velocity measurements taken at 13 mm upstream of the filter with the sphere positioned at 197 mm from the housing inlet. Maximum and minimum non-dimensional flow rates of 2.05 and 0.75 were obtained in Regions 6 and 8, respectively. Measurements taken for Figure 4.13 are well within the wake region of the sphere and thus the axial velocities just downstream of the center

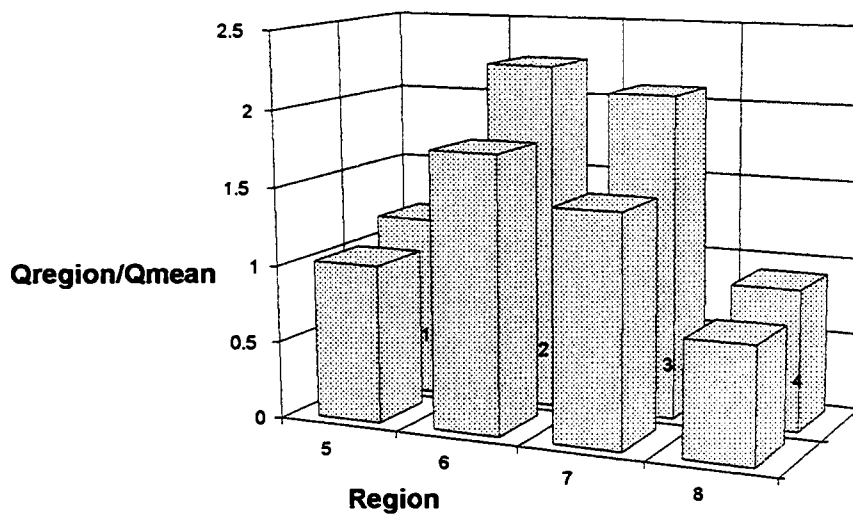


Figure 4.11 Non-Dimensional Flow Rate Distribution in the Standard SAE Test Housing Measured at 13 mm Upstream of the Filter.

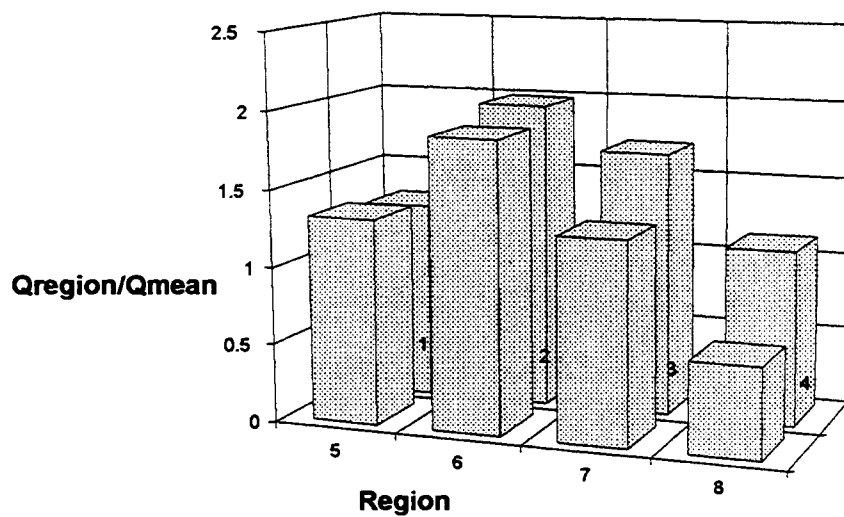


Figure 4.12 Non-Dimensional Flow Rate Distribution in the Test Housing Measured at 13 mm Upstream of the Filter with a 76.2 mm Dia Sphere Positioned at 159 mm Downstream from Housing Inlet.



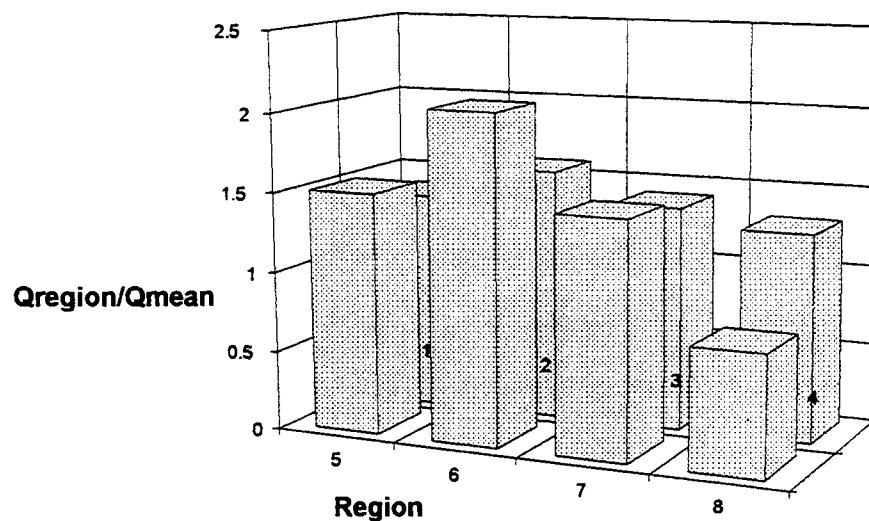


Figure 4.13 Non-Dimensional Flow Rate Distribution in the Test Housing Measured at 13 mm Upstream of the Filter with a 76.2 mm Dia Sphere Positioned at 197 mm Downstream from Housing Inlet.

of the sphere are very low. The Figure 4.13 reveals lower flows in regions along the center line and higher flow rates in the front edge regions, with the exception of Region 8. Finally, a root mean sum, rms, of flow rate differences between the eight regions reveals rms flow rate values of 0.468, 0.423, and 0.337, respectively, for each of the three cases presented in Figures 4.11, 4.12, and 4.13.

#### 4.5 Three-Dimensional Transverse Velocity Profiles

Transverse velocity measurements reveal that the flow within the SAE test housing is much like an impinging jet, rather than a free jet. Non-dimensional

transverse velocity distributions are provided in Figures 4.14 to 4.17. The transverse velocity measurements were non-dimensionalized by dividing each measurement by the calculated average axial velocity through the filter,  $U_{mean} = 2.567$  m/s. Note that transverse velocities are much lower in magnitude than the axial velocities. The positive transverse velocity direction is towards the left, as illustrated in Figure 3.5. Transverse velocity measurements on the left side of the filter tend to be negative while those on the right side of the filter tend to be positive. Figure 4.14 illustrates that as the flow nears the filter, it fans out, much like an impinging jet. The SAE test housing exit leading to the downstream induction blower is positioned to the left of the filter resulting in slightly higher positive transverse velocities on the left side of the filter.

Figure 4.15 is a three-dimensional distribution of the non-dimensional transverse velocities 13 mm upstream of the filter specimen with a 76.2 mm sphere positioned 159 mm downstream of the housing inlet. In general the positive transverse velocities occur on the right side of the filter while the negative velocities occur on the left side. The central region is surrounded by lower positive velocities due to the sphere's wake region. Maximum and minimum non-dimensional transverse velocities of 0.517 (1.33 m/s) and -0.87 (-2.23 m/s) were measured at the right center of the filter and at the left edge, respectively.

Figure 4.16 represents the non-dimensional transverse velocities 51 mm upstream of the filter with a 76.2 mm sphere positioned at 159 mm downstream of the housing inlet. Figure 4.17 is a similar plot of transverse velocities at 13 mm upstream of the filter with a 76.2 mm sphere positioned at 197 mm downstream of the housing inlet. Similar characteristics as in Figures 4.14 and 4.15 are present, resembling an impinging jet flow pattern. Note the close similarities of Figures 4.16 and 4.17. This

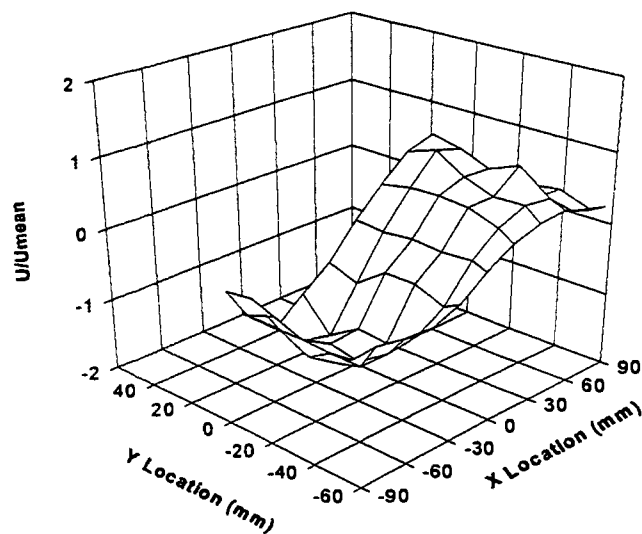


Figure 4.14 Non-Dimensional Transverse Velocities in the Standard SAE Test Housing Measured at 13 mm Upstream of the Filter, Plane I.

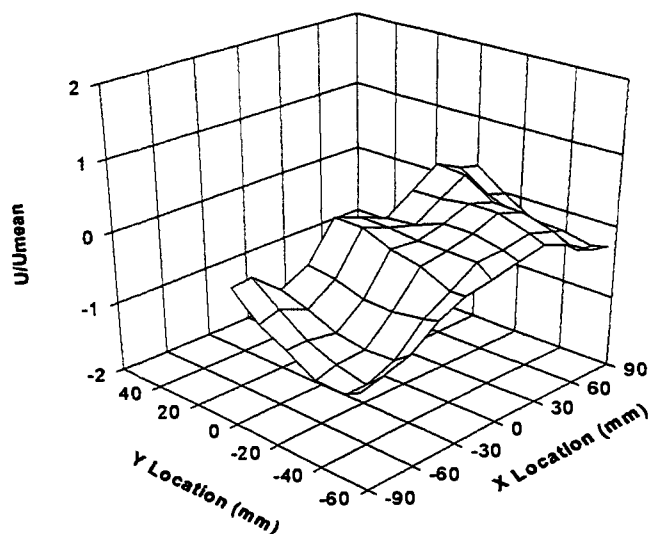


Figure 4.15 Non-Dimensional Transverse Velocities in Test Housing Measured at 13 mm Upstream of the Filter, Plane I, with a 76.2 mm Dia Sphere Positioned at 159 mm Downstream from Housing Inlet.

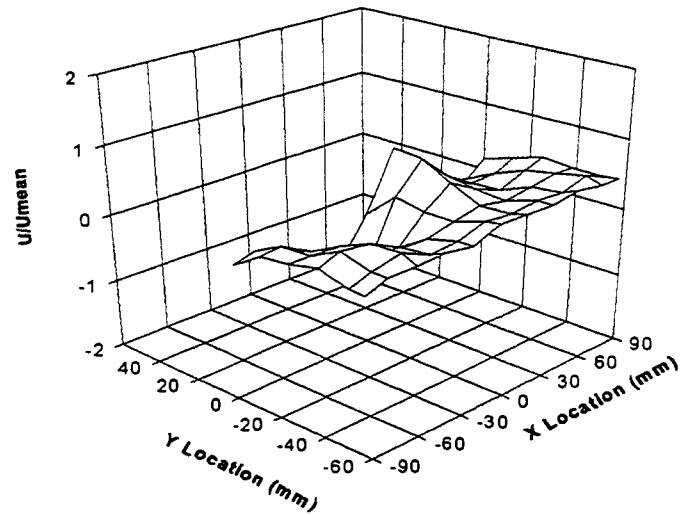


Figure 4.16 Non-Dimensional Transverse Velocities in Test Housing Measured at 51 mm Upstream of the Filter, Plane II, with a 76.2 mm Dia Sphere Positioned at 159 mm Downstream from Housing Inlet.

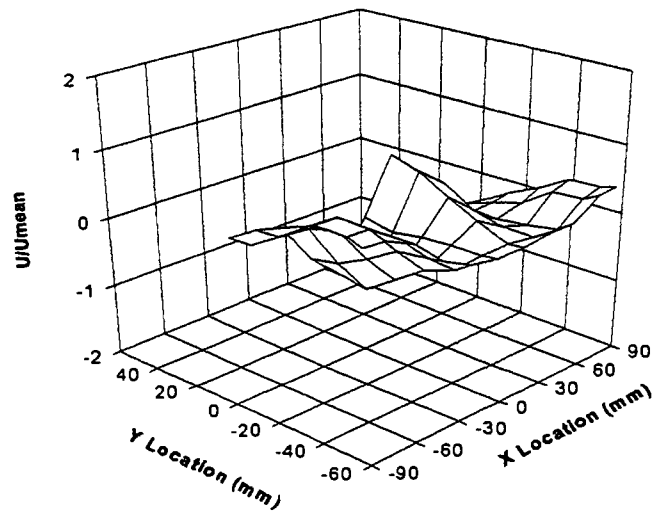


Figure 4.17 Non-Dimensional Transverse Velocities in Test Housing Measured at 13 mm Upstream of the Filter, Plane I, with a 76.2 mm Dia Sphere Positioned at 197 mm Downstream from Housing Inlet.

similarity is attributed to the fact that both sets of data were taken at the same distance downstream of the sphere, 19 mm.

#### 4.6 Turbulence Intensities Upstream of the Filter Specimen

Axial turbulence intensities at 13 mm upstream of the filter are plotted in Figures 4.18 to 4.20. These plots are an indication of the distribution of turbulence in the flow just upstream of the filter. The axial turbulence intensities were obtained by dividing the local rms values of the axial velocity fluctuations about the local mean axial velocity by the maximum mean axial velocity measured above the filter. Without an obstruction, this peak mean axial velocity occurs near the center of the filter. However, due to the obstructing spheres introduced (as in Figures 4.19 and 4.20), the maximum axial velocity is not necessarily at the center of the filter.

From the three-dimensional axial velocity plots of Section 4.3, it is clear that the flow within the test housing is similar to jet flow. Figure 4.18 represents such a turbulence intensity distribution. The central region has high turbulence intensities surrounded by a circular region of higher turbulence intensities. The lower turbulence intensities are closer to the edges of the filter. Similar characteristics are present in Figures 4.19 and 4.20.

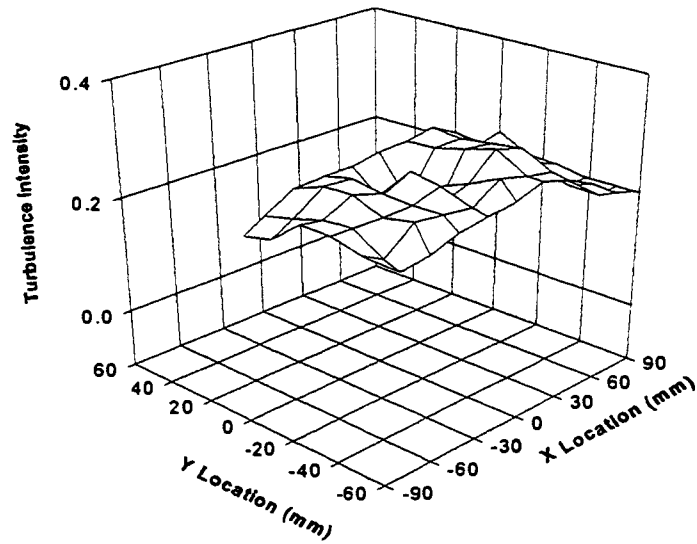


Figure 4.18 Axial Turbulence Intensity in the Test Housing at 13 mm Upstream of the Filter.

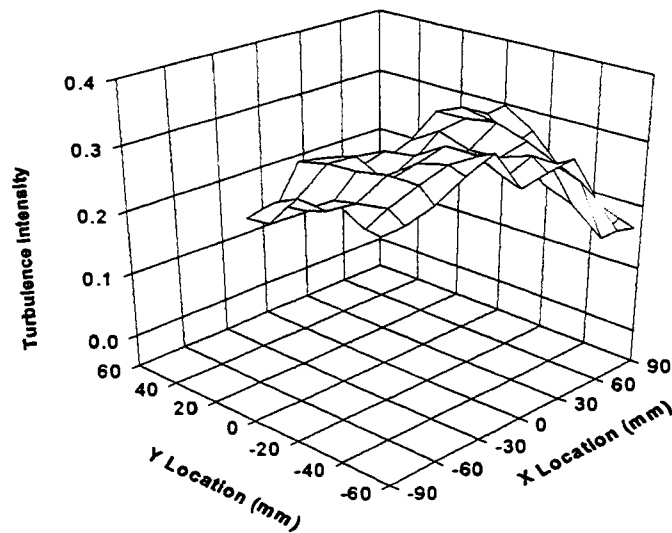


Figure 4.19 Axial Turbulence Intensity at 13 mm Upstream of the Filter with a 76.2 mm Dia Sphere Positioned at 159 mm Downstream of the Housing Inlet.

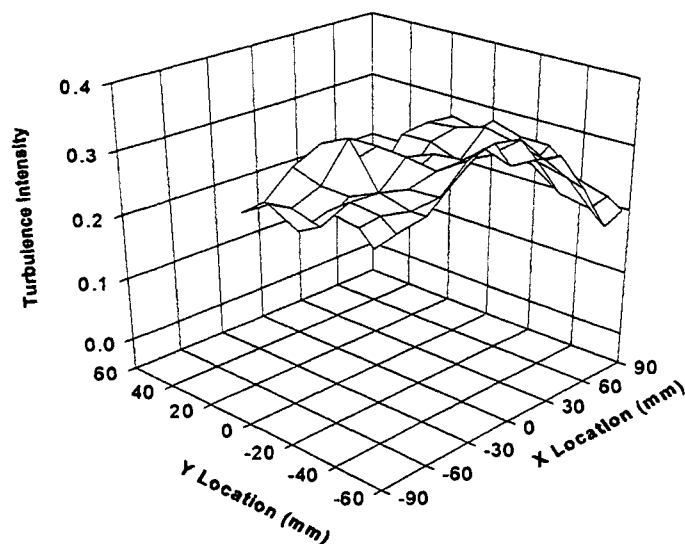


Figure 4.20 Axial Turbulence Intensity at 13 mm Upstream of the Filter with a 76.2 mm Dia Sphere Positioned at 197 mm Downstream of the Housing Inlet.

#### 4.7 Summary of Results

The flow visualizations confirmed with LDV measurements reveal a separated and recirculating flow pattern within the SAE test housing. Furthermore, flow upstream of the filter specimen resembles that of an impinging jet. Obstructing spheres positioned at the inlet allow the inlet flow to be re-distributed away from the central inlet region. However, due to high inlet velocities restricting a sphere's wake region, the flow is re-channelled back to the central region. The larger sized spheres positioned downstream of the inlet appear to be most effective in reducing the axial flow in the central region, resulting in slightly higher velocities near the edges of the filter specimen. Furthermore, maximum velocities are lower by as much as 16 percent

at 13 mm upstream of the filter, compared to a non-obstructed flow. For the 76.2 mm sphere positioned at 159 mm, a flowrate comparison of eight equally sized regions above the front half of the filter reveals lower flow rates of 11.8 and 18.6 percent within the central regions, Regions II and III. Furthermore, a root mean sum, rms, of flow rate differences between the eight regions reveals improved lower rms flow rate values of 0.468, 0.423, and 0.337, respectively, for each of the three cases presented. In summary, by reducing the axial flow in the central region, the 76.2 mm diameter sphere positioned 159 mm downstream of the housing inlet moderately improves the uniformity of flow upstream of the filter specimen. When this same sphere is positioned at 197 mm, variations in regional flow rates are reduced.



## CHAPTER V

### FILTRATION EFFICIENCIES OF PLEATED AIR FILTERS

#### 5.1 General Overview

All computational results presented in this chapter were obtained from the filtration efficiency program developed, EFFMODEL. All efficiency models incorporated in EFFMODEL require axial velocities measurements just upstream of the filter specimen, with the exception of the Lee and Liu (1982b) interception model. Related elemental areas and corresponding aerosol velocities are tabulated. Filtration efficiencies strongly depend on the aerosol velocity inside the filter media. Pleated filter geometry, fiber diameter, packing density, and particle size are other significant factors affecting filtration efficiencies. The existence of large scale variations in the velocities across the filter specimen suggests filtration efficiencies will also vary across the filter specimen.

Single fiber efficiencies and elemental efficiencies for monodisperse particles are presented in three-dimensional form. Furthermore, overall elemental efficiencies for the two grades of polydisperse SAE mass distributions are tabulated and presented. Finally, overall filter efficiencies for both monodisperse and polydisperse aerosols are compared in table form. All calculations are based on an effective uniform fiber diameter of  $51.78 \mu\text{m}$  and a packing density of  $c = 0.345$ . All collection efficiencies assume non-perfect adhesion unless stated otherwise.

The following assumptions were used in all filtration efficiency computations obtained from program EFFMODEL:

1. Non-perfect particle adhesion and retention, as modeled with the Ptak and Jaroszczyk (1990) adhesion model
2. Re-entrainment effects of particles are assumed to be accounted for with the Ptak and Jaroszczyk adhesion model
3. Diffusive filtration mechanisms are negligible
4. Uniform particle concentration per unit volume at filter inlet,  $C_o = (C_{eo})_i$
5. Aerosol particles are monodisperse (polydisperse aerosols are accounted for as individual monodisperse aerosols then weight averaged)
6. Filter packing density,  $c$ , is uniform throughout the filter media
7. Uniform air velocity distribution through the elemental filter media
8. Filter media has a uniform fiber diameter
9. Filter media is clean and free of clogging.

## 5.2 Single Fiber Efficiencies within Pleated Air Filters

Single fiber efficiencies strongly depend on the aerosol velocity inside the filter media. Due to the variations in axial velocities upstream of the filter specimen, as presented in Chapter IV, similar variations in single fiber efficiencies are present. Single fiber efficiency distributions are provided in Figures 5.1 to 5.4. The efficiencies are plotted in three-dimensional form. As in Chapter IV, the three-dimensional distributions represent the front half of the filter specimen.

Figure 5.1 shows the single fiber efficiency of a clean filter within the SAE test housing assuming perfect adhesion. Note the similarity of the bell-shaped dome

compared to Figure 4.7. The single fiber efficiencies are highest in the central region where the velocities are highest and lowest along the edges where the velocities are lowest. Figure 5.2 represents the single fiber efficiencies of a clean filter with non-perfect adhesion. The central region here is leveled off with lower efficiencies throughout the center. At higher velocities, as illustrated in Figures 2.5 and 2.13, the retention or adhesion of particles is lowered. Adhesion efficiencies within the central region are in the neighborhood of 0.73 as compared to 0.92 at the edges of the filter. This results in significantly lower single fiber efficiencies within the central region. Figure 5.1 has maximum single fiber efficiency of 0.90 near the center compared to Figure 5.2 with a maximum of 0.61 to the left of the center.

Figures 5.3 and 5.4 represent the single fiber efficiencies with a 76.2 mm sphere positioned 159 mm downstream of the housing inlet assuming perfect and non-perfect adhesion, respectively. Similar characteristics as in Figures 5.1 and 5.2 are present. Figure 5.3 has maximum single fiber efficiency of 0.86 near the center compared to Figure 5.4 with a maximum of 0.61 also near the center.

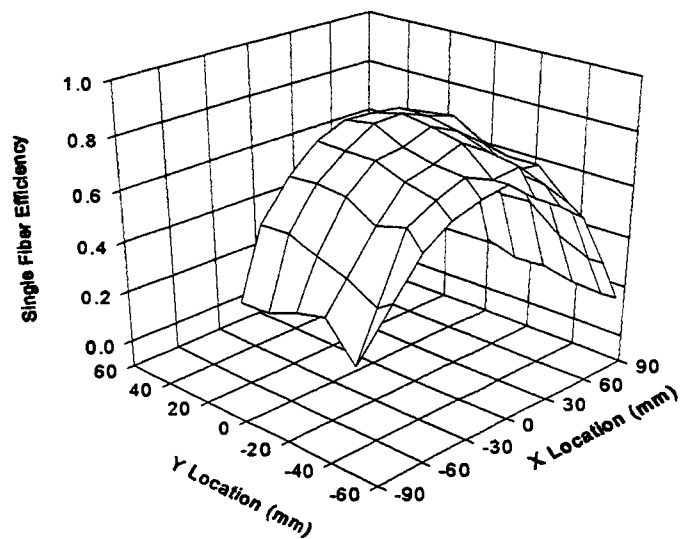


Figure 5.1 Single Fiber Efficiency in Standard SAE Test Housing Assuming Perfect Adhesion, 5  $\mu\text{m}$  Particles.

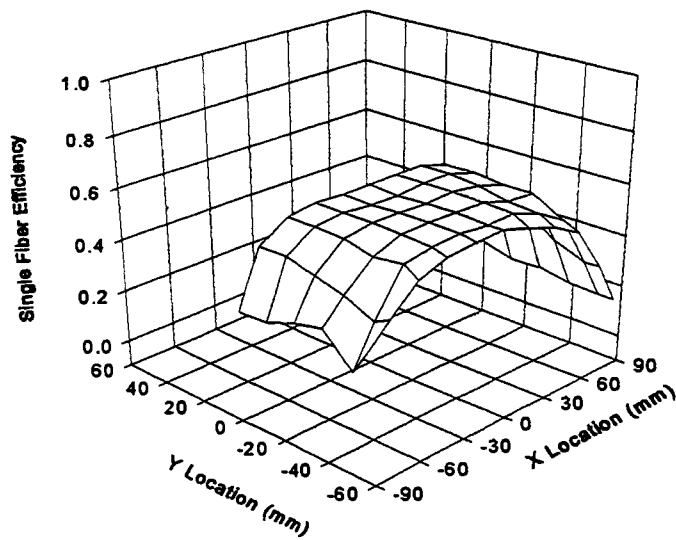


Figure 5.2 Single Fiber Efficiency in Standard SAE Test Housing, 5  $\mu\text{m}$  Particles.

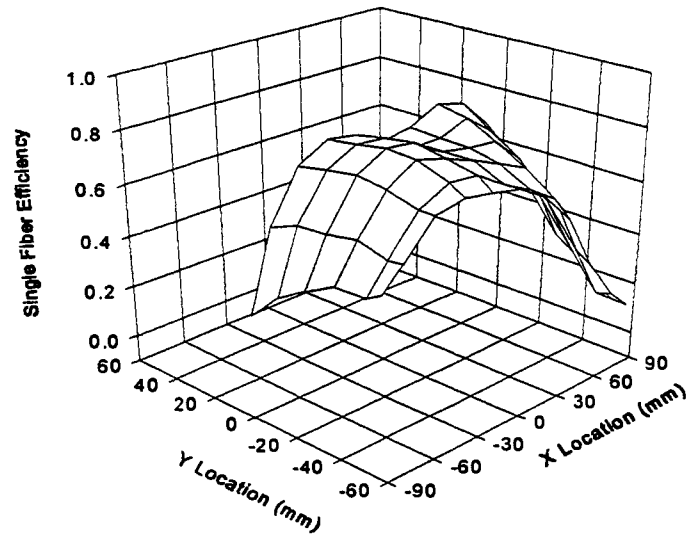


Figure 5.3 Single Fiber Efficiency Assuming Perfect Adhesion with 76.2 mm Dia Sphere Positioned at 159 mm Downstream of the Housing Inlet, 5  $\mu$ m Particles.

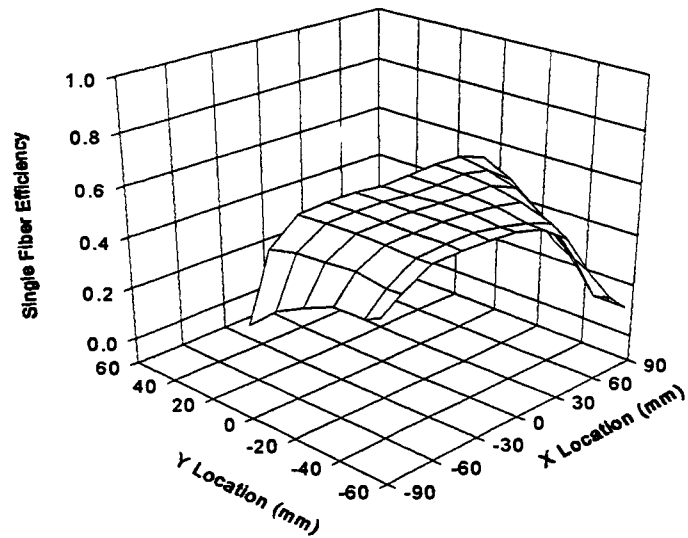


Figure 5.4 Single Fiber Efficiency with 76.2 mm Dia Sphere Positioned at 159 mm Downstream of the Housing Inlet, 5  $\mu$ m Particles.

### 5.3 Elemental Efficiencies Across Pleated Air Filter Beds

Elemental efficiencies for the filter beds were obtained assuming perfect and non-perfect adhesion. Various plots of elemental efficiency distributions are provided in Figures 5.5 to 5.16 for the specified monodisperse particle sizes. With the exception of Figure 5.13, all figures represent elemental efficiencies assuming non-perfect adhesion. At a particle size of  $1.0\ \mu\text{m}$ , the aerosol is small enough to penetrate through the filter bed with an overall penetration of 0.96 or greater, as illustrated in Figures 5.5 and 5.6.

At a particle size of  $2.5\ \mu\text{m}$ , Figures 5.7 and 5.8, an elemental efficiency distribution shaped similar to that of the bell-shaped dome of the three-dimensional velocity distributions is present. Again, filtration efficiencies strongly depend on the aerosol velocities for this particle size. Thus, if variations exist in the velocity distributions, similar variations will be present in the efficiency distributions. Figures 5.7 and 5.8 represent an overall filter efficiency of 0.726 and 0.699, respectively, for the  $2.5\ \mu\text{m}$  monodisperse particles.

Smaller particles are easier to filter than larger sized particles. At a particle size of  $5.0\ \mu\text{m}$ , Figures 5.9 and 5.10, an elemental efficiency distribution of unity is present away from the edges of the filters where the velocities are lowest. With a larger particle size of  $7.5\ \mu\text{m}$ , Figures 5.11 and 5.12 illustrate an elemental efficiency distribution of unity with the exception of the right side edges. The elemental efficiency distributions of Figures 5.9 and 5.10 both have an overall filter efficiency of 0.989, for the  $5.0\ \mu\text{m}$  monodisperse particles. For the  $7.5\ \mu\text{m}$  monodisperse particles, the elemental efficiency distributions of Figures 5.11 and 5.12 have an overall filter efficiency of 0.993 and 0.995.

Up to this point, all elemental efficiency distributions presented assumed non-perfect adhesion. Similar distributions of elemental efficiencies assuming perfect adhesion were plotted and revealed no visible differences from the plots presented in Figures 5.5 to 5.12 assuming non-perfect adhesion. Actual tabulations result in a maximum difference between elemental efficiencies assuming perfect adhesion to elemental efficiencies assuming non-perfect adhesion of +0.007 (0.7 percent difference). At large particle sizes  $\geq 15\mu\text{m}$ , the adhesion model approaches low values of adhesion. As discussed in Sub-Section 2.8.4, as the particle size is increased the adhesion model tabulations decrease in value and approach zero.

Figure 5.13 illustrates an elemental efficiency distribution of unity assuming perfect adhesion for a monodisperse particle size of  $D_p \geq 15\mu\text{m}$ . Assuming non-perfect adhesion, the elemental efficiencies for  $7.5\mu\text{m}$  particles are presented in Figures 5.14 to 5.16. The elemental efficiency distributions differ from unity. The areas of lower efficiencies correspond to the areas of higher velocities. Furthermore, as the monodisperse particle size was increased up to  $140\mu\text{m}$ , the elemental efficiency distribution assuming non-perfect adhesion was significantly lowered approaching overall filter efficiencies of 0.044. Such low efficiencies are not realistic. Particle sizes may be too large for the adhesion model. Essentially, if a particle is too large to penetrate through a filter, the filter efficiency is understood to be 1.00, the particle is captured by sieving.

Overall filter efficiencies assuming perfect and non-perfect adhesion are provided in Table 5.1, for the specified particle sizes. Note that for particle sizes  $\geq 5.0\mu\text{m}$ , an increase in the overall filter efficiencies was achieved by obstructing the flow with a 76.2 mm diameter sphere. A maximum improvement of 2.6 percent in overall filter efficiency is achieved, with  $30\mu\text{m}$  particles. For a filter of packing density  $c =$

0.345 and an effective fiber diameter of  $D_f = 51.78 \mu\text{m}$ , at a monodisperse particle size of  $D_p \geq 15 \mu\text{m}$ , the overall filter efficiency assuming perfect adhesion reaches unity. However, if the adhesion probability of a particle is modeled using the Ptak and Jaroszczyk adhesion model, overall filter efficiencies at a particle size  $\geq 15 \mu\text{m}$  descend and approach zero. Again, such low efficiencies are not realistic. The particle sizes are apparently too large for the adhesion model. Recall that the authors, Ptak and Jaroszczyk, do not indicate any limits or bounds for the adhesion model.

The Ptak and Jaroszczyk (1990) adhesion model does appear to work well for smaller sized particles. It is recommended here that the Ptak and Jaroszczyk adhesion model be further investigated and implemented in efforts to determine an upper bound of particle sizes. Perhaps the parameters  $a_0$ ,  $b_0$ , and  $c_0$  of Equation (2.43) can be experimentally determined to include a larger range of particle sizes or a separate range for larger particles.



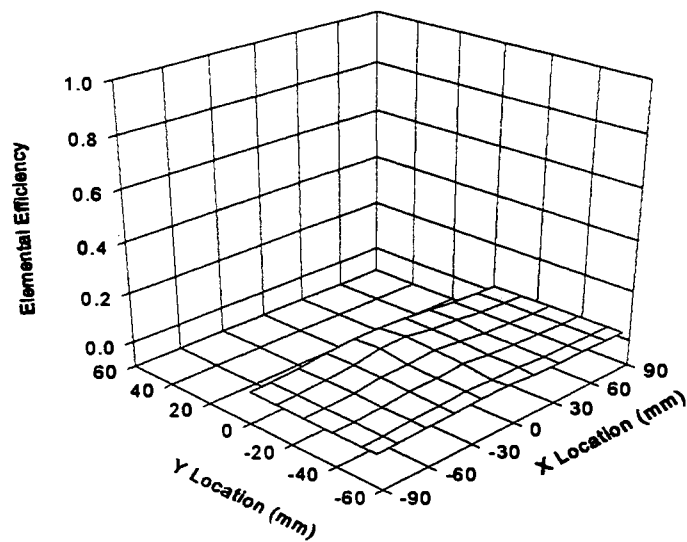


Figure 5.5 Elemental Efficiency in Standard SAE Test Housing, 1.0  $\mu\text{m}$  Particles.

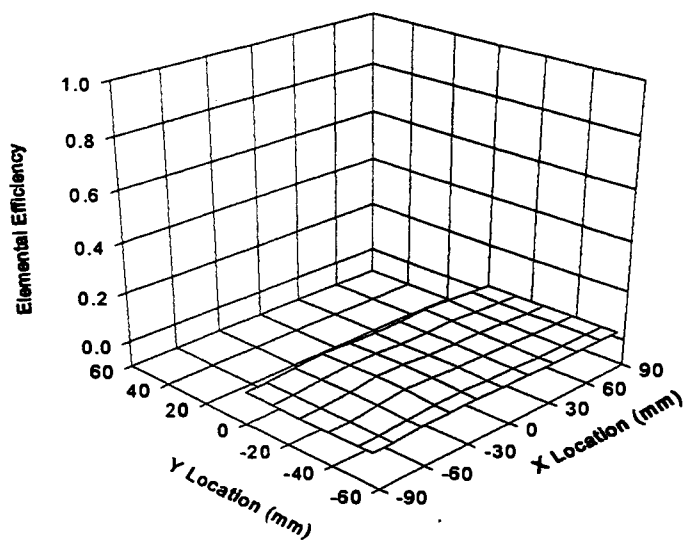


Figure 5.6 Elemental Efficiency with 76.2 mm Dia Sphere Positioned at 159 mm Downstream of the Housing Inlet, 1.0  $\mu\text{m}$  Particles.

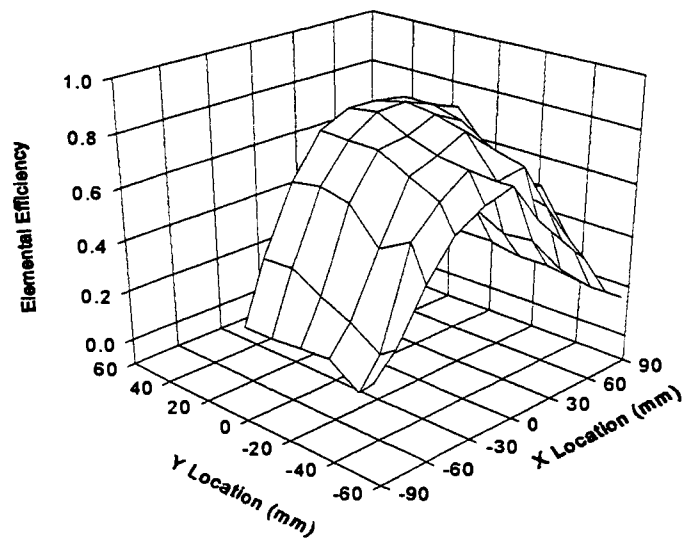


Figure 5.7 Elemental Efficiency in Standard SAE Test Housing, 2.5  $\mu\text{m}$  Particles.

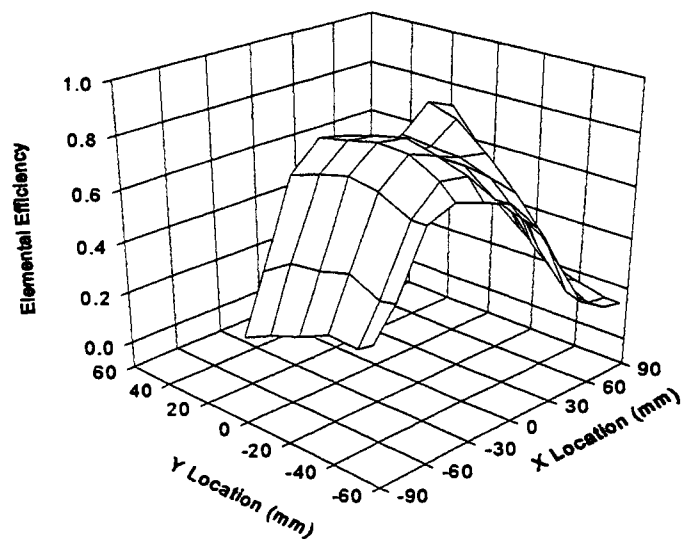


Figure 5.8 Elemental Efficiency with 76.2 mm Dia Sphere Positioned at 159 mm Downstream of the Housing Inlet, 2.5  $\mu\text{m}$  Particles.

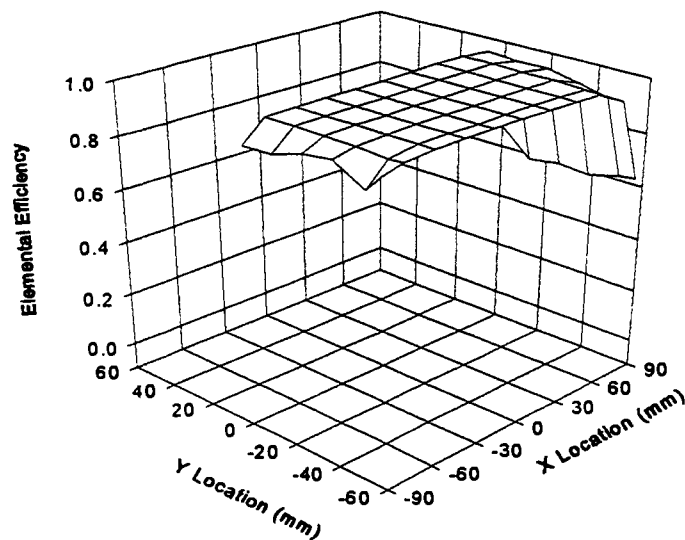


Figure 5.9 Elemental Efficiency in Standard SAE Test Housing, 5.0  $\mu\text{m}$  Particles.

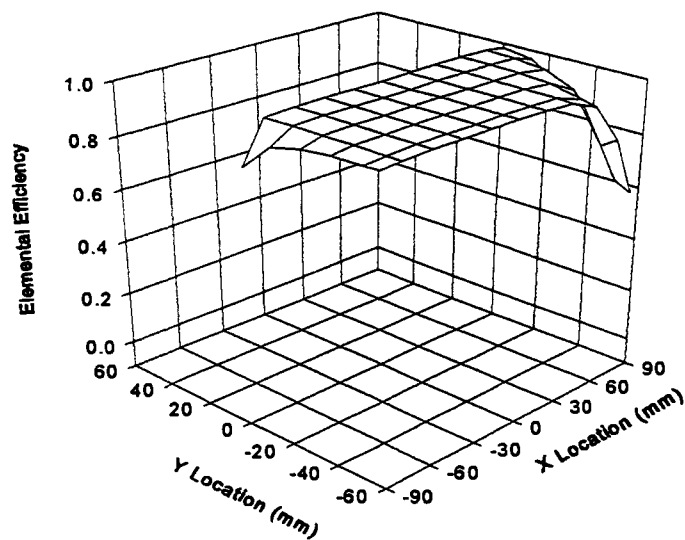


Figure 5.10 Elemental Efficiency with 76.2 mm Dia Sphere Positioned at 159 mm Downstream of the Housing Inlet, 5.0  $\mu\text{m}$  Particles.

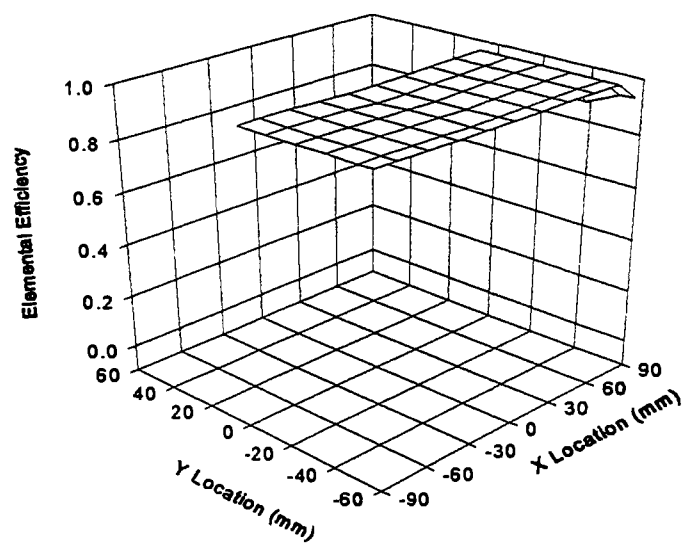


Figure 5.11 Elemental Efficiency in Standard SAE Test Housing, 7.5  $\mu\text{m}$  Particles.

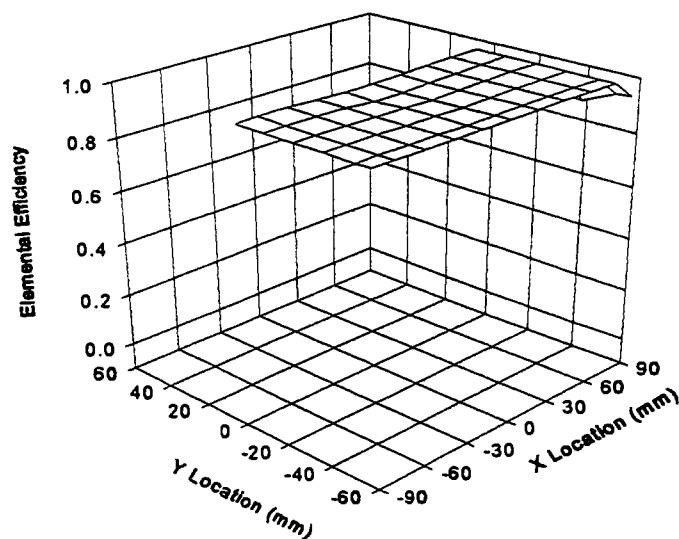


Figure 5.12 Elemental Efficiency with 76.2 mm Dia Sphere Positioned at 159 mm Downstream of the Housing Inlet, 7.5  $\mu\text{m}$  Particles.

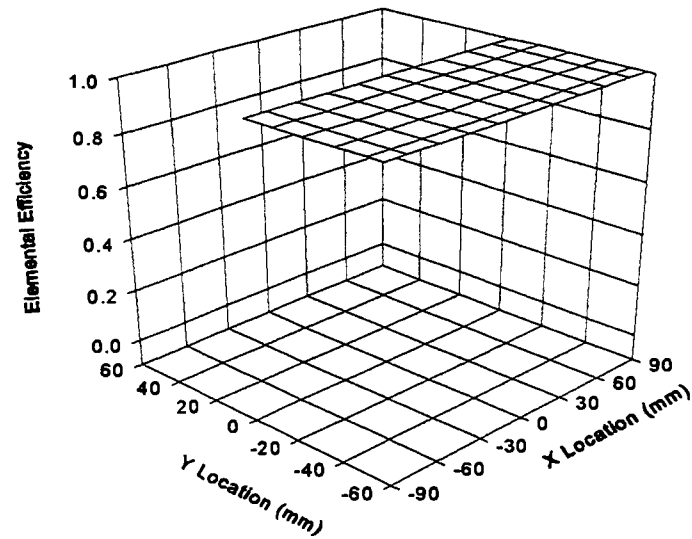


Figure 5.13 Elemental Efficiency of Unity Across Filter Assuming Perfect Adhesion with or without 76.2 mm Dia Sphere Positioned either 159 mm or 197 mm Downstream of the Housing Inlet, for Particle Sizes  $\geq 15.0 \mu\text{m}$ .

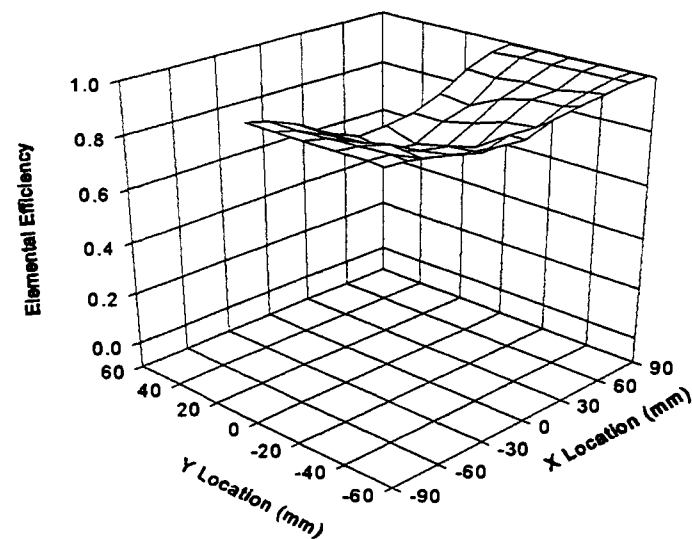


Figure 5.14 Elemental Efficiency in Standard SAE Test Housing,  $15.0 \mu\text{m}$  Particles.

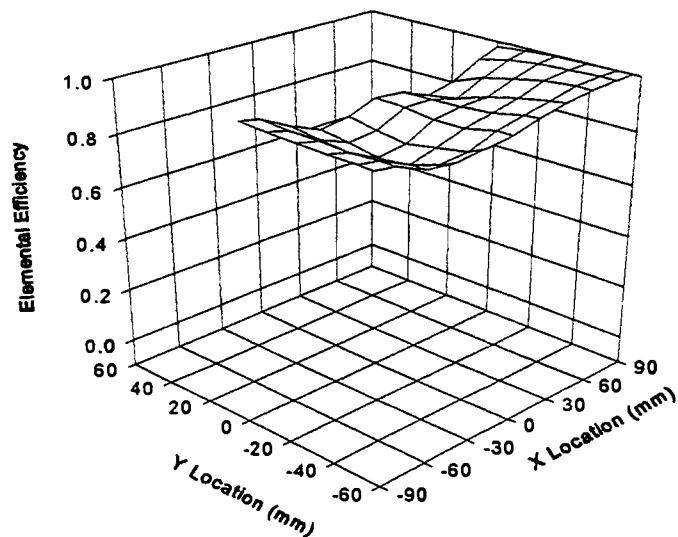


Figure 5.15 Elemental Efficiency with 76.2 mm Dia Sphere Positioned at 159 mm Downstream of the Housing Inlet, 15.0  $\mu\text{m}$  Particles.

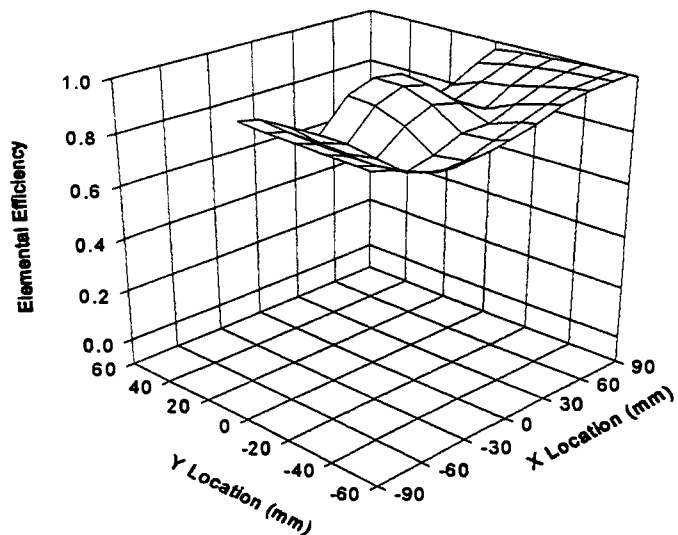


Figure 5.16 Elemental Efficiency with 76.2 mm Dia Sphere Positioned at 197 mm Downstream of the Housing Inlet, 15.0  $\mu\text{m}$  Particles.

Table 5.1 Overall Filter Efficiencies Assuming a Monodisperse Particle Size Distribution

Overall Filter Efficiencies for the Specified Monodisperse Particle Sizes						
Particle Diameter [ $\mu\text{m}$ ]	Without Sphere		Sphere at 159 mm		Sphere at 197 mm	
	Perfect Adhesion	Non-Perf. Adhesion	Perfect Adhesion	Non-Perf. Adhesion	Perfect Adhesion	Non-Perf. Adhesion
1.0	0.039	0.038	0.035	0.034	0.036	0.035
2.5	0.745	0.726	0.718	0.699	0.727	0.708
5.0	0.993	0.989	0.993	0.989	0.994	0.990
7.5	0.999	0.993	0.999	0.995	1.000	0.995
15.0	1.000	0.903	1.000	0.920	1.000	0.914
30.0	1.000	0.548	1.000	0.574	1.000	0.565
60.0	1.000	0.205	1.000	0.217	1.000	0.212
140.0	1.000	0.044	1.000	0.046	1.000	0.044

#### 5.4 Overall Elemental Efficiencies for SAE Test Dust Particle Distributions

Under actual operating conditions, automotive air filters are never exposed to monodisperse particles. In efforts to provide a realistic understanding of the filtration efficiency performance for a polydisperse aerosol, the two grades of SAE test dust distributions were incorporated into program EFFMODEL. The fine and coarse grade

particle distributions are presented in Table 1.1. Overall elemental efficiency distributions were tabulated and plotted assuming perfect and non-perfect adhesion for both the fine and coarse grade SAE particle mass distributions. Refer to Figures 5.19 to 5.30. Related overall filter efficiencies were also calculated and are presented in table form.

As presented in the previous section, overall filter efficiencies for a monodisperse particle size of  $D_p \geq 5.0 \mu\text{m}$ , the elemental efficiency distributions are flat with a value of unity with the exception of some points along the edges. Furthermore, at monodisperse particle sizes of  $D_p < 5.0 \mu\text{m}$ , the elemental efficiency distributions are far from unity. In order to model the effects of a polydisperse particle distribution, ranging from 0.0 to 200.0  $\mu\text{m}$  sized particles, it is necessary to include a range of particles  $D_p < 5.0 \mu\text{m}$ . The standard SAE test dust distributions by weight do not include an interval range of particle sizes finer than 5.0  $\mu\text{m}$ . Thus, in efforts to include efficiency computations for particle sizes  $< 5.0 \mu\text{m}$ , a linear log - probability or log - mass fraction relationship was assumed. The two SAE distributions are provided as a cumulative mass fraction distribution in Figures 5.17 and 5.18.

Both distributions were assumed to be lognormally distributed, thus the cumulative distributions of the plots shown are straight lines. The SAE polydisperse distributions were scaled down to include the smaller interval ranges, obtained from Figures 5.17 and 5.18. The actual polydisperse distributions incorporated into EFFMODEL are provided in Table 5.2.



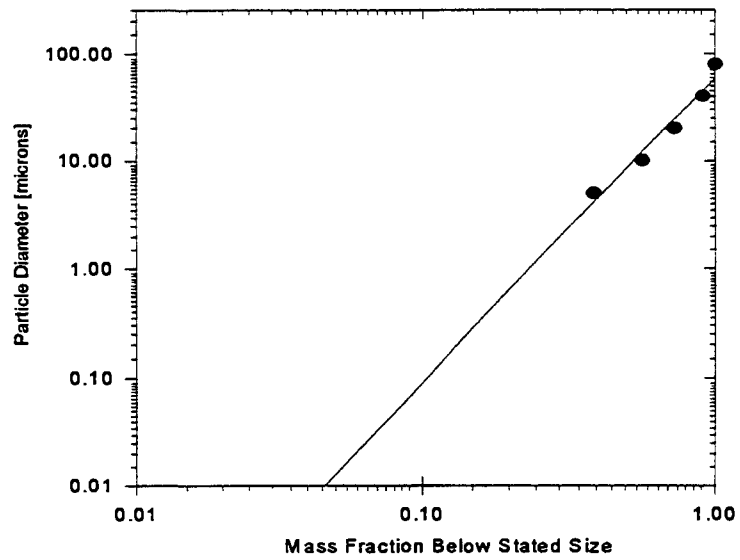


Figure 5.17 Cumulative Mass Fraction Distribution of SAE Polydisperse Fine Grade Test Dust

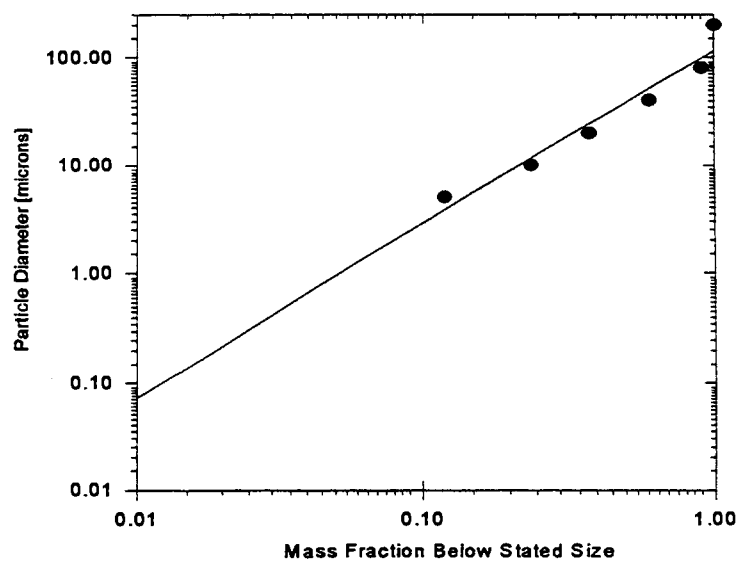


Figure 5.18 Cumulative Mass Fraction Distribution of SAE Polydisperse Coarse Grade Test Dust

Table 5.2 Standard SAE Polydisperse Test Dust Distributions by Percent Weight

Polydisperse Particle Size Distribution by Percent Weight		
Size [ $\mu\text{m}$ ]	Fine Grade % Weight	Coarse Grade % Weight
0.0 - 1.5	27.4	6.5
1.5 - 3.0	7.6	3.5
3.0 - 5.0	4.0	2.0
5.0 - 10.0	18.0	12.0
10.0 - 20.0	16.0	14.0
20.0 - 40.0	18.0	23.0
40.0 - 80.0	9.0	30.0
80.0 - 200.0	-	9.0

The overall elemental efficiency distributions for the specified SAE test dust distributions are provided in Figures 5.19 to 5.30. All three cases are represented: SAE test housing without obstruction, 76.2 mm diameter sphere at 159 mm, and 76.2

mm diameter sphere at 197 mm. Smaller particles are easier to filter than larger sized particles. Consequently, lower efficiencies are achieved with the fine grade test dust compared to the coarse grade test dust. Furthermore, the coarse grade test dust provides a smoother distribution throughout the filter specimen, as illustrated in Figures 5.21, 5.25, and 5.29.

Overall filter efficiencies assuming perfect and non-perfect adhesion are provided in Table 5.3, for the specified SAE polydisperse distribution. When perfect adhesion is assumed, the obstructed flows do not improve the overall filter efficiency. In fact, lower filter efficiencies are achieved. It is apparent from the figures that a smoother efficiency distribution is achieved with the unobstructed flow, for perfect adhesion. Note from Table 5.3 that the overall filter efficiencies assuming non-perfect adhesion are improved by obstructing the flow. This may be attributed to the fact that higher peak velocities, from the unobstructed flow, result in lower adhesion values. Furthermore, the fact that all of the overall elemental efficiency distributions assuming non-perfect adhesion are concave downward, suggests that at large particle diameters the Ptak and Jaroszczyk (1990) adhesion model is dominated by peak velocities resulting in lower adhesion efficiencies.

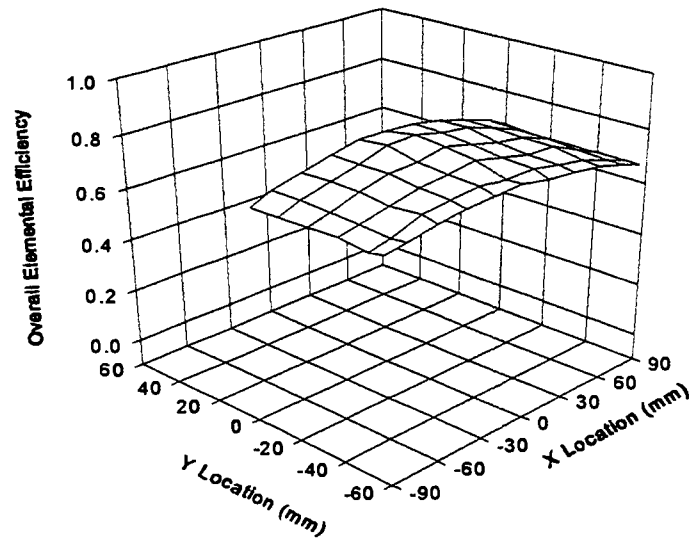


Figure 5.19 Overall Elemental Efficiency in Standard SAE Test Housing Assuming Perfect Adhesion, SAE Fine Grade Test Dust Distribution.

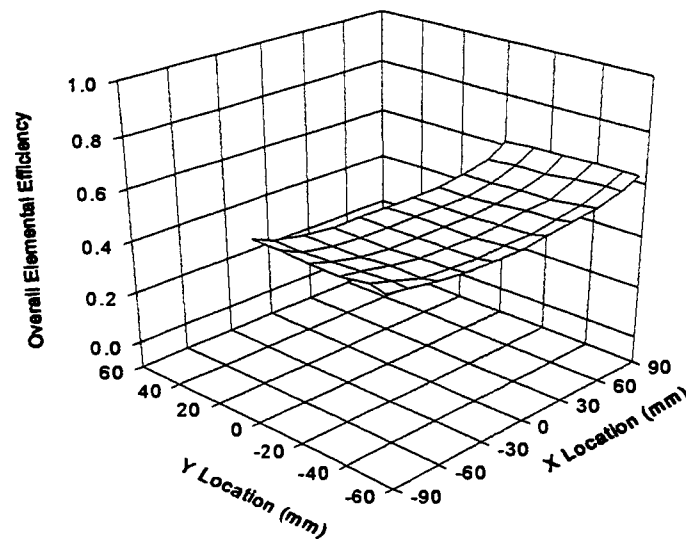


Figure 5.20 Overall Elemental Efficiency in Standard SAE Test Housing, SAE Fine Grade Test Dust Distribution.

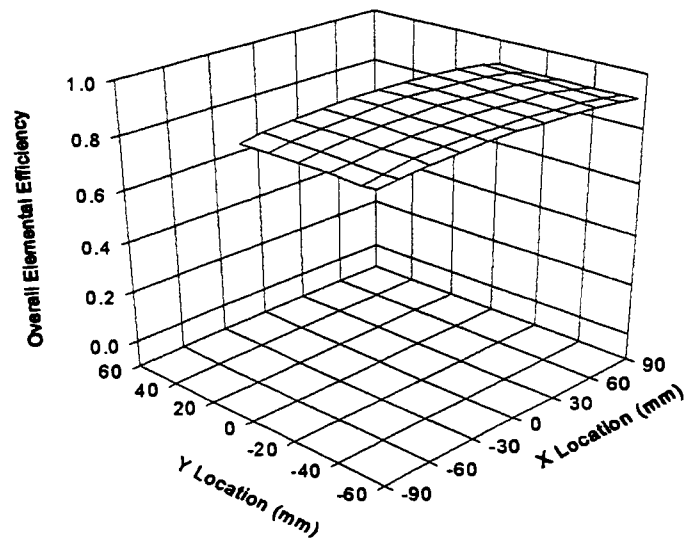


Figure 5.21 Overall Elemental Efficiency in Standard SAE Test Housing Assuming Perfect Adhesion, SAE Coarse Grade Test Dust Distribution.

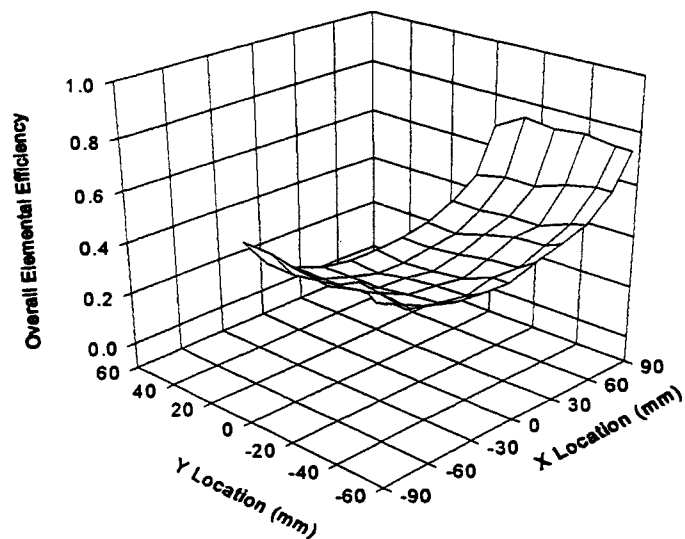


Figure 5.22 Overall Elemental Efficiency in Standard SAE Test Housing, SAE Coarse Grade Test Dust Distribution.

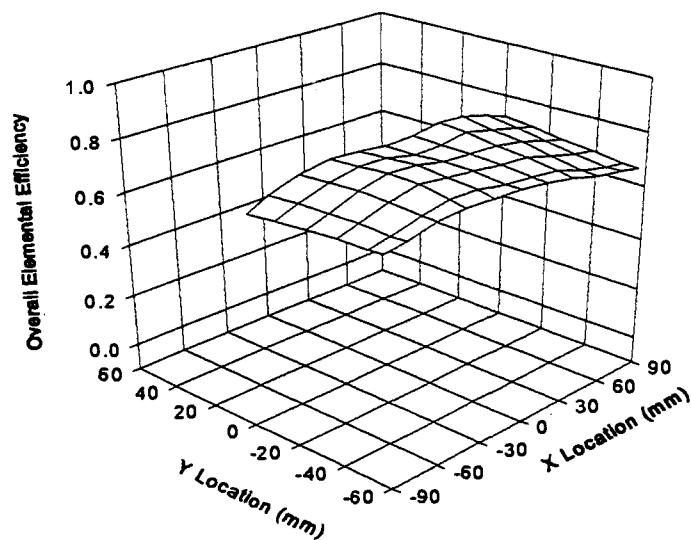


Figure 5.23 Overall Elemental Efficiency Assuming Perfect Adhesion with 76.2 mm Dia Sphere Positioned at 159 mm Downstream of the Housing Inlet, SAE Fine Grade Test Dust Distribution.

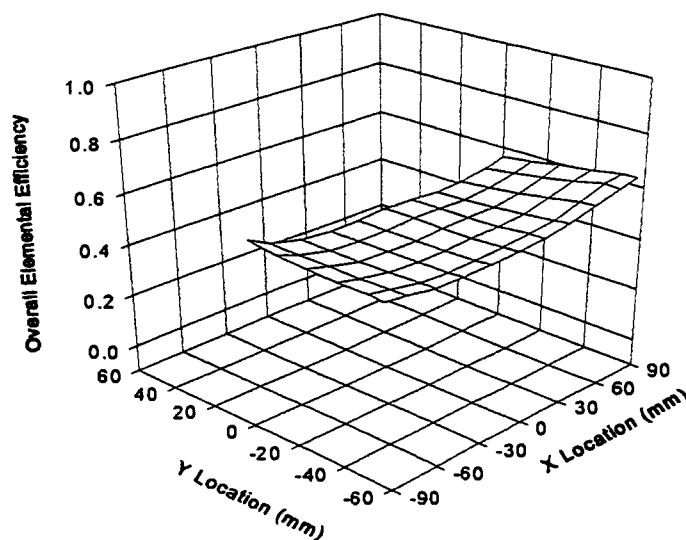


Figure 5.24 Overall Elemental Efficiency with 76.2 mm Dia Sphere Positioned at 159 mm Downstream of the Housing Inlet, SAE Fine Grade Test Dust Distribution.

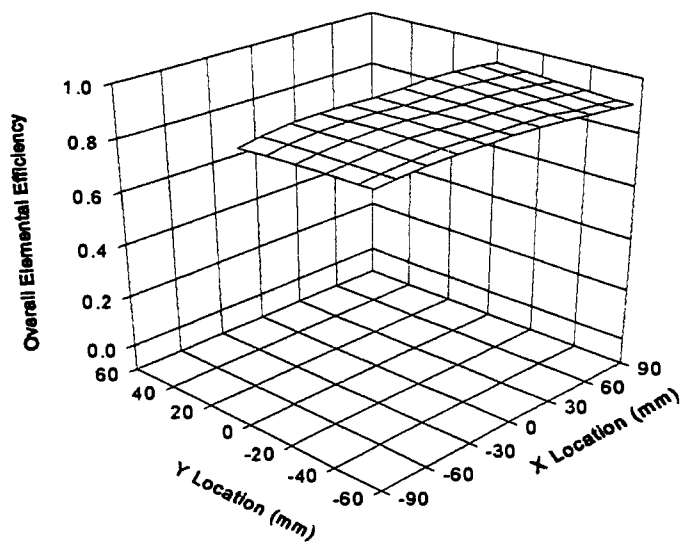


Figure 5.25 Overall Elemental Efficiency Assuming Perfect Adhesion with 76.2 mm Dia Sphere Positioned at 159 mm Downstream of the Housing Inlet, SAE Coarse Grade Test Dust Distribution.

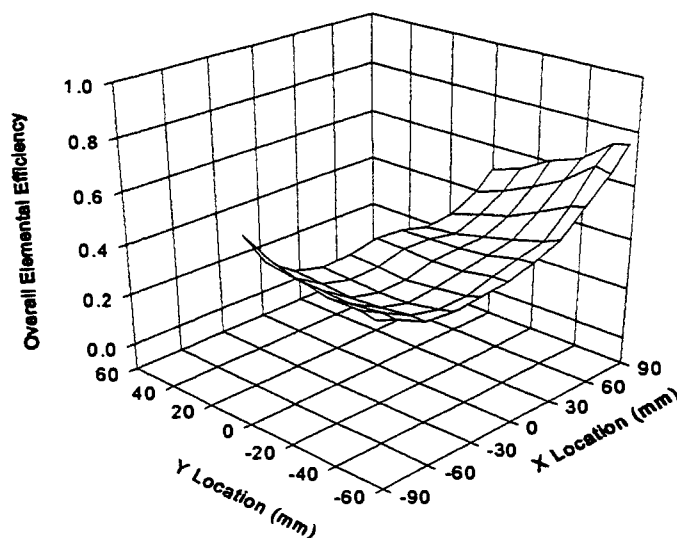


Figure 5.26 Overall Elemental Efficiency with 76.2 mm Dia Sphere Positioned at 159 mm Downstream of the Housing Inlet, SAE Coarse Grade Test Dust Distribution.

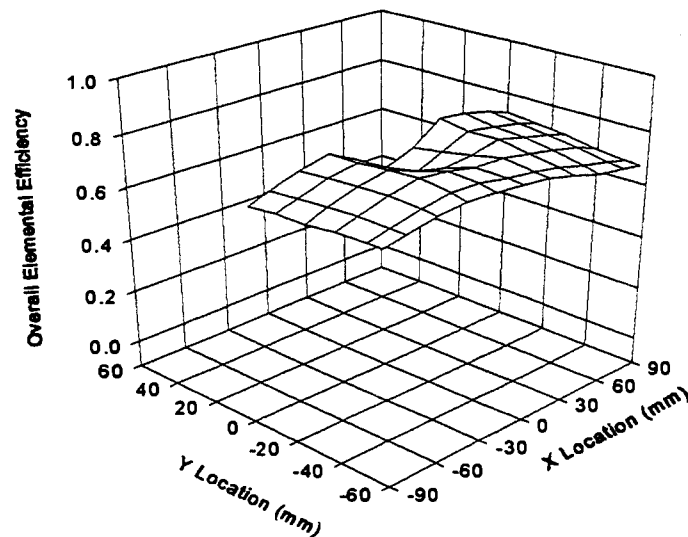


Figure 5.27 Overall Elemental Efficiency Assuming Perfect Adhesion with 76.2 mm Dia Sphere Positioned at 197 mm Downstream of the Housing Inlet, SAE Fine Grade Test Dust Distribution.

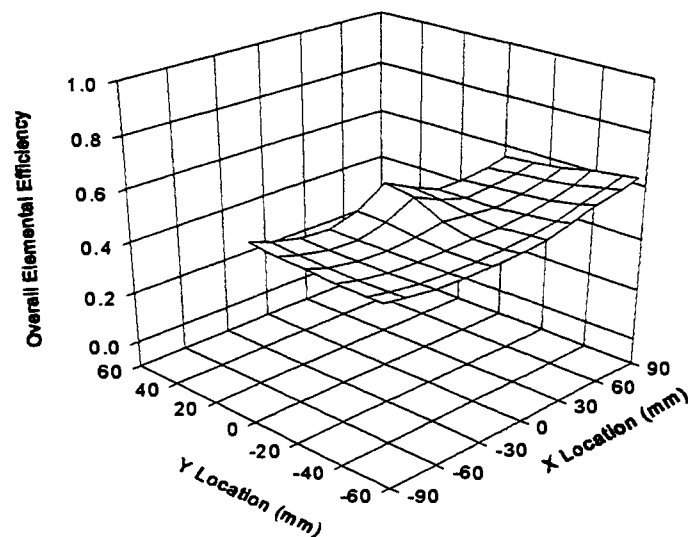


Figure 5.28 Overall Elemental Efficiency with 76.2 mm Dia Sphere Positioned at 197 mm Downstream of the Housing Inlet, SAE Fine Grade Test Dust Distribution.



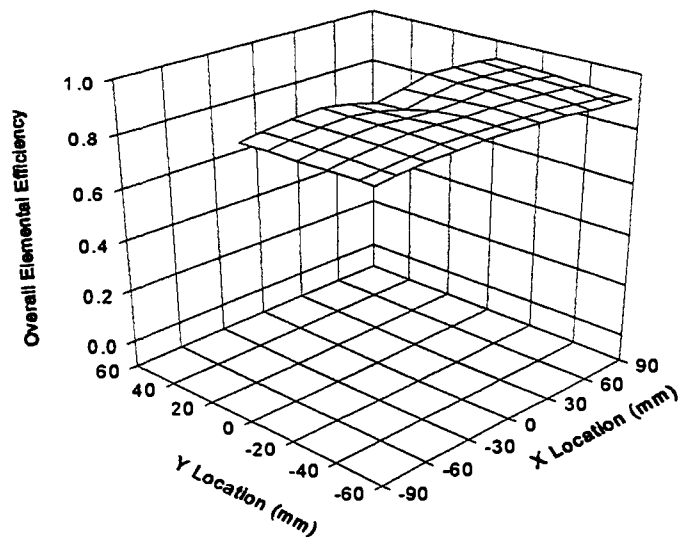


Figure 5.29 Overall Elemental Efficiency Assuming Perfect Adhesion with 76.2 mm Dia Sphere Positioned at 197 mm Downstream of the Housing Inlet, SAE Coarse Grade Test Dust Distribution.

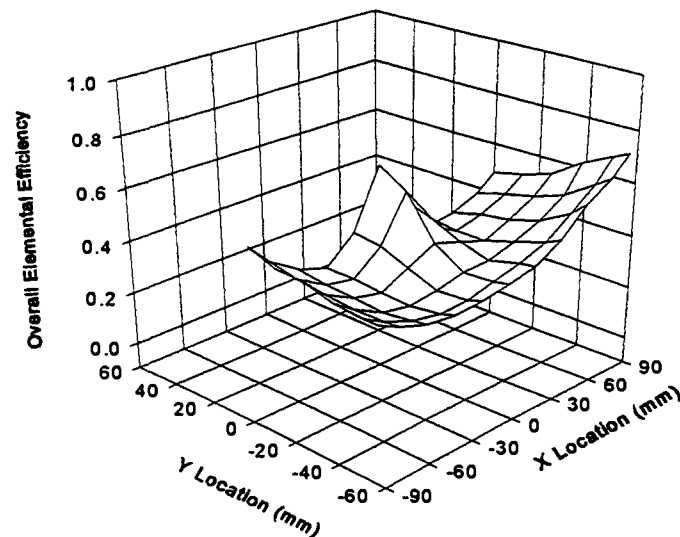


Figure 5.30 Overall Elemental Efficiency with 76.2 mm Dia Sphere Positioned at 197 mm Downstream of the Housing Inlet, SAE Coarse Grade Test Dust Distribution.

Table 5.3 Overall Filter Efficiencies for the Standard SAE Polydisperse Test Dust Distributions

Overall Filter Efficiencies for the Specified Polydisperse Particle Distributions						
Particle Dist.	Without Sphere		Sphere at 159 mm		Sphere at 197 mm	
	Perfect Adhesion	Non-Perf. Adhesion	Perfect Adhesion	Non-Perf. Adhesion	Perfect Adhesion	Non-Perf. Adhesion
SAE Fine	0.766	0.535	0.758	0.537	0.761	0.536
SAE Coarse	0.942	0.416	0.940	0.425	0.941	0.422

### 5.5 Summary of Efficiency Results

Filtration efficiencies strongly depend on the aerosol velocity inside the filter media. At higher velocities, the retention or adhesion of particles is lowered. Smaller particles are easier to filter than larger sized particles. At a particle size of 5.0  $\mu\text{m}$ , elemental efficiency distributions of unity are present away from the edges of the filters where the velocities are lowest.

No visible differences are present between elemental efficiency distributions assuming perfect adhesion and non-perfect adhesion, for particles  $\leq 7.5 \mu\text{m}$ . Actual tabulations result in a maximum difference between elemental efficiencies assuming

perfect adhesion to elemental efficiencies assuming non-perfect adhesion of 0.7 percent difference.

For particle sizes  $\geq 5.0 \mu\text{m}$ , an increase in the overall filter efficiencies is achieved by obstructing the flow with a 76.2 mm diameter sphere. A maximum improvement of 2.6 percent in overall filter efficiency is achieved, at  $30 \mu\text{m}$  particles. For a filter of packing density  $c = 0.345$  and an effective fiber diameter of  $D_{ef} = 51.78 \mu\text{m}$ , at a monodisperse particle size of  $D_p \geq 15 \mu\text{m}$ , the overall filter efficiency assuming perfect adhesion reaches unity, regardless if flow is obstructed. At this large particle size, the Ptak and Jaroszczyk (1990) adhesion model strongly deviates from the assumed perfect adhesion calculations.

When perfect adhesion is assumed, the obstructed flows do not improve the overall filter efficiency for the SAE polydisperse test dust distributions. In fact, lower filter efficiencies are achieved. It is apparent from the figures that a smoother efficiency distribution is achieved with the unobstructed flow, for perfect adhesion. At the larger sized particles, the adhesion model is dominated by peak velocities resulting in lower adhesion efficiencies. The large particle sizes are perhaps too large for the adhesion model. It is recommended here that the Ptak and Jaroszczyk adhesion model be further investigated and implemented in efforts to determine an upper bound of particle size.

## CHAPTER VI

### SEPARATION AND CONTROL OF THE SAE PANEL FILTER TEST HOUSING

#### 6.1 Flow Uniformity in Automotive Air Filter Test Housings

By use of an ideal standard universal testing system ensuring uniform flow throughout a filter specimen, tested conditions could be controlled, and accurate comparison of performance characteristics between different filter designs may be made among different manufacturers and laboratories. With this in mind, the SAE J726 Test Code was developed (SAE, 1987a). The air cleaner test code provides a uniform method of determining and reporting air cleaner performance characteristics on the specified laboratory testing set-up and equipment. A schematic of the air filter element test set-up is illustrated in Figure 1.1. A detailed drawing of the panel filter universal test housing is illustrated in Figure 1.2.

Since filtration is a velocity dependent process, it is expected that the most efficient filtration is obtained when the incoming flow is distributed uniformly over the filter surface. However, an ideal universal testing system ensuring uniform flow is not completely achievable. At best, a testing system may be used to rank filters rather than to measure or predict actual filter performance (Jaroszczyk et al., 1987). A badly designed test system may result in the air flow upstream of the filter being channeled through the central region. The effects of non-uniform flow are shown in Figure 6.1 using monodisperse 5  $\mu\text{m}$  particles through a porous foam filter tested in layers (Brown, 1993). Channeling has caused the filter to remove aerosol over a more limited area and therefore at higher velocities. Thus, the graph of (logarithmic)

penetration against (linear) thickness does not reveal a penetration of unity, as illustrated in Figure 6.1. Essentially for a linear relationship, at a "zero" or no layer a filter penetration of 1.0 is expected.

Past and present work has shown that air filters tested in the universal SAE test housing experience very non-uniform flow. The abruptly expanding test housing inlet (without room for proper diffusing) results in flow separation. This separated flow provides non-uniform flow to the filter specimen. Within the following sub-section, it will be shown that the universal SAE test housing inlet is configured as a wide angle diffuser with no provisions to control flow separation.

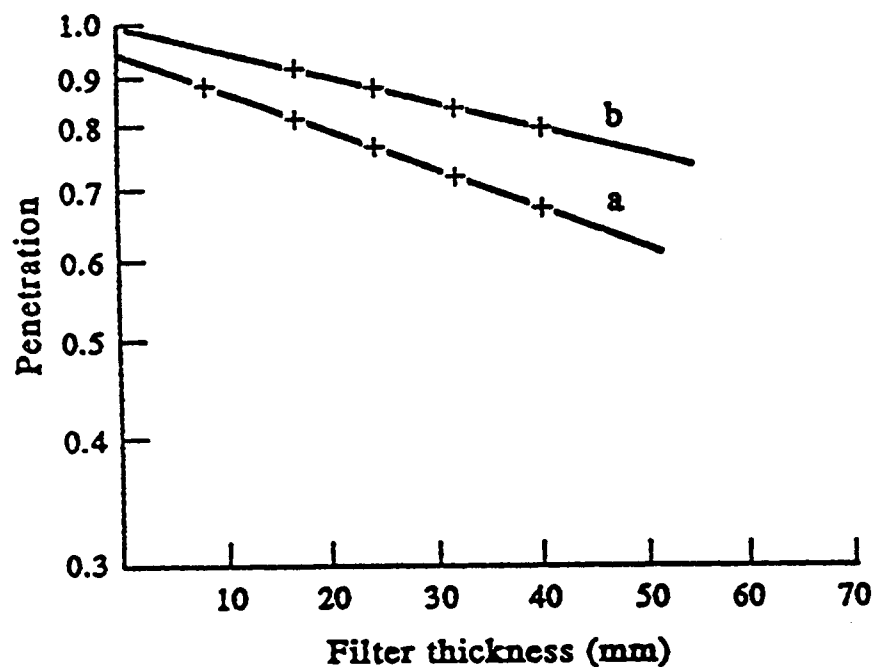


Figure 6.1 Effect of Non-Uniform Flow through a Porous Foam Filter Tested in Layers: (a) Non-Uniform Flow and (b) Uniform Flow (Brown, 1993)

## 6.2 Diffuser Performance and Characteristics

A diffuser is an expansion or area increase intended to reduce velocity in order to recover the pressure head of the flow. Diffusers are always designed to increase pressure and reduce kinetic energy of ducted flows. Small changes in design parameters cause large changes in performance (White, 1979). For two-dimensional straight-walled diffusers or flat walled diffusers, the two most important governing parameters for flow separations are total divergence angle,  $2\theta$  and the ratio of wall length to inlet throat width,  $L/w$ , (Chang, 1970). A typical flat walled diffuser with governing parameters labeled is illustrated in Figure 6.2. Chang's schematic diagrams of the flow regimes for two-dimensional diffusers are provided in Figure 6.3 and a flow regime map from White (1979) is presented in Figure 6.4. As referenced by Chang, these observations were originally made by S.J. Kline in 1958. A complete stability map of diffuser flow patterns was summarized and published in Fox and Kline (1962).

As shown in Figure 6.3 and 6.4, four entirely different flow regimes were observed as the total divergence angle,  $2\theta$ , was increased from  $0^\circ$  to  $100^\circ$ . Below the line *aa* in Figure 6.4, no region of stall exists and main flow is well behaved and unseparated as illustrated in Figure 6.3a. This no stall well-behaved flow pattern is most favorable for filtration testing. Between lines *aa* and *bb*, a large transitory stall exists in which the separation varies in location, size and intensity as illustrated in Figure 6.3b. Between lines *bb* and *cc*, a region of (bistable) fully developed stall exists in which the diffuser is filled with a large turbulent recirculation area as illustrated in Figure 6.3c. This bistable stall pattern may flip-flop from one wall to the other and diffuser performance is poor. Above line *cc*, a jet flow region exists in which the main

flow ignores the walls and simply passes on through at nearly constant area. Separation starts immediately downstream of the inlet throat. This type of flow occurs at high angles of divergence and diffuser performance is extremely poor.

The total divergence angles between diffuser planes may be determined as follows:

$$2\theta = 2 \tan^{-1} \left[ \frac{\frac{1}{2}(w_2 - w_1)}{L} \right] \quad (6.1)$$

The SAE test housing diverges in two angles. Using the actual dimensions of the SAE test housing as illustrated in Figure 1.2, the two total divergence angles between the diffuser planes are  $2\theta_A = 59.4^\circ$  and  $2\theta_B = 36.7^\circ$  with a  $L/w_1$  ratio of 2.78. For the case of  $2\theta_A$ , the flow could be interpreted as being in the region of jet flow. For the case of  $2\theta_B$ , the flow could be interpreted as being in the region of transitory stall. However, the flow regimes presented in Figures 6.3 and 6.4 apply only to two-dimensional flat wall diffusers. In reality, the universal SAE test housing diverges in two planes and will tend to behave like a flat walled diffuser with a greater divergence angle.

In efforts to provide a more realistic way of comparing a two plane diverging diffuser to flat walled diffuser flow regimes, it is proposed here to analyze the two plane diverging diffuser as a flat walled diffuser based on an equivalent area change. By dividing both the numerator and denominator of Equation (6.1) by  $w_1$  and expressing the ratio  $w_2/w_1$  as an area ratio  $A_2/A_1$ , Equation (6.1) may be expressed in terms of an area ratio as follows:

$$2\theta_{AB} = 2 \tan^{-1} \left[ \frac{\frac{1}{2} \left( \frac{A_2}{A_1} - 1 \right)}{L/w_1} \right] \quad (6.2)$$

Where  $A_1 = w_1 w_1$ ,  $A_2 = w_{2A} w_{2B}$ , and  $2\theta_{AB}$  is the equivalent divergence angle. For the SAE test housing, using Equation (6.2) we have  $2\theta_{AB} = 125.8^\circ$  and  $L/w_1 = 2.78$ , which corresponds to a jet flow regime as illustrated in Figures 6.3a and 6.4. Flow visualizations and velocity measurements presented within this thesis confirm the strongly recirculating separated flow at the walls of the housing and that the flow upstream of the filter is channelled through the central region resembling jet flow, as illustrated in Figure 6.3a. The geometry of the SAE test housing clearly leads to separated flow and poorly controlled filter inlet flow distributions.

Note that the diffuser performance and characteristics presented in this section apply to standard diffusers with an open exit. Unlike a standard diffuser with an open exit, the mounted filter within the SAE test housing provides some adverse or favorable pressure gradient. Based on flow visualizations and LDV measurements, this pressure gradient is favorable and provides back pressure which helps the flow behavior. Thus, flow regimes predicted from Figure 6.4 are achieved at slightly lower divergence angles.



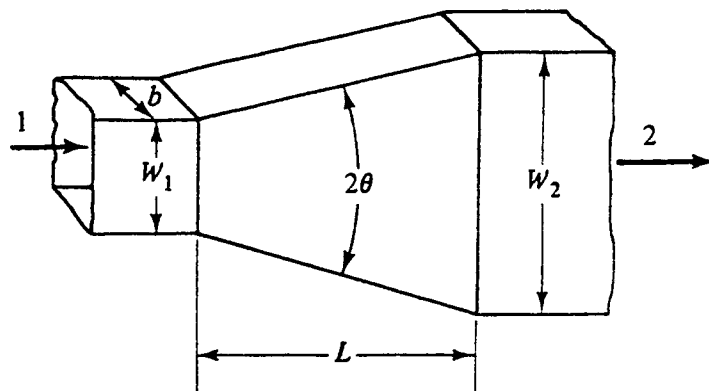


Figure 6.2 Diffuser Geometry of a Flat Walled Diffuser (White, 1979)

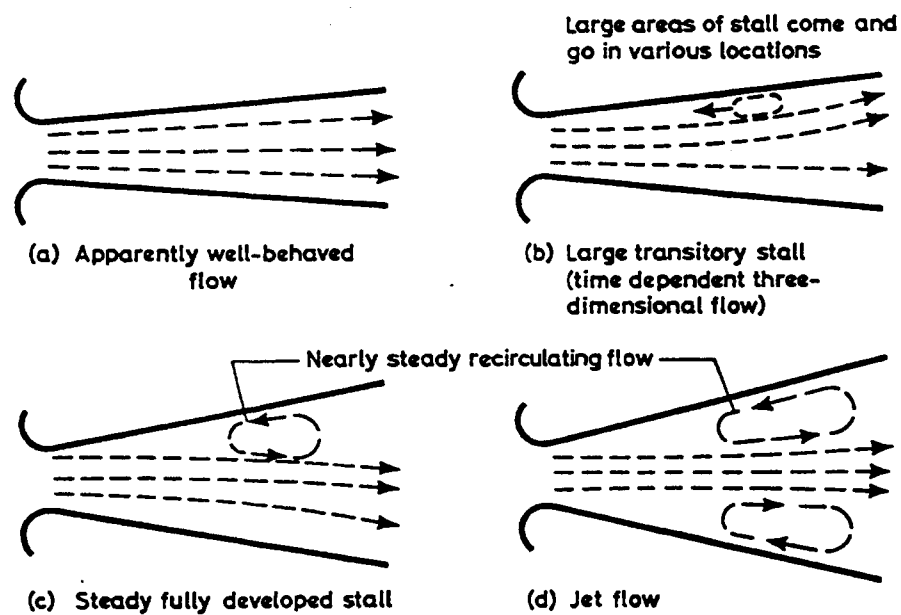


Figure 6.3 Schematic of Flat Walled Diffuser Operating Flow Regimes (Chang, 1970)

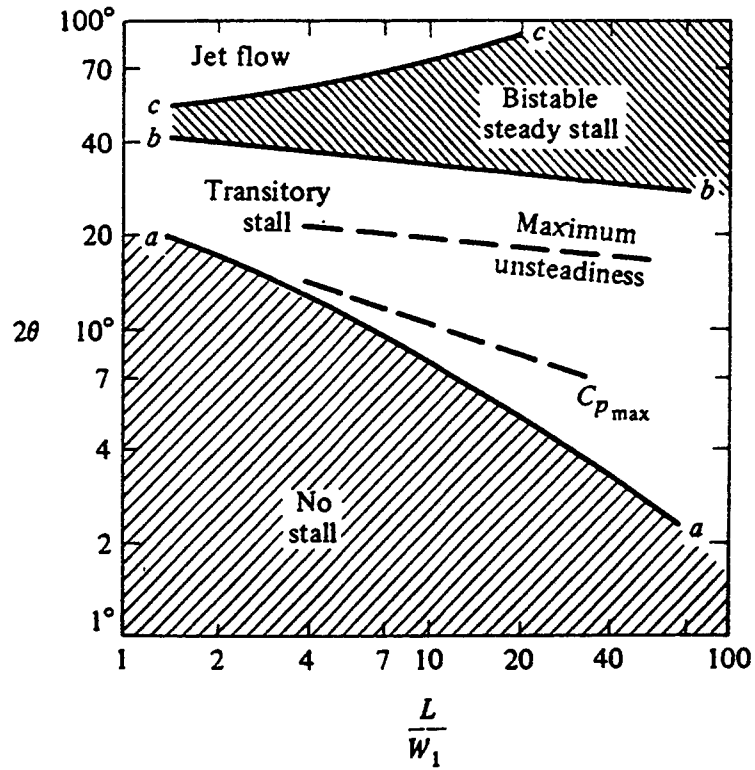


Figure 6.4 Flat Walled Diffuser Operating Flow Regime Map (White, 1979)

### 6.3 Recommended Test Housing Designs

A prototype shallow angle diffuser type panel filter test housing shown in Figure 6.5 was built (Liang et al., 1994; and Newman, 1994) to provide a more uniform flow to the filter being tested. This housing was specifically built for the Purolator AF3192 panel air filter element. Flow separation from the walls of the housing was not expected due to the very shallow angles of the diffuser section,  $2.8^\circ$  and  $0.6^\circ$ . With a calculated equivalent flat walled diffuser divergence angle of  $10.6^\circ$  and a  $L/w_1$  ratio of 10.2, one may expect this prototype housing to operate in the no stall or transitory stall regimes. However, unlike a standard diffuser with an open exit, the mounted filter within the test housing provides some back pressure which is understood to help the flow behavior. Thus based on flow visualizations and LDV measurements, flow regimes predicted from Figure 6.4 are achieved at slightly lower divergence angles. Flow visualizations and LDV velocity measurements presented by Newman (1994) show that the housing provides a much more uniform velocity distribution, resembling a developed turbulent duct flow, to the filter under test. An example of this flow distribution is provided in Figure 6.6.

Unlike the configuration of the SAE test housing, the filter specimen occupies the entire cross section of the prototype test housing. There are no zones of recirculation apparent in the prototype housing and the jet-like flow seen in the SAE test housing is not present. Much more uniform flows are achieved with this prototype shallow angle test housing. The disadvantage is having to custom fit the housing to the filter dimensions. Many different sized filters must be tested, thus it is not practical to custom fit a test housing design to each filter.

Unlike the prototype housing, the SAE test housing has a sudden contraction at the diffuser exit due to the filter mounting plate. It is understood that this mounting plate induces a region of recirculation between the sides of the filter and the housing walls. This mounting plate is the main mechanism allowing different sized filters to be tested within the same universal test housing. Changes in separation between different filter sizes may range from impinging jet flow with large regions of recirculation between the sides of the filter and housing walls, for small filters, to impinging flow with regions of separation near the housing walls upstream of the filter, for large filters. In summary, it is understood that changes in the filter size may change the operating regime of the diffuser.

To best control or minimize separation and achieve a much more uniform flow within a diffuser test housing, the divergence angle and the length to inlet throat ratio must be determined within the no stall regime of Figure 6.4. Furthermore, induced regions of recirculation due to the filter mounting plate may be minimized by reducing the range of filter sizes tested. It is recommended here that two to four new test housings (based on the range of panel filter sizes) be designed for a smaller range of panel filter sizes. By designing several test housings, a small filter mounting plate may be used reducing the sudden contraction area inducing recirculation near the filter and housing walls, and with a smaller diffuser exit area, a short diffuser length would be needed to achieve the smaller divergence angles. At present, in cooperation with Purolator Products Inc., these new prototype test housing designs will be directed towards the filter sizes most in demand.

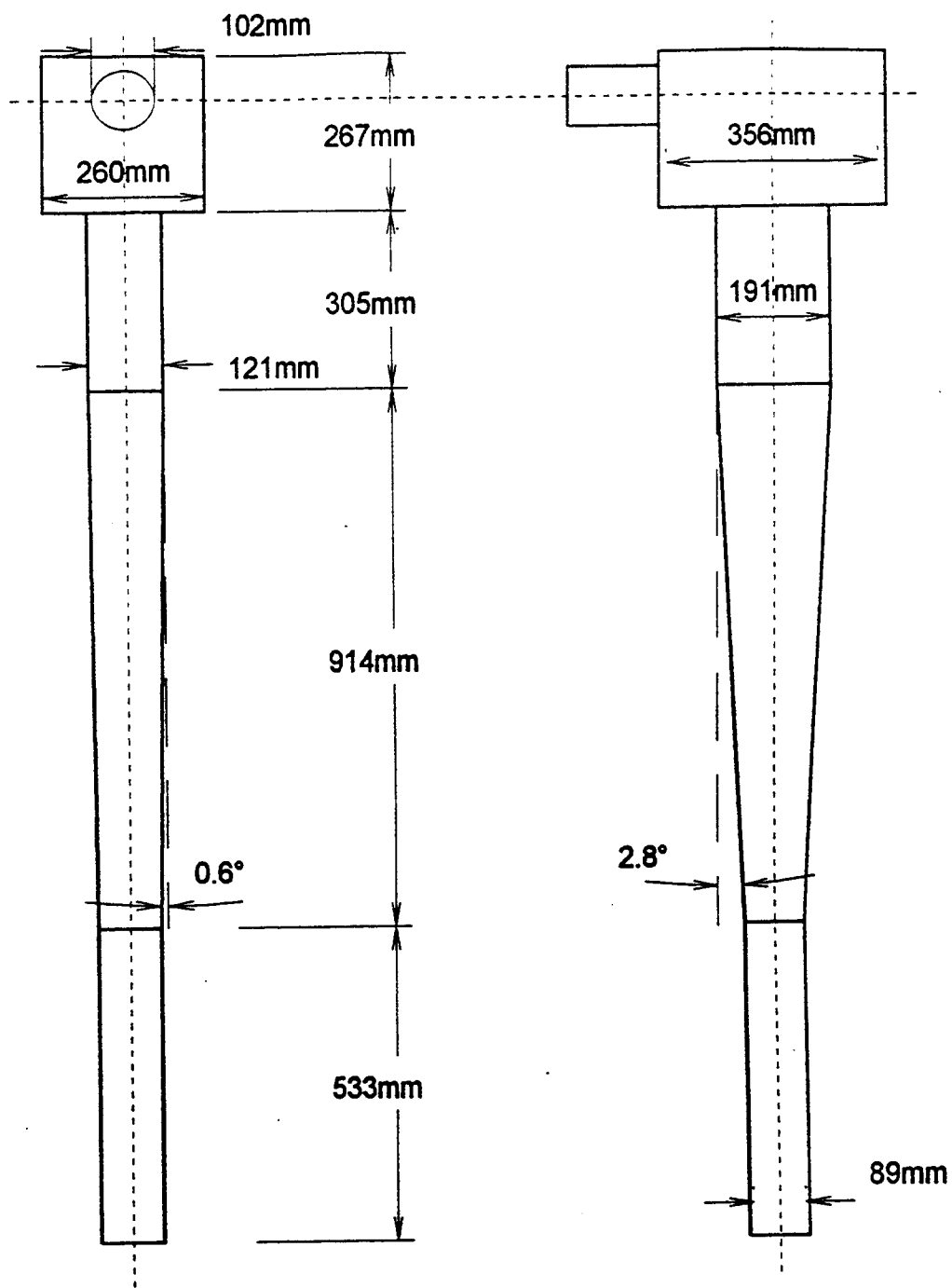


Figure 6.5 Shallow Angle Prototype Panel Filter Test Housing

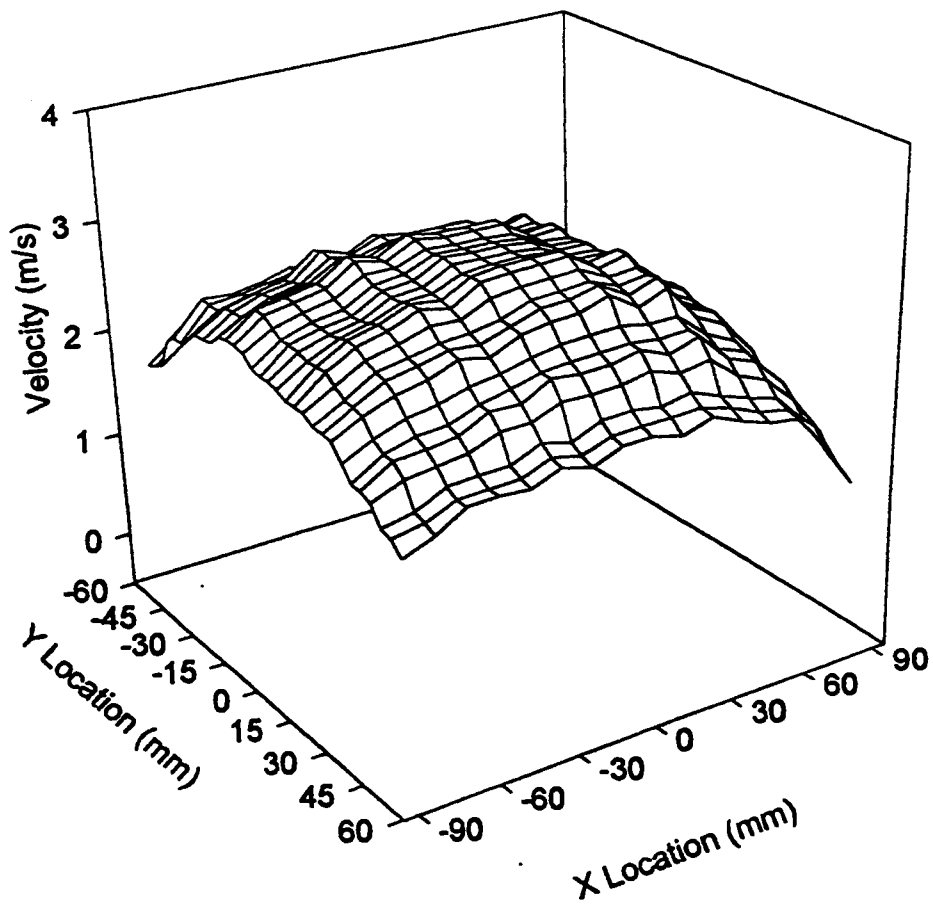


Figure 6.6 Velocity Distribution 13 mm Upstream of Filter in Prototype Test Housing (Newman, 1994)

## CHAPTER VII

### CONCLUSIONS AND RECOMMENDATIONS

#### 7.1 Conclusions

The following conclusions can be drawn from the work presented:

1. The flow field inside the standard SAE test housing is channelled through the central region with separated and recirculating regions along the walls of the housing.
2. The impinging jet like flow provides the filter with a bell-shaped non-uniform velocity distribution. Variations in velocity distributions can result in similar variations in efficiency distributions.
3. Obstructing spheres positioned at the housing inlet allow the inlet flow to be re-distributed away from the central inlet region. However, due to high inlet velocities restricting a sphere's wake region, the flow is re-channelled back to the central region.
4. Larger sized spheres positioned downstream of the inlet appear to be most effective in reducing the axial flow in the central region, resulting in moderately improved flow uniformity. Comparison of equally sized regions reveals lower flow rates within the central region of 11.8 and 18.6 percent. Overall, lower

fluctuations in regional flow rates were observed.

5. Particle collection efficiencies are strongly dependent upon both aerosol velocity and particle size. At larger particle sizes or smaller fiber diameters, efficiency curves approach peaks and end bounds at lower velocities.
6. No visible differences ( $< 0.7$  percent) are present between elemental efficiency distributions assuming perfect adhesion and non-perfect adhesion, for particles of  $D_p \leq 7.5 \mu\text{m}$ . For larger particles, the Ptak and Jaroszczyk (1990) adhesion model strongly deviates from the perfect adhesion efficiencies.
7. For a filter of packing density  $c = 0.345$ , and effective fiber diameter of  $D_{ef} = 51.78 \mu\text{m}$ , at a monodisperse particle size of  $D_p \geq 15.0 \mu\text{m}$ , the overall filter efficiency assuming perfect adhesion reaches unity.
8. Although the obstructed flow improves uniformity, no improvement in the overall filter efficiency for the two grades of SAE polydisperse test dust distributions is present, assuming perfect adhesion.
9. To best control or minimize separation and achieve a much more uniform flow within a diffuser test housing, the divergence angle and the length to inlet throat ratio must ensure a no stall regime.



## 7.2 Recommendations

The following is a listing of recommendations for future studies:

1. The Ptak and Jaroszczyk (1990) adhesion model can be further investigated and implemented in efforts to determine an upper bound particle size.
2. Velocity bias corrections could be investigated and implemented, if velocity bias errors are determined to be large. Possible on/off line corrections for probe volume displacement and/or distortion could be further investigated and implemented.
3. Several new test housings could be designed for a smaller range of panel air filters sizes. A small filter mounting plate may be used, reducing the sudden contraction area inducing recirculation near the filter and housing walls.
4. Efficiency models could be developed that include the effects of dust loading providing an overall filtration efficiency over the life of the filter.

## REFERENCES

- Aerometrics Inc., "User's Manual: Doppler Signal Analyzer for Phase Doppler Particle Sizing Applications," Draft 2, Aerometrics Inc., Sunnyvale, CA, 1992.
- Aerometrics Inc., "User's Manual: Doppler Signal Analyzer for Phase Doppler Particle Sizing Applications," Updated Revisions, Aerometrics Inc., Sunnyvale, CA, April 1993.
- Brinkman, H.C., "A Calculation of the Viscous Force Exerted by a Flowing Fluid on a Dense Swarm of Particles," *Applied Science Research*, Vol. A1, No. 27, 1967, pp. 27-34.
- Brown, R.C., *Air Filtration: An Integrated Approach to the Theory and Applications of Fibrous Filters*, Pergamon Press, Oxford, 1993.
- Cai, Q., "A Study of Air Filter Flow by Computational Fluid Dynamics," M.S. Thesis, Oklahoma State University, Stillwater, OK, 1993.
- Chang, P.K., *Separation of Flow*, Pergamon Press, New York, 1970.
- Chen, D.R., Pui, D.Y.H., and Liu, B.Y.H., "Optimization of Pleated Filter Design," *Air Filtration: Basic Technologies and Future Trends*, Proceedings of the American Filtration Society, 1994, pp. 24-32.
- Cooper, C.D., and Alley, F.C., *Air Pollution Control*, 2nd ed. Waveland Press, Prospect Heights, IL, 1994.
- Crawford, M., *Air Pollution Control Theory*, McGraw Hill, New York, NY, 1976.
- Dahneke, B., "The Capture of Aerosol Particles by Surfaces", *Journal of Colloid and Interface Science*, Vol. 37, No. 2, Academic Press, New York, 1971, pp. 342-353.
- Dahneke, B., "Measurements of Bouncing of Small Latex Spheres", *Journal of Colloid and Interface Science*, Vol. 45, No. 3, Academic Press, New York, 1973, pp. 584-590.
- Dahneke, B., "Further Measurements of the Bouncing of Small Latex Spheres", *Journal of Colloid and Interface Science*, Vol. 51, No. 1, Academic Press, New York, 1974, pp. 58-65

- Davies, C.N., *Air Filtration*, Academic Press, New York, NY, 1973.
- Dorman, R.G., "Filtration," *Aerosol Science*, edited by Davies, C.N., Academic Press, New York, 1966, pp.195-222.
- First, M.W., and Hinds, W.C., "High Velocity Filtration of Submicron Aerosols," *Journal of the Air Pollution Control Association*, Vol. 26, No. 2, APAC, 1976.
- Flagan, R.C., and Seinfeld, J.H., *Fundamentals of Air Pollution Engineering*, Prentice Hall Englewood, NJ, 1988.
- Freshwater, D.C., and Stenhouse, J.I.T., "The Retention of Large Particles in Fibrous Filters," *American Institute of Chemical Engineering Journal*, Vol. 18, No. 4, New York, NY, 1972, pp. 786-791.
- Fox, R.W., and Kline, S.J., "Flow Regimes in Curved Subsonic Diffusers," *Journal of Basic Engineering*, Vol. 84, ASME, New York, NY, 1962, pp. 303-316.
- Gillespie, T., "The Role of Electric Forces in the Filtration of Aerosols by Fiber Filters" *Journal of Colloid Science*, Vol. 10, Academic Press, New York, NY, 1955, pp. 299-314.
- Hall, M.J. and Hiatt, J.P., "Exit Flows from Highly Porous Media," *Physics of Fluids*, Vol. 6, No. 2, American Institute of Physics, 1994, pp. 469-479.
- Happel, J., "Viscous Flow Relative to Arrays of Cylinders," *American Institute of Chemical Engineers Journal*, Vol. 5, New York, NY, 1959, pp. 174-177.
- Hiatt, J.P., "Measurements of Velocities and Turbulence Intensities Created by Porous Ceramic Foams," M.S. Thesis, The University of Texas, Austin, TX, 1994.
- Jackson, G.W., and James, D.F., "The Permeability of Fibrous Porous Media," *The Canadian Journal of Chemical Engineering*, Vol. 64, CJCE, 1986, pp. 364-374.
- Jaroszcyk, T., and Verdegan, B.M., "Cartridge Filtration," *Filtration: Principles and Practices*, edited by Matteson, M.J. and Orr, C., Mercel Dekker, Inc., New York, 1987, pp. 537-606.
- Jaroszcyk, T., and Wake, J., "Critical Aerosol Velocity in Nonwoven Filtration," *TAPPI Proceedings*, Nonwoven Conference, Atlanta, GA, 1991, pp. 125-135.

- Krupp, H., "Particle Adhesion: Theory and Experiment," *Advances in Colloid and Interface Science*, Vol. 1, Elsevier Scientific Publishing Co., Amsterdam, 1967, pp. 111-239.
- Kuwabara, S., "The Forces Experienced by Randomly Distributed Parallel Circular Cylinders or Spheres in a Viscous Flow at Small Reynolds Numbers," *Journal of the Physical Society of Japan*, Vol. 14, Japan, 1959, pp. 527-532.
- Larsen, R.I., "The Adhesion and Removal of Particles Attached to Air Filter Surfaces," *American Industrial Hygiene Association*, Vol. 1, Williams & Wilkins Co., Baltimore, MD, 1958, pp. 265-270.
- Landahl, H.D., and Herrmann, R.G., "Sampling of Liquid Aerosols by Wires, Cylinders, and Slides, and the Efficiency of Impaction of the Droplet," *Journal of Colloid Science*, 1949, pp. 103-136.
- Lee, K.W. and Liu, B.Y.H., "Experimental Study of Aerosol Filtration by Fibrous Filters," *Aerosol Science and Technology*, Vol. 1, Elsevier Science Publishing Co., Amsterdam, 1982a, pp. 35-46.
- Lee, K.W. and Liu, B.Y.H., "Theoretical Study of Aerosol Filtration by Fibrous Filters", *Aerosol Science and Technology*, Vol. 1, Elsevier Science Publishing Co., Amsterdam, 1982b, pp. 147-161.
- Liang, F., Natarajan, B., Tian, Y., and Dougherty, R.L., "Local Efficiency Measurements Applicable to Both Automotive Engine and Cabin Filtration," *Particulate Science and Technology*, Vol. 12, No. 4, Taylor and Francis Publishers, 1994, pp. 333-350.
- Licht, W., *Air Pollution Control Engineering: Basic Calculations for Particulate Collection*, Pollution Engineering and Technology, Ref. Book 10, Marcel Dekker, New York, NY, 1980.
- Liu, G., Tebbutt, C.B., Duran, R., and Chambers, F.W., "Filter Inlet Velocity Redistribution with Filter Loading," *Advances in Filtration and Separation Technology*, Proceedings of the 1995 Annual Technical Conference of the American Filtration and Separations Society, Vol. 9, 1995, pp. 159-163.
- Löffler, F., "Investigation of Adhesive Forces Between Solid Particles and Fiber Surfaces," *Staub-Reinhaltung der Luft*, Vol. 26, No. 7, 1966, pp. 10-17.

- Loffler, F., "The Adhesion of Dust Particles to Fibrous and Particulate Surfaces," *Staub-Reinhaltung der Luft*, Vol. 28, No. 11, 1968, pp. 29-37.
- Loffler, F., and Umhauer, H., "An Optical Method for the Determination Of Particle Separation on Filter Fibers," *Staub-Reinhaltung der Luft*, Vol. 31, No. 2, 1971a, pp. 9-14.
- Loffler, F., "Collection of Particles by Fiber Filters," *Air Pollution Control*, edited by Stauss, W., John Wiley & Sons, New York, NY, 1971b.
- McQuiston, F.C., and Parker, J.D., *Heating, Ventilation, and Air Conditioning Analysis and Design*, 4th ed., John Wiley & Sons, New York, NY, 1994, pp. 103-125.
- Newman, R.A., "Uniformity of Airflow in Automotive Air Filter Test Housings and Its Effects on the Efficiency of Fibrous Filters," M.S. Thesis, Oklahoma State University, Stillwater, OK, 1994.
- Ptak, T., and Jaroszczyk, T., "Theoretical-Experimental Aerosol Filtration Model for Fibrous Filters at Intermediate Reynolds Numbers," *Proceedings of the Fifth World Filtration Congress*, France, 1990, pp. 566-572.
- SAE, "Air Cleaner Test Code - J726", Society of Automotive Engineers Recommended Practice, Warrendale, PA, June 1987a.
- SAE, "Air Cleaner Elements - J1141", Society of Automotive Engineers Information Report, Warrendale, PA, July 1987b.
- SAE, "Passenger Compartment Air Filter Test Code - J1669", Society of Automotive Engineers Recommended Practice, Warrendale, PA, December 1993.
- Sabnis, R.D., "Effects of Non-uniform Air Flow Through Filters on Filtration Efficiency," M.S. Thesis, Oklahoma State University, Stillwater, OK, 1993.
- Sabnis, R.D., Cai, Q., and Chambers, F.W., "Diagnosis of the Flow Fields in a Housing for Air Filter Performance Testing," *American Insititute of Aeronautics and Astronautics*, Paper AIAA 91-0117, 1994a.
- Sabnis, R.D., Cai, Q., and Chambers, F.W., "Flow Distribution Effects Upon Air Filter Performance Measurements," *Climate Control and Automotive Cabin Air Filtration*, Society of Automotive Engineers SP-1040 (Also available as SAE Paper 940317), 1994a, pp. 1-12.

- Suneja, S.K., and Lee, C.H., "Aersol Filtration by Fibrous Filters at Intermediate Reynolds Numbers ( $\leq 100$ )," *Atmospheric Environment*, Vol. 8, 1974, pp. 1081-1094.
- Spielman, L. and Goren, S.L., "Model for Predicting Pressure Drop and Filtration Efficiency in Fibrous Media," *Environmental Science and Technology*, Vol. 2, No. 4, 1968, pp. 279-287.
- Stenhouse, J.I.T., "Filtration of Air by Fibrous Filters," *Filtration and Separation*, Vol. 12, 1975, pp. 268-274.
- Tebbutt, C., "CFD Model of Flow Through Air Filters," M.S. Thesis, Oklahoma State University, Stillwater, OK, 1995
- Walkenhorst, W., "On the Effect of the Adhesive Force on the Separation Efficiency of Dust Filters" *Staub-Reinhaltung der Luft*, Vol. 32, No. 6, 1972, pp. 30-35.
- Wang, H.C., and Kasper, G., "Filtration Efficiency of Nanometer-Size Aerosol Particles," *Journal of Aerosol Science*, Vol. 22, No. 1, Pergamon Press, 1991, pp. 31-41.
- Wang, Y., "Effect of Component Layout and Geometry for Surface Mounted Electronic Components: A Smoke Flow Visualization Study," M.S. Thesis, Oklahoma State University, Stillwater, OK, 1993, pp. 11-24.
- White, F.M., *Fluid Mechanics*, McGraw Hill, New York, NY, 1979.

**APPENDIX A**  
**PUROLATOR AF3192 FILTER SPECIFICATIONS**

Table A.1 Filter Specifications

Description	Specification
Length of filter (mm)	193
Width of filter (mm)	121
Height of pleats (mm)	30
Pitch of pleats (mm)	3.125
Filter media thickness ( $\mu\text{m}$ )	700
Effective fiber diameter ( $\mu\text{m}$ )	51.78
Packing Density	0.345





C ERI REAL VECT SINGLE EFF DUE TO INTERCEPT + INERTIAL  
 C ERIA REAL VECT SINGLE EFF DUE TO INTERCEPT + INTERITAL W/ ADH  
 C EELM REAL VECT ELEMENTAL EFFICIENCY  
 C ELMA REAL VECT ELEMENTAL EFFICEINCY WITH ADHESION EFF  
 C PE REAL VECTOR PENETRATION DUE TO INERTIAL INTERCEPTION ONLY  
 C PEA REAL VECTOR PENETRATION DUE TO INERTIAL INTERCEPTION  
 C AND ADHESION  
 C EOY REAL OVERALL EFFICIENCY  
 C EOVA REAL OVERALL EFFICEINCY WITH ADHESION EFFECTS

C PARAMETERS AND VARIABLES:

C C REAL PACKING DENSITY OF FILTER MEDIA  
 C HF REAL HIEGHT OF FILTER PLEATS, FILTER DEPTH [M]  
 C PF REAL PITCH OF FILTER [M]  
 C UIF REAL VECTOR VELOCITY IN FILTER MEDIA  
 C AE REAL VECTOR ELEMENTAL AREA PER UPSTREAM OF FILTER  
 C SAE REAL VECTOR ELEMENTAL SURFACE AREA THROUGH FILTER  
 C AFILT REAL TOTAL FILTER AREA  
 C DX REAL VECTOR TRAVERSE INCREMENT IN X-AXIS  
 C DY REAL VECTOR TRAVERSE INCREMENT IN Y-AXIS  
 C ST REAL VECTOR STOKES NUMBER  
 C STC REAL VECTOR STOKES NUMBER CORRECTED FOR SLIP  
 C RE REAL VECTOR REYNOLDS NUMBER

C DATA FILES:

C EFFVEL.DAT EXPERIMENTAL DATA ARRANGED IN ASCENDING ORDER (1-66)  
 C  
 C OUPUT FILES:  
 C VELSTRE.OUT RAW VEL, PLEAT VEL, STOKES #, AND REYNOLDS #  
 C  
 C EFFCOMP.OUT INTERCEPTION, INERTIAL IMPACTION, AND ADHESION EFF  
 C  
 C SINGELEM.OUT SINGLE AND ELEMENTAL EFFICIENCIES  
 C  
 C SAEDUST.OUT OVERALL EFFICIENCIES OF SAE TEST DUST DISTRIBUTION

C SUBROUTINES:

C EFFRIA IMPLEMENTS THREE MODELS TO CALCULATE INTERCEPTION,  
 C INERTIAL, AND ADHESION EFFICIENCIES  
 C SINGLEE CALCULATES THE SINGLE FIBER EFFICIENCY DUE TO INERTIAL  
 C IMPACTION AND INTERCEPTION, "COLLECTION OR COLLISION  
 C EFFICIENCY"; IN ADDITION, CALCUALTES THE SINGLE FIBER  
 C EFFICIENCY DUE TO INERTIAL INTERCEPTION ("COLL EFF")  
 C AND ADHESION.  
 C ELEMENT CALCUALTES ELEMENTAL FIBER EFFICIENCIES DUE TO  
 C INERTIAL INTERCEPTION AND INERTIAL INTERCEPTION WITH  
 C ADHESION.

C FUNCTIONS:

C -NONE USED-

```

C
C
C   PROGRAM EFFMODEL
C
C   PARAMETER (NDP=66)
C   PARAMETER (PP=9)
C   PARAMETER (PD=8)
C
C   REAL RN(NDP),VOF(NDP),UIF(NDP)
C   REAL ER(NDP),EI(NDP),EA(NDP),ST(NDP),STC(NDP),RE(NDP)
C   REAL ERI(NDP),ERIA(NDP)
C   REAL EELM(NDP),ELMA(NDP)
C   REAL PE(NDP),PEA(NDP),EOV,EOVA
C   REAL PARAM(PP),C,RP(PD),RF,RHOP,VISCA,H,HF,PF,LAM
C   REAL AE(NDP),SAE(NDP),DX(NDP),DY(NDP),AFILT
C   REAL RDUST(PD),MFDUST(PD),MCDUST(PD)
C   REAL*8 M(PD),MEFF1(NDP),MEFF2(NDP)
C   REAL DPE(NDP),DPEA(NDP),DEOV,DEOVA
C   REAL VOFM,UIFM,QCFM
C   REAL TRASH,NUM1,NUM2,DEN
C
C   INTEGER I,J,IJ,II,JJ,K,KDUST,NUMPD
C   INTEGER FLAG
C
C   CHARACTER*14 FLABEL
C   CHARACTER*12 DATAFILE,DTYPE
C   CHARACTER*5 ALPHA(PP)
C
C-->SAE STANDARD TEST DUST DISTRIBUTION DATA (%weight)
C
C   DATA RDUST /0.75,1.50,2.50,5.0,10.0,20.0,40.0,100.0/
C   DATA MFDUST /0.274,0.076,0.04,0.18,0.16,0.18,0.09,0.00/
C   DATA MCDUST /0.065,0.035,0.02,0.12,0.14,0.23,0.30,0.09/
C
C-->INITIALIZE PARAMETER [PARAM(2),RP:TO BE SPECIFIED LATER]
C
C   DATA ALPHA(1)/'C    '/
C   C=0.345
C   PARAM(1)=C
C   DATA ALPHA(2)/'RP   '/
C   RP(1)=0.000000
C   PARAM(2)=RP(1)
C   DATA ALPHA(3)/'RF   '/
C   RF=(51.78E-6)/2.0
C   PARAM(3)=RF
C   DATA ALPHA(4)/'RHOP '/
C   RHOP=2723.0
C   PARAM(4)=RHOP
C   DATA ALPHA(5)/'VISCA'/
C   VISCA=1.837E-5
C   PARAM(5)=VISCA
C   DATA ALPHA(6)/'HF   '/
C   HF=0.03
C   PARAM(6)=HF
C   DATA ALPHA(7)/'H    '/

```



```

DO 120 I=1,PD
  RP(I)=RDUST(I)/1000000
  M(I)=MCDUST(I)
  DTYPE=' SAE COURSE '
120  CONTINUE
  END IF
  IF(FLAG.EQ.3) THEN
    DTYPE='W/O SAE DUST'
    PRINT*, " INPUT THE PARTICLE RADIUS [MICRONS]"
    READ*,RP(1)
    RP(1)=RP(1)/1000000
  END IF
C
C-->OPEN DATA AND OUTPUT FILES
C
  OPEN(2,FILE=DATAFILE,STATUS="OLD")
  OPEN(6,FILE="VELSTRE.OUT")
  OPEN(7,FILE="EFFCOMP.OUT")
  OPEN(8,FILE="SINGELEM.OUT")
  OPEN(9,FILE="SAEDUST.OUT")
C
C-->READ INPUT DATA FILE
C  NOTE: INPUT FILE MUST HAVE A LABEL, DATE, OR NAME
C  ON THE FIRST LINE WITH NO MORE THAN 14 CHARATERS
C
  READ(2,4000) FLABEL
4000  FORMAT(A14)
  DO 200 I=1,NDP
    READ(2,*) RN(I),TRASH,VOF(I)
    c  VOF(I)--VOF(I)
200  CONTINUE
C
C-->SPECIFY ELEMENTAL AREA PER SPECIFIC DATA POINT
C
  DO 300 IJ=1,NDP
    DX(IJ)=0.75*0.0254
    DY(IJ)=0.50*0.0254
    IF(IJ.EQ.1.OR.IJ.EQ.11) THEN
      DX(IJ)=0.5*DX(IJ)
      DY(IJ)=0.5*DY(IJ)
    END IF
    IF(IJ.GE.2.AND.IJ.LE.10) DX(IJ)=0.50*DX(IJ)
    IF(IJ.EQ.12.OR.IJ.EQ.22) DX(IJ)=0.50*DX(IJ)
    IF(IJ.EQ.23.OR.IJ.EQ.33) DX(IJ)=0.50*DX(IJ)
    IF(IJ.EQ.34.OR.IJ.EQ.44) DX(IJ)=0.50*DX(IJ)
    IF(IJ.EQ.45.OR.IJ.EQ.55) DX(IJ)=0.50*DX(IJ)
    IF(IJ.GE.57.AND.IJ.LE.65) DY(IJ)=0.25*DY(IJ)
    IF(IJ.EQ.56.OR.IJ.EQ.66) THEN
      DY(IJ)=0.25*DY(IJ)
      DX(IJ)=0.5*DX(IJ)
    END IF
    AE(IJ)=DX(IJ)*DY(IJ)
    SAE(IJ)=DX(IJ)*(((2.0*HF*DY(IJ)/PF)**2.0)+DY(IJ)**2)**0.5)
    UIF(IJ)=VOF(IJ)*AE(IJ)/((1.0-PARAM(1))*SAE(IJ))
300  CONTINUE

```

```

C
C-->TITLE LABELS FOR OUTPUT FILES
C
      WRITE(6,4501) DTYPE
      WRITE(7,4502) DTYPE
      WRITE(8,4503) DTYPE
      IF(FLAG.NE.3) WRITE(9,4504) DTYPE
4501  FORMAT(//,T36,'VELSTRE.OUT',/,T30,'OUTPUT FROM EFFMODEL.FOR',
      +/,T36,A12)
4502  FORMAT(//,T36,'EFFCOMP.OUT',/,T30,'OUTPUT FROM EFFMODEL.FOR',
      +/,T36,A12)
4503  FORMAT(//,T36,'SINGELEM.OUT',/,T30,'OUTPUT FROM EFFMODEL.FOR',
      +/,T36,A12)
4504  FORMAT(//,T36,'SAEDUST.OUT',/,T30,'OUTPUT FROM EFFMODEL.FOR',
      +/,T36,A12)
C
C-->MAIN DO LOOP FOR SAE DISTRIBUTION
C
      NUNPD=PD
      IF(FLAG.EQ.3) NUNPD=1
      DO 205 K=1,NDP
          MEFF1(K)=0.0
          MEFF2(K)=0.0
205   CONTINUE
      DO 350 KDUST=1,NUNPD
          PARAM(2)=RP(KDUST)
C
C-->CALL SUBROUTINES
C
      DO 400 J=1,NDP
          CALL EFFRIA(PARAM,UIF(J),ER(J),EI(J),EA(J),ST(J),STC(J),RE(J))
          CALL SINGLEE(PARAM,ER(J),EI(J),EA(J),ERI(J),ERIA(J))
          CALL ELEMENT(PARAM,ERI(J),ERIA(J),EELM(J),ELMA(J))
400   CONTINUE
C
C-->PENETRATION
C
      DO 500 II=1,NDP
          PE(II)=1.0-EELM(II)
          PEA(II)=1.0-ELMA(II)
500   CONTINUE
C
C-->OVERALL FILTER EFFICIENCY
C
      NUM1=0.0
      NUM2=0.0
      DEN=0.0
      AFILT=0.0
      VOFM=0.0
      UIFM=0.0
      DO 600 JJ=1,NDP
          NUM1=NUM1+PE(JJ)*SAE(JJ)*UIF(JJ)
          NUM2=NUM2+PEA(JJ)*SAE(JJ)*UIF(JJ)
          DEN=DEN+SAE(JJ)*UIF(JJ)
          AFILT=AFILT+AE(JJ)

```

```

        VOFM=VOFM+VOF(JJ)
        UIFM=UIFM+UIF(JJ)
600    CONTINUE
        EOVM=1.0- NUM1/DEN
        EOVA=1.0- NUM2/DEN
        QCFM=DEN/0.000472
        VOFM=VOFM/FLOAT(NDP)
        UIFM=UIFM/FLOAT(NDP)
C
C--->SAE DISTRIBUTION CALCULATIONS
C
        IF(FLAG.EQ.3) GOTO 651
        DO 650 II=1,NDP
        MEFF1(II)=MEFF1(II)+(M(KDUST)*EELM(II))
        MEFF2(II)=MEFF2(II)+(M(KDUST)*ELMA(II))
650    CONTINUE
651    CONTINUE
C
C-->WRITE EFFICIENCIES TO OUTPUT FILES
C
        WRITE(6,5000) FLABEL
        WRITE(7,5000) FLABEL
        WRITE(8,5000) FLABEL
5000   FORMAT(/,2X,A14,/,2X,'PARAMETERS:')
        DO 1000 J=1,PP
        WRITE(6,5100) ALPHA(J),PARAM(J)
        WRITE(7,5100) ALPHA(J),PARAM(J)
        WRITE(8,5100) ALPHA(J),PARAM(J)
1000   CONTINUE
5100   FORMAT(T5,A5,'-',1X,E13.5)
        WRITE(6,6200)
6200   FORMAT(/,2X,'RUN',T12,'VEL UPSTRM',T27,'FILTER VEL',T43,'STOKES',
+T58,'CSTOKES',T73,'REYNOLDS',/)
        WRITE(7,7200)
7200   FORMAT(/,2X,'RUN',T13,'INTERCEPT',T28,'INERTIAL',T43,'ADHESIVE',/)
        WRITE(8,8200)
8200   FORMAT(/,2X,'RUN',T13,'SINGLE',T27,'SING w/ ADH',T43,'ELEMENTAL',
+T57,'ELEM w/ ADH',/)
        DO 1100 K=1,NDP
        WRITE(6,6300) K,VOF(K),UIF(K),ST(K),STC(K),RE(K)
        WRITE(7,7300) K,ER(K),EI(K),EA(K)
        WRITE(8,8300) K,ERI(K),ERIA(K),EELM(K),ELMA(K)
1100   CONTINUE
6300   FORMAT(2X,I3,T10,E12.5,T25,E12.5,T40,E12.5,T55,E12.5,T70,E12.5)
7300   FORMAT(2X,I3,T10,E12.5,T25,E12.5,T40,E12.5)
8300   FORMAT(2X,I3,T10,E12.5,T25,E12.5,T40,E12.5,T55,E12.5)
        WRITE(8,8400) EOVM,EOVA,QCFM,VOFM,UIFM
8400   FORMAT(/,2X,'OVERALL/TOTALS',/,T10,'EOV =',T18,E12.5,T40,
+'EOVA =',T48,E12.5,/,T10,'QCFM =',T18,E12.5,/,T10,'VOFM =',
+T18,E12.5,T40,'UIFM =',T48,E12.5)
C
C-->END OF MAIN DO LOOP
C
350   CONTINUE
C

```

```

C-->FOR FLAG = 3 SKIP SAE DUST DISTRIBUTION CALCULATIONS
C
      IF(FLAG.EQ.3) GOTO 999
C
C-->OVERALL SAE TEST DUST EFFICIENCIES
C
      DO 700 II=1,NDP
      DPE(II)=1.0-MEFF1(II)
      DPEA(II)=1.0-MEFF2(II)
700  CONTINUE
      NUM1=0.0
      NUM2=0.0
      DEN=0.0
      DO 750 JJ=1,NDP
      NUM1=NUM1+DPE(JJ)*SAE(JJ)*UIF(JJ)
      NUM2=NUM2+DPEA(JJ)*SAE(JJ)*UIF(JJ)
      DEN=DEN+SAE(JJ)*UIF(JJ)
750  CONTINUE
      DEOV=1.0-NUM1/DEN
      DEOVA=1.0-NUM2/DEN
C
C-->WRITE SAE TEST DUST DISTRIBUTION EFFICIENCIES
C
      WRITE(9,5000) FLABEL
      DO 800 JJ=1,PP
      IF(JJ.NE.2) WRITE(9,5100) ALPHA(JJ),PARAM(JJ)
      IF(JJ.EQ.2) WRITE(9,5101) ALPHA(JJ)
800  CONTINUE
5101 FORMAT(T5,A5,' =',1X,' SAE DUST')
      WRITE(9,9100)
9100 FORMAT(/,T5,'SAE TEST DUST DISTRIBUTION')
      WRITE(9,9201) (RP(IJ),IJ=1,PD)
      WRITE(9,9202) (M(IJ),IJ=1,PD)
9201 FORMAT(2X,'RADIUS: ',10(E12.5,2X),/)
9202 FORMAT(2X,'%WIEGHT: ',10(E12.5,2X),/)
      WRITE(9,9300)
9300 FORMAT(/,2X,'RUN',T11,'OV DUST EFF',T28,'OV W/ ADH',/)
      DO 850 K=1,NDP
      WRITE(9,9400) K,MEFF1(K),MEFF2(K)
850  CONTINUE
9400 FORMAT(2X,I3,T10,E12.5,T25,E12.5)
      WRITE(9,9500) DEOV,DEOVA
9500 FORMAT(/,2X,'OVERALL/TOTALS',/, 'DEOV =',T18,E12.5,T40,
+ 'DEOVA =',T48,E12.5)
C
C-->FOR FLAG = 3 SKIP SAE DUST CALCULATIONS
C
999  CONTINUE
C
C-->ECHO PRINT EFFMODEL COMPLETE
C
      PRINT*,' '
      PRINT*,' '
      PRINT*,' '
      PRINT*,' '

```





```

C
C   OUTPUT:
C   EINTER REAL   EFFICEINCY DUE TO INTERCEPTION
C   EINER  REAL   EFFICIENCY DUE TO INERTIAL IMPACTION
C   EADH   REAL   ADHESION EFFICIENCY
C   ST1    REAL   STOKES NUMBER
C   ST2    REAL   STOKES NUMBER CORRECTED FOR SLIP
C   REN    REAL   REYNOLDS NUMBER
C
C   SUBROUTINES:
C   - NONE USED -
C
C   FUNCTIONS:
C   - NONE USED -
C
C*****
C
C   SUBROUTINE EFFRIA(P,U,EINTER,EINER,EADH,ST1,ST2,REN)
C
C   REAL P(10),U,EINTER,EINER,EADH,ST1,ST2,REN
C   REAL C,RP,RF,RHOP,LAM,VISCA
C   REAL I,KN,KU,CC
C
C-->PARAMETERS
C
C   C=P(1)
C   RP=P(2)
C   RF=P(3)
C   RHOP=P(4)
C   VISCA=P(5)
C   LAM=P(9)
C
C   I=RP/RF
C   KN=LAM/RF
C   KU=(-0.5)*LOG(C)-0.75+C-(0.25)*C**2.0
C   CC=1.0+1.257*KN
C   FC=0.90/(C**0.30)
C
C-->STOKES, STOKES CORRECTED, REYNOLDS
C
C   ST1=(RP**2.0)*RHOP*U/(9.0*VISCA*RF)
C   ST2=ST1*CC
C   REN=RHOP*2.0*RP*U/VISCA
C
C
C-->EFFICIENCY DUE TO INTERCEPTION
C
C   EINTER=((1.0-C)*I**2.0)/(KU*(1.0+I))
C   IF(EINTER.GT.1.0) EINTER=1.00
C
C-->EFFICIENCY DUE TO INERTIAL IMPACTION
C
C   EINER=FC*(ST2**3.0)/((ST2**3.0)+(0.77*ST2**2.0)+0.22)
C   IF(EINER.GT.1.0) EINER=1.00
C

```

```

C-->ADHESION EFFICIENCY
C
      EADH=(190.0)/(((ST2*REN)**0.68)+190.0)
      IF(EADH.GT.1.0) EADH=1.00
C
C
C-->RETURN -N- END
C
      RETURN
C
      -N-
      END
C
C***** END OF SUBROUTINE ERIA *****
C
C
C-----
C***** SUBROUTINE SINGLEE *****
C
C  SUBROUTINE SINGLEE CALCULATES THE SINGLE FIBER EFFICIENCY
C  EFFICIENCY DUE TO INERTIAL IMPACTION AND INTERCEPTION.
C  THIS SUBROUTINE ALSO CALCULATES THE ADHESION EFFICIENCY.
C
C  CALL STATEMENT:
C    CALL SINGLEE(P,EINTER,EINER,EADH,EII,EIIA)
C
C  INPUT:
C    EINTER REAL  EFFICEINCY DUE TO INTERCEPTION
C    EINER  REAL  EFFICIENCY DUE TO INERTIAL IMPACTION
C    EADH   REAL  ADHESION EFFICIENCY
C
C  OUTPUT:
C    EII   REAL  SINGLE FIBER "COLLECTION/COLLISION" EFFICIENCY
C    EIIA  REAL  SINGLE FIBER EFFICIENCY (WITH ADHESION)
C
C  SUBROUTINES:
C    - NONE USED -
C
C  FUNCTIONS:
C    - NONE USED -
C
C*****
C
C    SUBROUTINE SINGLEE(P,EINTER,EINER,EADH,EII,EIIA)
C
C    REAL P(10),EINTER,EINER,EADH,EII,EIIA
C
C-->PARAMETERS (NOT USED)
C
C    C=P(1)
C
C-->SIGLE FIBER EFFICIENCY
C
C    EII=1.0-(1.0-EINTER)*(1.0-EINER)
C    EIIA=EII*EADH
C

```

```

C
C-->RETURN -N- END
C
C   RETURN
C   -N-
C   END
C
C***** END OF SUBROUTINE SINGLEE *****
C
C
C-----
C***** SUBROUTINE ELEMENT *****
C
C   SUBROUTINE ELEMENT CALCULATES THE ELEMENTAL FIBER EFFICIENCY
C   DUE TO INERTIAL IMPACTION AND INTERCEPTION WITH AND WITHOUT
C   THE ADHESION EFFICIENCY MODEL
C
C   CALL STATEMENT:
C   CALL ELEMENT(P,EII,EIIA,EELM1,EELM2)
C
C   INPUT:
C   P   REAL VECTOR PARAMETERS OF PARTICLE, FILTER, AIR
C   EII REAL   SINGLE FIBER "COLLECTION/COLLISION" EFFICIENCY
C   EIIA REAL  SINGLE FIBER EFFICIENCY (WITH ADHESION)
C
C   PARAMETERS AND VARIABLES:
C   P   REAL VECTOR PARAMETERS OF PARTICLE, FILTER, AIR
C   C   REAL   PACKING DENSITY
C   H   REAL   FILTER THICKNESS
C   RF  REAL   FILTER DIAMETER
C
C   OUTPUT:
C   EELM1 REAL  ELEMENTAL FIBER EFFICIENCY
C   EELM2 REAL  ELEMENTAL FIBER EFFICIENCY WITH ADHESION EFF
C
C   SUBROUTINES:
C   - NONE USED -
C
C   FUNCTIONS:
C   - NONE USED -
C
C*****
C
C
C   SUBROUTINE ELEMENT(P,EII,EIIA,EELM1,EELM2)
C
C   REAL P(10),EII,EIIA,EELM1,EELM2
C   REAL C,RF,H,PI
C
C-->PARAMETERS
C
C   C=P(1)
C   RF=P(3)
C   H=P(7)
C

```

```
      PI=3.141592654
C
C
C-->ELEMENTAL EFFICIENCIES
C
      EELM1=1.0-EXP((-EII*2.0*C*H)/(PI*(1.0-C)*RF))
      EELM2=1.0-EXP((-EIIA*2.0*C*H)/(PI*(1.0-C)*RF))
C
C
C-->RETURN -N- END
C
      RETURN
C      -N-
      END
C
C***** END OF SUBROUTINE ELEMENT *****
```

## APPENDIX C

## SAMPLE INPUT/OUTPUT FILES OF EFFMODEL.FOR

## C.1 Sample Input Data File

76Sphr159-F8	V1	V2
1.0000E+00	-2.4106E-01	-1.0030E+00
2.0000E+00	-1.4962E-01	-2.7023E+00
3.0000E+00	-9.6970E-01	-4.2231E+00
4.0000E+00	-5.1045E-01	-5.0692E+00
5.0000E+00	7.8243E-01	-4.7916E+00
6.0000E+00	4.3733E-01	-4.0803E+00
7.0000E+00	5.5236E-02	-4.2959E+00
8.0000E+00	7.0578E-01	-5.1099E+00
9.0000E+00	1.3280E+00	-4.6677E+00
1.0000E+01	8.7683E-01	-3.4447E+00
1.1000E+01	6.5273E-01	-2.0906E+00
1.2000E+01	-1.1217E+00	-1.4680E+00
1.3000E+01	-8.3179E-01	-2.9868E+00
1.4000E+01	-1.2413E+00	-4.4846E+00
1.5000E+01	-6.2008E-01	-5.3166E+00
1.6000E+01	7.7406E-01	-5.1225E+00
1.7000E+01	4.1842E-01	-4.1739E+00
1.8000E+01	1.5147E-01	-4.2078E+00
1.9000E+01	7.3775E-01	-4.7593E+00
2.0000E+01	1.2398E+00	-3.7634E+00
2.1000E+01	1.8862E-01	-2.7373E+00
2.2000E+01	-8.0497E-02	-1.7366E+00
2.3000E+01	-1.5138E+00	-1.7988E+00
2.4000E+01	-1.4949E+00	-3.0458E+00
2.5000E+01	-1.6532E+00	-4.7254E+00
2.6000E+01	-9.1782E-01	-5.6913E+00
2.7000E+01	3.9515E-01	-5.4293E+00
2.8000E+01	2.9540E-01	-4.4215E+00
2.9000E+01	5.2865E-01	-4.1698E+00
3.0000E+01	8.8168E-01	-4.0468E+00
3.1000E+01	5.9147E-01	-3.1551E+00
3.2000E+01	-2.0025E-01	-2.0762E+00
3.3000E+01	-8.2235E-01	-1.1833E+00
3.4000E+01	-2.2316E+00	-2.1049E+00
3.5000E+01	-1.9039E+00	-3.1820E+00
3.6000E+01	-1.8358E+00	-4.5698E+00
3.7000E+01	-9.4744E-01	-5.5708E+00
3.8000E+01	1.5867E-01	-5.0566E+00
3.9000E+01	3.1783E-01	-4.4364E+00
4.0000E+01	5.3088E-01	-3.9087E+00
4.1000E+01	8.8168E-01	-3.4390E+00
4.2000E+01	5.4293E-01	-2.3662E+00
4.3000E+01	-5.4711E-01	-1.5038E+00
4.4000E+01	-7.9857E-01	-9.8575E-01
4.5000E+01	-2.1836E+00	-2.1664E+00

4.6000E+01	-2.1777E+00	-2.9568E+00
4.7000E+01	-1.7769E+00	-4.1559E+00
4.8000E+01	-7.9213E-01	-4.8660E+00
4.9000E+01	-2.7748E-01	-4.7079E+00
5.0000E+01	2.7380E-01	-3.8797E+00
5.1000E+01	3.2017E-01	-3.3604E+00
5.2000E+01	5.2586E-01	-2.8595E+00
5.3000E+01	2.0737E-01	-1.7114E+00
5.4000E+01	-8.2046E-01	-9.4449E-01
5.5000E+01	-1.0092E+00	-5.7282E-01
5.6000E+01	-1.9588E+00	-2.3704E+00
5.7000E+01	-1.6879E+00	-3.0091E+00
5.8000E+01	-1.3930E+00	-4.1471E+00
5.9000E+01	-6.5389E-01	-4.4162E+00
6.0000E+01	-2.4995E-01	-4.1617E+00
6.1000E+01	-1.2132E-01	-3.8966E+00
6.2000E+01	1.1080E-01	-3.2841E+00
6.3000E+01	2.9155E-01	-2.5046E+00
6.4000E+01	-7.6968E-02	-1.5848E+00
6.5000E+01	-6.3174E-01	-1.0193E+00
6.6000E+01	8.5000E-01	-0.4780E+00

## C.2 Sample VELSTRE.OUT File

VELSTRE.OUT  
OUTPUT FROM EFFMODEL.FOR  
W/O SAE DUST

NoSphr-CT

PARAMETERS:

C	=	.34500E+00
RP	=	.50000E-06
RF	=	.25890E-04
RHOP	=	.27230E+04
VISCA	=	.18370E-04
HF	=	.30000E-01
H	=	.70000E-03
PF	=	.31250E-02
LAM	=	.65000E-07

RUN	VEL UPSTRM	FILTER VEL	STOKES	CSTOKES	REYNOLDS
1	.12780E+01	.10148E+00	.16140E-01	.18777E-01	.15043E+02
2	.28750E+01	.22830E+00	.36309E-01	.42242E-01	.33841E+02
3	.40240E+01	.31954E+00	.50820E-01	.59124E-01	.47366E+02
4	.52660E+01	.41817E+00	.66505E-01	.77373E-01	.61985E+02
5	.60630E+01	.48146E+00	.76570E-01	.89083E-01	.71367E+02
6	.59660E+01	.47375E+00	.75345E-01	.87658E-01	.70225E+02
7	.56730E+01	.45049E+00	.71645E-01	.83353E-01	.66776E+02
8	.48590E+01	.38585E+00	.61365E-01	.71393E-01	.57195E+02
9	.35670E+01	.28325E+00	.45048E-01	.52409E-01	.41987E+02
10	.23490E+01	.18653E+00	.29666E-01	.34514E-01	.27650E+02
11	.62100E+00	.49313E-01	.78427E-02	.91243E-02	.73097E+01

12	.12976E+01	.10304E+00	.16388E-01	.19065E-01	.15274E+02
13	.29014E+01	.23040E+00	.36642E-01	.42630E-01	.34152E+02
14	.41358E+01	.32842E+00	.52232E-01	.60767E-01	.48682E+02
15	.52190E+01	.41444E+00	.65911E-01	.76682E-01	.61432E+02
16	.64688E+01	.51368E+00	.81695E-01	.95045E-01	.76143E+02
17	.65998E+01	.52408E+00	.83350E-01	.96970E-01	.77685E+02
18	.56780E+01	.45088E+00	.71708E-01	.83426E-01	.66835E+02
19	.51429E+01	.40839E+00	.64950E-01	.75564E-01	.60536E+02
20	.36363E+01	.28875E+00	.45923E-01	.53428E-01	.42802E+02
21	.20572E+01	.16336E+00	.25981E-01	.30226E-01	.24215E+02
22	.31430E+00	.24958E-01	.39693E-02	.46180E-02	.36996E+01
23	.15680E+01	.12451E+00	.19802E-01	.23038E-01	.18457E+02
24	.26350E+01	.20924E+00	.33278E-01	.38716E-01	.31016E+02
25	.40090E+01	.31835E+00	.50630E-01	.58904E-01	.47189E+02
26	.52240E+01	.41483E+00	.65975E-01	.76755E-01	.61491E+02
27	.54250E+01	.43079E+00	.68513E-01	.79709E-01	.63857E+02
28	.62110E+01	.49321E+00	.78439E-01	.91257E-01	.73109E+02
29	.52630E+01	.41793E+00	.66467E-01	.77328E-01	.61950E+02
30	.41310E+01	.32804E+00	.52171E-01	.60696E-01	.48625E+02
31	.33450E+01	.26562E+00	.42244E-01	.49148E-01	.39373E+02
32	.20970E+01	.16652E+00	.26483E-01	.30811E-01	.24683E+02
33	.38700E+00	.30731E-01	.48875E-02	.56861E-02	.45553E+01
34	.17713E+01	.14066E+00	.22370E-01	.26025E-01	.20850E+02
35	.24231E+01	.19242E+00	.30602E-01	.35602E-01	.28522E+02
36	.33800E+01	.26840E+00	.42686E-01	.49662E-01	.39785E+02
37	.46308E+01	.36773E+00	.58483E-01	.68040E-01	.54508E+02
38	.49884E+01	.39612E+00	.62999E-01	.73294E-01	.58718E+02
39	.56291E+01	.44700E+00	.71091E-01	.82708E-01	.66259E+02
40	.45722E+01	.36307E+00	.57743E-01	.67179E-01	.53819E+02
41	.34676E+01	.27536E+00	.43793E-01	.50949E-01	.40817E+02
42	.33633E+01	.26708E+00	.42476E-01	.49416E-01	.39589E+02
43	.16947E+01	.13457E+00	.21403E-01	.24900E-01	.19948E+02
44	.37320E+00	.29635E-01	.47132E-02	.54834E-02	.43929E+01
45	.12320E+01	.97832E-01	.15559E-01	.18102E-01	.14502E+02
46	.21050E+01	.16716E+00	.26584E-01	.30928E-01	.24778E+02
47	.36800E+01	.29222E+00	.46475E-01	.54070E-01	.43317E+02
48	.42520E+01	.33765E+00	.53699E-01	.62474E-01	.50050E+02
49	.48220E+01	.38291E+00	.60898E-01	.70849E-01	.56759E+02
50	.42190E+01	.33503E+00	.53282E-01	.61989E-01	.49661E+02
51	.43370E+01	.34440E+00	.54773E-01	.63723E-01	.51050E+02
52	.33320E+01	.26459E+00	.42080E-01	.48957E-01	.39220E+02
53	.26160E+01	.20773E+00	.33038E-01	.38436E-01	.30793E+02
54	.14870E+01	.11808E+00	.18780E-01	.21848E-01	.17503E+02
55	.49300E+00	.39149E-01	.62262E-02	.72436E-02	.58030E+01
56	.17145E+01	.13615E+00	.21653E-01	.25191E-01	.20181E+02
57	.22861E+01	.18154E+00	.28871E-01	.33589E-01	.26909E+02
58	.30719E+01	.24394E+00	.38795E-01	.45135E-01	.36159E+02
59	.36888E+01	.29292E+00	.46586E-01	.54199E-01	.43420E+02
60	.40519E+01	.32176E+00	.51172E-01	.59534E-01	.47694E+02
61	.42261E+01	.33559E+00	.53372E-01	.62093E-01	.49745E+02
62	.33829E+01	.26863E+00	.42723E-01	.49704E-01	.39820E+02
63	.28806E+01	.22875E+00	.36379E-01	.42324E-01	.33907E+02
64	.23981E+01	.19043E+00	.30286E-01	.35235E-01	.28228E+02
65	.14982E+01	.11897E+00	.18921E-01	.22013E-01	.17635E+02
66	.50980E+00	.40483E-01	.64383E-02	.74904E-02	.60008E+01

## C.3 Sample EFFCOMP.OUT File

EFFCOMP.OUT  
 OUTPUT FROM EFFMODEL.FOR  
 W/O SAE DUST

NoSphr-CT

## PARAMETERS:

C = .34500E+00  
 RP = .50000E-06  
 RF = .25890E-04  
 RHOP = .27230E+04  
 VISCA = .18370E-04  
 HF = .30000E-01  
 H = .70000E-03  
 PF = .31250E-02  
 LAM = .65000E-07

RUN	INTERCEPT	INERTIAL	ADHESIVE
1	.24619E-02	.37225E-04	.99778E+00
2	.24619E-02	.42155E-03	.99333E+00
3	.24619E-02	.11484E-02	.98951E+00
4	.24619E-02	.25488E-02	.98495E+00
5	.24619E-02	.38601E-02	.98182E+00
6	.24619E-02	.36815E-02	.98221E+00
7	.24619E-02	.31745E-02	.98337E+00
8	.24619E-02	.20093E-02	.98648E+00
9	.24619E-02	.80217E-03	.99108E+00
10	.24619E-02	.23044E-03	.99493E+00
11	.24619E-02	.42750E-05	.99917E+00
12	.24619E-02	.38963E-04	.99773E+00
13	.24619E-02	.43322E-03	.99325E+00
14	.24619E-02	.12458E-02	.98912E+00
15	.24619E-02	.24822E-02	.98513E+00
16	.24619E-02	.46677E-02	.98018E+00
17	.24619E-02	.49497E-02	.97965E+00
18	.24619E-02	.31828E-02	.98335E+00
19	.24619E-02	.23768E-02	.98542E+00
20	.24619E-02	.84949E-03	.99085E+00
21	.24619E-02	.15495E-03	.99576E+00
22	.24619E-02	.55436E-06	.99967E+00
23	.24619E-02	.68707E-04	.99707E+00
24	.24619E-02	.32490E-03	.99407E+00
25	.24619E-02	.11357E-02	.98956E+00
26	.24619E-02	.24892E-02	.98511E+00
27	.24619E-02	.27827E-02	.98433E+00
28	.24619E-02	.41433E-02	.98123E+00
29	.24619E-02	.25445E-02	.98496E+00
30	.24619E-02	.12415E-02	.98913E+00
31	.24619E-02	.66236E-03	.99182E+00
32	.24619E-02	.16409E-03	.99565E+00
33	.24619E-02	.10348E-05	.99956E+00
34	.24619E-02	.98993E-04	.99654E+00
35	.24619E-02	.25287E-03	.99471E+00



36	.24619E-02	.68323E-03	.99171E+00
37	.24619E-02	.17425E-02	.98733E+00
38	.24619E-02	.21718E-02	.98600E+00
39	.24619E-02	.31027E-02	.98354E+00
40	.24619E-02	.16779E-02	.98754E+00
41	.24619E-02	.73738E-03	.99142E+00
42	.24619E-02	.67322E-03	.99176E+00
43	.24619E-02	.86716E-04	.99674E+00
44	.24619E-02	.92805E-06	.99958E+00
45	.24619E-02	.33351E-04	.99788E+00
46	.24619E-02	.16597E-03	.99563E+00
47	.24619E-02	.88025E-03	.99070E+00
48	.24619E-02	.13527E-02	.98870E+00
49	.24619E-02	.19644E-02	.98662E+00
50	.24619E-02	.13218E-02	.98882E+00
51	.24619E-02	.14346E-02	.98840E+00
52	.24619E-02	.65471E-03	.99186E+00
53	.24619E-02	.31795E-03	.99413E+00
54	.24619E-02	.58611E-04	.99727E+00
55	.24619E-02	.21392E-05	.99939E+00
56	.24619E-02	.89786E-04	.99669E+00
57	.24619E-02	.21247E-03	.99511E+00
58	.24619E-02	.51374E-03	.99271E+00
59	.24619E-02	.88653E-03	.99067E+00
60	.24619E-02	.11722E-02	.98941E+00
61	.24619E-02	.13284E-02	.98879E+00
62	.24619E-02	.68498E-03	.99170E+00
63	.24619E-02	.42401E-03	.99332E+00
64	.24619E-02	.24515E-03	.99478E+00
65	.24619E-02	.59944E-04	.99724E+00
66	.24619E-02	.23654E-05	.99936E+00

#### C.4 Sample SINGELEM.OUT File

SINGELEM.OUT  
OUTPUT FROM EFFMODEL.FOR  
W/O SAE DUST

NoSphr-CT

PARAMETERS:

C	=	.34500E+00
RP	=	.50000E-06
RF	=	.25890E-04
RHOP	=	.27230E+04
VISCA	=	.18370E-04
HF	=	.30000E-01
H	=	.70000E-03
PF	=	.31250E-02
LAM	=	.65000E-07

RUN	SINGLE	SING w/ ADH	ELEMENTAL	ELEM w/ ADH
1	.24991E-02	.24935E-02	.22402E-01	.22353E-01
2	.28825E-02	.28632E-02	.25794E-01	.25625E-01
3	.36075E-02	.35696E-02	.32177E-01	.31845E-01
4	.50045E-02	.49291E-02	.44357E-01	.43704E-01
5	.63126E-02	.61978E-02	.55624E-01	.54641E-01
6	.61344E-02	.60252E-02	.54097E-01	.53161E-01
7	.56287E-02	.55351E-02	.49750E-01	.48943E-01
8	.44663E-02	.44059E-02	.39683E-01	.39158E-01
9	.32621E-02	.32330E-02	.29142E-01	.28886E-01
10	.26918E-02	.26782E-02	.24109E-01	.23988E-01
11	.24662E-02	.24641E-02	.22111E-01	.22093E-01
12	.25008E-02	.24951E-02	.22418E-01	.22367E-01
13	.28941E-02	.28746E-02	.25897E-01	.25725E-01
14	.37047E-02	.36644E-02	.33030E-01	.32676E-01
15	.49380E-02	.48646E-02	.43782E-01	.43145E-01
16	.71182E-02	.69771E-02	.62496E-01	.61296E-01
17	.73995E-02	.72489E-02	.64884E-01	.63607E-01
18	.56369E-02	.55430E-02	.49821E-01	.49012E-01
19	.48329E-02	.47624E-02	.42870E-01	.42258E-01
20	.33093E-02	.32790E-02	.29557E-01	.29291E-01
21	.26165E-02	.26054E-02	.23443E-01	.23344E-01
22	.24625E-02	.24617E-02	.22078E-01	.22071E-01
23	.25305E-02	.25231E-02	.22681E-01	.22615E-01
24	.27860E-02	.27695E-02	.24942E-01	.24796E-01
25	.35948E-02	.35573E-02	.32066E-01	.31737E-01
26	.49450E-02	.48714E-02	.43842E-01	.43204E-01
27	.52378E-02	.51557E-02	.46377E-01	.45667E-01
28	.65950E-02	.64712E-02	.58039E-01	.56981E-01
29	.50002E-02	.49250E-02	.44320E-01	.43668E-01
30	.37004E-02	.36602E-02	.32992E-01	.32639E-01
31	.31227E-02	.30971E-02	.27914E-01	.27689E-01
32	.26256E-02	.26142E-02	.23523E-01	.23422E-01
33	.24630E-02	.24619E-02	.22082E-01	.22073E-01
34	.25607E-02	.25518E-02	.22948E-01	.22870E-01
35	.27142E-02	.26998E-02	.24307E-01	.24180E-01
36	.31435E-02	.31174E-02	.28097E-01	.27867E-01
37	.42001E-02	.41469E-02	.37363E-01	.36899E-01
38	.46284E-02	.45636E-02	.41094E-01	.40530E-01
39	.55570E-02	.54656E-02	.49133E-01	.48344E-01
40	.41357E-02	.40842E-02	.36801E-01	.36351E-01
41	.31975E-02	.31701E-02	.28573E-01	.28331E-01
42	.31335E-02	.31077E-02	.28009E-01	.27782E-01
43	.25484E-02	.25401E-02	.22840E-01	.22766E-01
44	.24629E-02	.24618E-02	.22081E-01	.22072E-01
45	.24952E-02	.24899E-02	.22368E-01	.22321E-01
46	.26275E-02	.26160E-02	.23540E-01	.23438E-01
47	.33400E-02	.33090E-02	.29827E-01	.29554E-01
48	.38113E-02	.37683E-02	.33964E-01	.33587E-01
49	.44215E-02	.43623E-02	.39293E-01	.38778E-01
50	.37805E-02	.37382E-02	.33694E-01	.33323E-01
51	.38930E-02	.38478E-02	.34679E-01	.34284E-01
52	.31150E-02	.30897E-02	.27846E-01	.27623E-01
53	.27791E-02	.27628E-02	.24881E-01	.24737E-01
54	.25204E-02	.25135E-02	.22591E-01	.22530E-01
55	.24641E-02	.24626E-02	.22092E-01	.22079E-01
56	.25515E-02	.25431E-02	.22867E-01	.22792E-01
57	.26739E-02	.26608E-02	.23950E-01	.23835E-01
58	.29744E-02	.29527E-02	.26606E-01	.26415E-01
59	.33463E-02	.33151E-02	.29882E-01	.29608E-01
60	.36313E-02	.35928E-02	.32386E-01	.32048E-01
61	.37871E-02	.37446E-02	.33751E-01	.33380E-01

62	.31452E-02	.31191E-02	.28113E-01	.27882E-01
63	.28849E-02	.28656E-02	.25816E-01	.25646E-01
64	.27065E-02	.26924E-02	.24239E-01	.24114E-01
65	.25217E-02	.25148E-02	.22603E-01	.22541E-01
66	.24643E-02	.24627E-02	.22094E-01	.22080E-01

## OVERALL/TOTALS

EOV =	.38611E-01	EOVA =	.38101E-01
QCFM =	.13839E+03	UIFM =	.27055E+00
VOFM =	.34070E+01		

## C.5 Sample SAEDUST.OUT File

SAEDUST.OUT  
OUTPUT FROM EFFMODEL.FOR  
SAE FINE

NoSphr-CT

## PARAMETERS:

C	=	.34500E+00
RP	=	SAE DUST
RF	=	.25890E-04
RHOP	=	.27230E+04
VISCA	=	.18370E-04
HF	=	.30000E-01
H	=	.70000E-03
PF	=	.31250E-02
LAM	=	.65000E-07

## SAE TEST DUST DISTRIBUTION

RADIUS:	.75000E-06	.15000E-05	.25000E-05	.50000E-05
	.10000E-04	.20000E-04	.40000E-04	.10000E-03
%WIEGHT:	.27400E+00	.76000E-01	.40000E-01	.18000E+00
	.16000E+00	.18000E+00	.90000E-01	.00000E+00

RUN	OV DUST EFF	OV W/ ADH
1	.68290E+00	.60212E+00
2	.73096E+00	.55383E+00
3	.75769E+00	.53324E+00
4	.78628E+00	.52187E+00
5	.80684E+00	.52064E+00
6	.80425E+00	.52058E+00
7	.79656E+00	.52072E+00
8	.77649E+00	.52424E+00
9	.74759E+00	.54043E+00
10	.71618E+00	.56592E+00
11	.66033E+00	.63179E+00
12	.68352E+00	.60127E+00

13	.73164E+00	.55327E+00
14	.76015E+00	.53171E+00
15	.78513E+00	.52208E+00
16	.81787E+00	.52146E+00
17	.82149E+00	.52189E+00
18	.79669E+00	.52071E+00
19	.78327E+00	.52245E+00
20	.74915E+00	.53925E+00
21	.70723E+00	.57376E+00
22	.64765E+00	.64055E+00
23	.69193E+00	.59015E+00
24	.72447E+00	.55911E+00
25	.75736E+00	.53345E+00
26	.78525E+00	.52206E+00
27	.79024E+00	.52128E+00
28	.81083E+00	.52084E+00
29	.78621E+00	.52188E+00
30	.76004E+00	.53178E+00
31	.74252E+00	.54443E+00
32	.70847E+00	.57262E+00
33	.65173E+00	.64043E+00
34	.69827E+00	.58275E+00
35	.71838E+00	.56409E+00
36	.74333E+00	.54378E+00
37	.77121E+00	.52614E+00
38	.77955E+00	.52335E+00
39	.79543E+00	.52079E+00
40	.76988E+00	.52670E+00
41	.74534E+00	.54218E+00
42	.74294E+00	.54409E+00
43	.69588E+00	.58544E+00
44	.65107E+00	.64063E+00
45	.68144E+00	.60414E+00
46	.70872E+00	.57240E+00
47	.75012E+00	.53852E+00
48	.76271E+00	.53023E+00
49	.77563E+00	.52452E+00
50	.76198E+00	.53064E+00
51	.76459E+00	.52921E+00
52	.74221E+00	.54467E+00
53	.72394E+00	.55955E+00
54	.68942E+00	.59333E+00
55	.65591E+00	.63727E+00
56	.69649E+00	.58473E+00
57	.71429E+00	.56752E+00
58	.73597E+00	.54974E+00
59	.75031E+00	.53837E+00
60	.75830E+00	.53285E+00
61	.76214E+00	.53055E+00
62	.74340E+00	.54372E+00
63	.73110E+00	.55371E+00
64	.71764E+00	.56470E+00
65	.68976E+00	.59288E+00
66	.65649E+00	.63660E+00

OVERALL/TOTALS

DEOV = .76621E+00

DEOVA = .53535E+00

## APPENDIX D

## SOURCE CODE LISTING OF DATAPICK.FOR FOR DSA OUPUT

```

C
C   PICKDATA.FOR
C   THIS PROGRAM SHOULD WORK WITH ANY SERIES DATA OUTPUT FROM DSA
C   HOWEVER, DATA SERIES MUST HAVE CONSISTENT NO. OF DATA ROWS
*****
      PARAMETER (NUM=100)
      INTEGER NDATA,IROW(NUM)
      CHARACTER VNAME*18(30),FNAME*12,OUTNAME*12,DUM1*3,DUM2*3
      REAL VAL(NUM,50)
C
C   EXPLAIN INPUT
C
      WRITE (*,3000)
C
C-->INPUT FILE NAME TO READ FROM AND NUMBER OF DATA
C
      PRINT*,'INPUT DSA-SERIES FILENAME TO READ FROM '
      PRINT*,'(EX. DS01-A.001):'
      PRINT*,'MUST BE IN CURRENT DIRECTORY.'
      READ(*,2000) FNAME
      PRINT*,'INPUT DESIRED OUTPUT FILE NAME (EX. DS01-A.OUT):'
      READ(*,2000) OUTNAME
2000  FORMAT(A12)
C
C-->OPEN DATA FILE AND OUTPUT FILE
      OPEN(5,FILE=FNAME)
      OPEN(6,FILE=OUTNAME)
C
C-->INITIALIZE SOME VARIABLES
C
C-->DO LOOP TO READ INITIAL CHARACTERS
      READ (5,2001) DUM1
      READ (5,2001) DUM2
      DO 50 I=1,NUM
          READ(5,2001) VNAME(I)
          IF(VNAME(I).EQ.'END_OF_LABELS') GOTO 100
          NDATA=NDATA+1
50    CONTINUE
100   CONTINUE
      NH=(NDATA+1)/2
      DO 120 I=1,NH
          WRITE (*,2010) I, VNAME(I),(I+NH),VNAME(I+NH)
120   CONTINUE
2001  FORMAT(A18)

```

```

2010 FORMAT (I3,') ',A18,3X,I3,') '.A18)
( WRITE (*,2500)
DO 130 I=1,NDATA
  READ*, IROW(I)
  IF (IROW(I).EQ.0) GOTO 140
  IF (IROW(I).EQ.-1) GOTO 135
  NROW=NROW+1
130 CONTINUE
135 CONTINUE
DO 137 I=1,NDATA
  IROW(I)=I
137 CONTINUE
  NROW=NDATA
140 CONTINUE
  N=0
DO 150 I=1,NUM
  IF (.NOT.EOF(5)) THEN
    N=N+1
    DO 200 J=1,NDATA
      READ(5,*) VAL(I,J)
200 CONTINUE
      NRUN=NRUN+1
    END IF
150 CONTINUE
IF (NROW.GT.13) THEN
  WRITE (6,2600) (VNAME(IROW(K)), K=1,13)
  DO 500 I=1,NRUN
    WRITE (6,2400) (VAL(I,IROW(J)),J=1,13)
500 CONTINUE
    WRITE (6,*) ' '
    WRITE (6,2600) (VNAME(IROW(K)), K=14,NROW)
    DO 501 I=1,NRUN
      WRITE (6,2400) (VAL(I,IROW(J)),J=14,NROW)
501 CONTINUE
ELSE
  WRITE (6,2600) (VNAME(IROW(K)), K=1,NROW)
  DO 600 I=1,NRUN
    WRITE (6,2400) (VAL(I,IROW(J)),J=1,NROW)
600 CONTINUE
  END IF
C-->FORMAT STATEMENTS
2600 FORMAT (24(1X,A18))
2100 FORMAT (I3)
2400 FORMAT (1P,24(E12.4,7X))
2500 FORMAT (1X,/,
&' ENTER NUMBERS CORRESPONDING TO DATA DESIRED',
&'AS NUMBERED ABOVE.',
&' /,' PRESS [ENTER] AFTER EACH POINT.',/,
&' ENTER 0 WHEN DONE.',/, ' TO SELECT ALL. ENTER -1')
3000 FORMAT (/, ' THIS PROGRAM TRANSFORMS DATA FROM A DSA SERIES',/,

```

&' INTO COLUMNS OF LIKE DATA. THE SERIES DATA MUST BE',/,  
&' OF THE SAME TYPE, E.G. CHANNEL 1, CHANNEL 2,'  
&' BOTH CHANNELS',/,  
&' OR BOTH CHANNELS WITH COIN ON.',/)

END

## APPENDIX E

PRELIMINARY CALCULATIONS OF DISPLACEMENT  
AND DISTORTION OF PROBE VOLUME

## E.1 Source Code Listing of Refraction Program

```

C      Program Refraction
C      Program calculates displacement of probe volume of LDV due to
C      refraction of laser light by slanted housing wall
C      Input data:
C      t:      thickness of wall
C      thetw angle of housing w.r.t. vertical
C      thetb angle of beam w.r.t horizontal
C      Data in inches, input angles in radians
C      Variables
      OPEN (6, FILE='REFRAC.PRN')
C      INPUT DATA
      PI=4.*ATAN(1)
      WRITE (6, 1002)
      WRITE (6, 1001)
      DO 50 K=1,2
      T=(K+1)/8.
      DO 100 I=1,45,4
      THETW=FLOAT(I-1)
      *      DO 200 J=1,45,4
      *      THETB=FLOAT(J)
      THETB=5.12
      THETUA=THETB-THETW
      THETMA=THETW
      THETLA=THETW+THETB
      THETUB=180./PI*ASIN(1.0/1.5*SIN(THETUA*PI/180.))
      THETMB=180./PI*ASIN(1.0/1.5*SIN(THETMA*PI/180.))
      THETLB=180./PI*ASIN(1.0/1.5*SIN(THETLA*PI/180.))
      ALPHA=90.-THETLA+THETW
      T1=T/COS(THETLB*PI/180.)
      BL=T1*SIN((THETLA-THETLB)*PI/180.)/SIN(ALPHA*PI/180.)

```



```

IF (THETW.GT.THETB) THEN
T2=T/COS(THETUB*PI/180.)
BETA=90.-THETW+THETUA
ELSE
T2=T/COS(THETUA*PI/180.)
BETA=90.+THETW+THETUB
ENDIF
BU=T2*SIN((THETUA-THETUB)*PI/180.)/SIN(BETA*PI/180.)
IF (THETW.EQ.0) THEN
BU0=BU
BLO=BL
ENDIF

YN=0.5*(BU-BL)
XN=-0.5*(BU+BL)/TAN(THETB*PI/180.)

GAMMA=90.-THETMA+THETW

T3=T/COS(THETMB*PI/180.)
YM=(-1.)*T3*SIN((THETMA-THETMB)*PI/180.)/SIN(GAMMA*PI/180.)
XM=-0.5*(BU0+BLO)/TAN(THETB*PI/180.)

XN=XN*25400.
YN=YN*25400.
XM=XM*25400.
YM=YM*25400.
WRITE (6, 1000) T, THETW, XN, YN, XM, YM

* 200 CONTINUE
100 CONTINUE
50 CONTINUE

1000 FORMAT (F6.3, 5X, F8.2, 5X, E10.4, 5X, E10.4, 5X, E10.4, 5X,
A E10.4)
1001 FORMAT (3X, 'THICK.', 3X, 'ANG. HOUS.', 4X,
a 'X DISPLAC.', 3X, 'Y DISPLAC.', 3X, 'X DISPLAC.',
b 3X, 'Y DISPLAC.')
```

```
1002 FORMAT (33X, 'VERT. BEAM', 10X, 'HORIZ. BEAM')
```

```
END
```

## E.2 Plots of Probe Volume Displacement

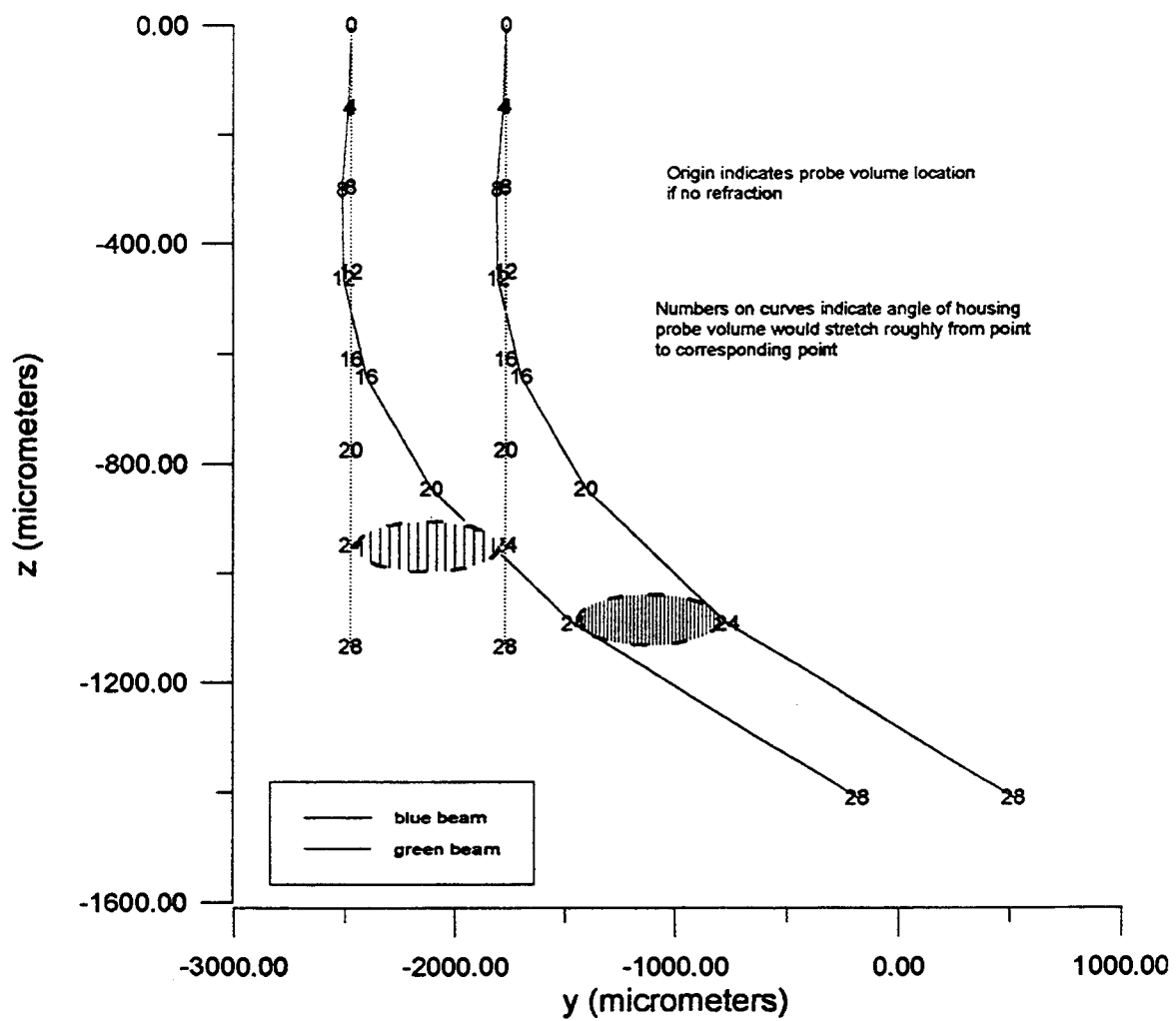


Figure E.1 Probe Volume Displacement for Axial (Blue) and Transverse (Green) Beams for a 6.4 mm (0.25 in.) Plexiglas with Varying Housing Angle

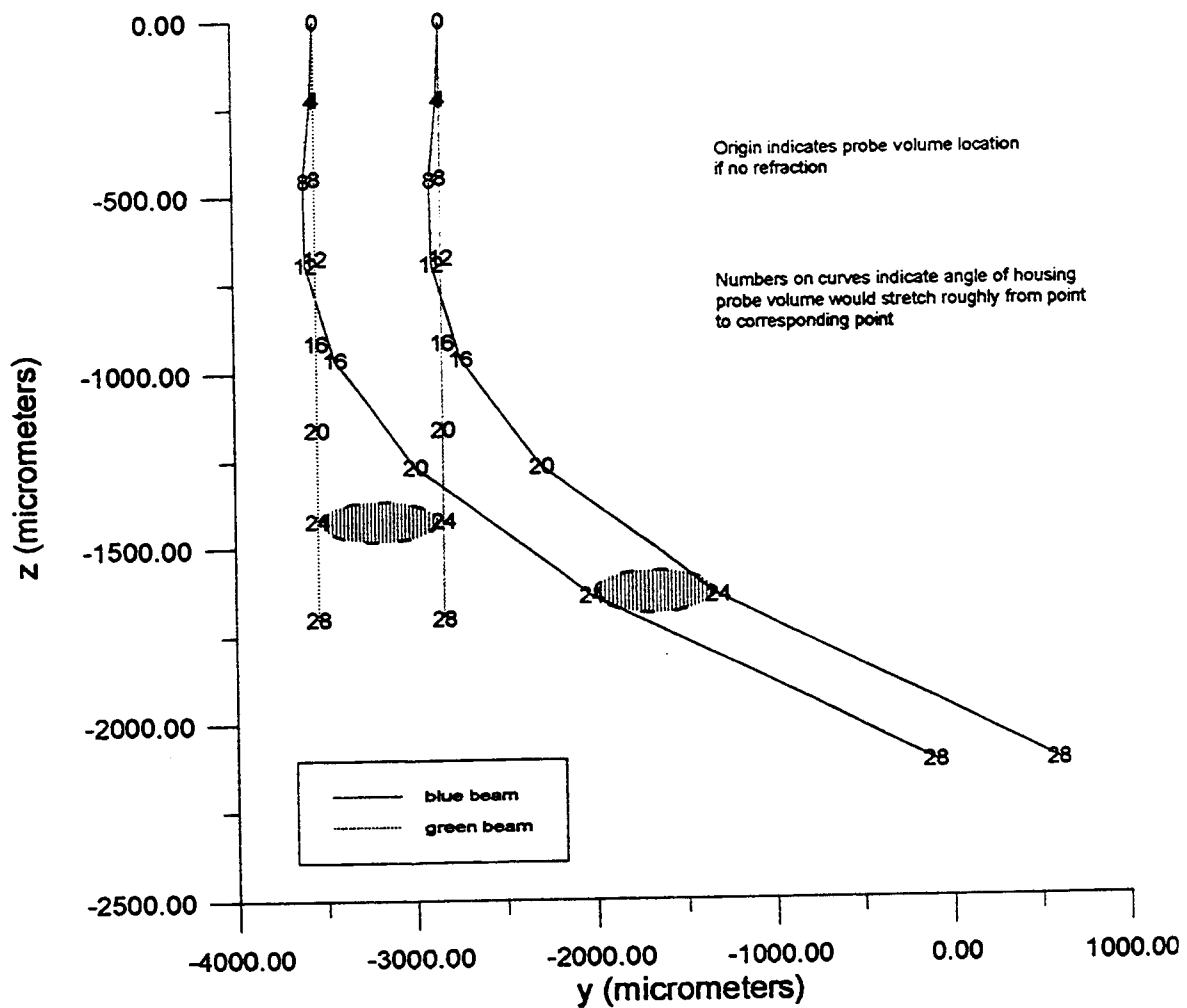


Figure E.2 Probe Volume Displacement for Axial (Blue) and Transverse (Green) Beams for a 9.5 mm (0.375 in.) Plexiglas with Varying Housing Angle

## APPENDIX F

### SMOKE GENERATOR

#### F.1 Smoke Generator Apparatus

Intermittent smoke is commonly introduced into a flow to aid in the visualization of a flow field. The smoke generating equipment discussed here, was found to be an effective system for smoke flow visualizations using an axial or transverse laser sheet. Intermittent smoke can be produced of constant denseness for a maximum of 15 second. This Appendix was adapted and revised from Wang (1990). A schematic of the smoke generator apparatus is provided in Figure F.1. Procedures in generating smoke are outlined and provided as a step process in Section F.2. The components of the smoke generator are as follows:

Compressed Gas Cylinder: A supply of non-flammable compressed gas must be supplied to the smoke chamber. This compressed gas is used to pressurize the smoke chamber allowing for controlled smoke injection into the flow stream. NO<sub>2</sub> cylinders were used in all flow visualizations presented within this paper. CO<sub>2</sub> cylinders have been used on previous occasions. It was learned that a minimum cylinder pressure of 250 psig was required to complete the flow visualizations. The compressed gas cylinder should be equipped with a pressure adjusting screw,

shut-off valve, bottle pressure gage, and output line pressure gage.

Smoke Chamber: Smoke is generated by the electrical heating element which burns the oil supply within the smoke chamber. Surrounding the heating element is a tray filled with coarse steel wool. Variac 1 may be used to control the current to the heating element. The smoke chamber is under pressure and caution must be used to not over heat or leave the heating chamber unattended. A perforated tube running from the oil reservoir to the smoke chamber channels the needed oil supply. Note that the chamber is supplied with an oil draining exhaust.

Smoke Chamber Pressure Gage: This gage displays the pressure within the smoke chamber. The pressure within the smoke chamber may be released when ever the Smoke Discharge Valve 4 or the Chamber Exhaust Valve 3 is opened. If the oil reservoir filler plug is not fully secured leaks may be present. Throughout the flow visualizations conducted, a small pressure leak was apparent.

Oil Reservoir: The Oil Reservoir stores the aviation oil. Velocity #10 Mobil Oil was used in all smoke flow visualizations. The filler plug of this oil reservoir also serves as a dipstick. The filler plug must be securely fastened due to the fact that the smoke chamber is under pressure during operation.

Variac 1: Variac 1 is used to supply proper current to the heating element in the smoke chamber. This variac is typically set at 100 volts. For all flow visualizations presented within this thesis, Variacs 1 and 2 were bypassed for a full power supply of 120V. Although this caused both heating elements to heat up quicker and

hotter, no problems were encountered.

Variac 2: Variac 2 is used to supply proper current to the heating element of the piping insulation of the compressed gas line between the compressed gas cylinder and valve 1. Again, for all flow visualizations presented in this thesis, Variacs 1 and 2 were bypassed for a full power supply of 120V.

Valve 1 - Chamber Inlet: Regulates the chamber pressure and can control the rate at which smoke is discharged from the chamber.

Valve 2 - Oil Supply: Valve 2 regulates the oil supply. Caution must be used to avoid an over supply of oil to the smoke chamber.

Valve 3 - Chamber Exhaust: Valve 3 releases the smoke chamber pressure, exhaust smoke, and drains unburned oil.

Valve 4 - Smoke Discharge: Valve 4 regulates the discharge of the desired smoke. With use of Valve 1 - Chamber Inlet, intermittent smoke can be produced of constant denseness for a maximum of 15 second.

Valve 5 - Gas Supply: Valve 5 releases the compressed gas into the pressure line to Valve 1. The compressed gas cylinder should also be equipped with a pressure adjusting screw, shutoff valve, bottle pressure gage, and output line pressure gage.

## F.2 Procedure

- Step 1: With Valves 1, 3, and 4 fully opened to release any pressure build up within the smoke chamber, and Valves 2 and 5 fully closed, the oil reservoir may be opened and filled with Velocity #10 Mobil Oil. Once filled, the filler plug should be securely fastened.
- Step 2: After all hosing connections, compressed air lines, and power supplies are securely connected, the smoke chamber may now be warmed up. First, ensure that all five valves are closed. Open the Compressed Gas Valve 5 to pressurize the supply line to 20 psig. Slowly open Chamber Inlet Valve 1 to pressurize the smoke chamber. After chamber has reached a pressure of 10 psig, close Valve 1.
- Step 3: Set Variac 1 to 100 volts and Variac 2 to 90 volts. Turn on both variacs.
- Step 4: Allow system to warm up for a full 20 minutes. Should the chamber leak pressure, ensure that all valves, except for Valve 5, are closed. If a small leak is still present, periodically open Valve 1 to maintain a chamber pressure of 10 psig.
- Step 5: Once system is heated up, open Valve 1 until the chamber pressure gauge reads 20 psig.
- Step 6: Slowly open Valve 2 approximately one quarter of a clockwise turn for a continuous oil supply to the chamber. Allow system to heat up for a full 5 minutes.
- Step 7: Ensure that the discharge hose is at desired location for discharge.

Step 8: Open Valve 4. Smoke should be coming out. Adjust Valves 1 and 4 for a stable density smoke. If no smoke is visible, close Valve 4, ensure chamber pressure of 20 psig, and allow system to heat up and accumulate smoke for an additional 1 to 2 minutes.

Step 9: Ensure proper lighting. An axial and transverse laser sheet was used for all flow visualizations conducted. Laser power controller was set at a range of 0.8 Watts to over 2.0 Watts.

Step 10: Once flow visualizations are complete, turn off variacs and close all valves.

Step 11: Allow system to cool.

Step 12: Ensure oil pan is properly positioned. Open Valve 3 to discharge excess smoke and drain unburned oil. Oil will be hot. Finally, open Valves 1 and 4. It may be necessary to drain oil build up in the discharge tubing connected to Valve 4. If this is the case, too much oil was supplied to the smoke chamber, adjust Step 6 as necessary.



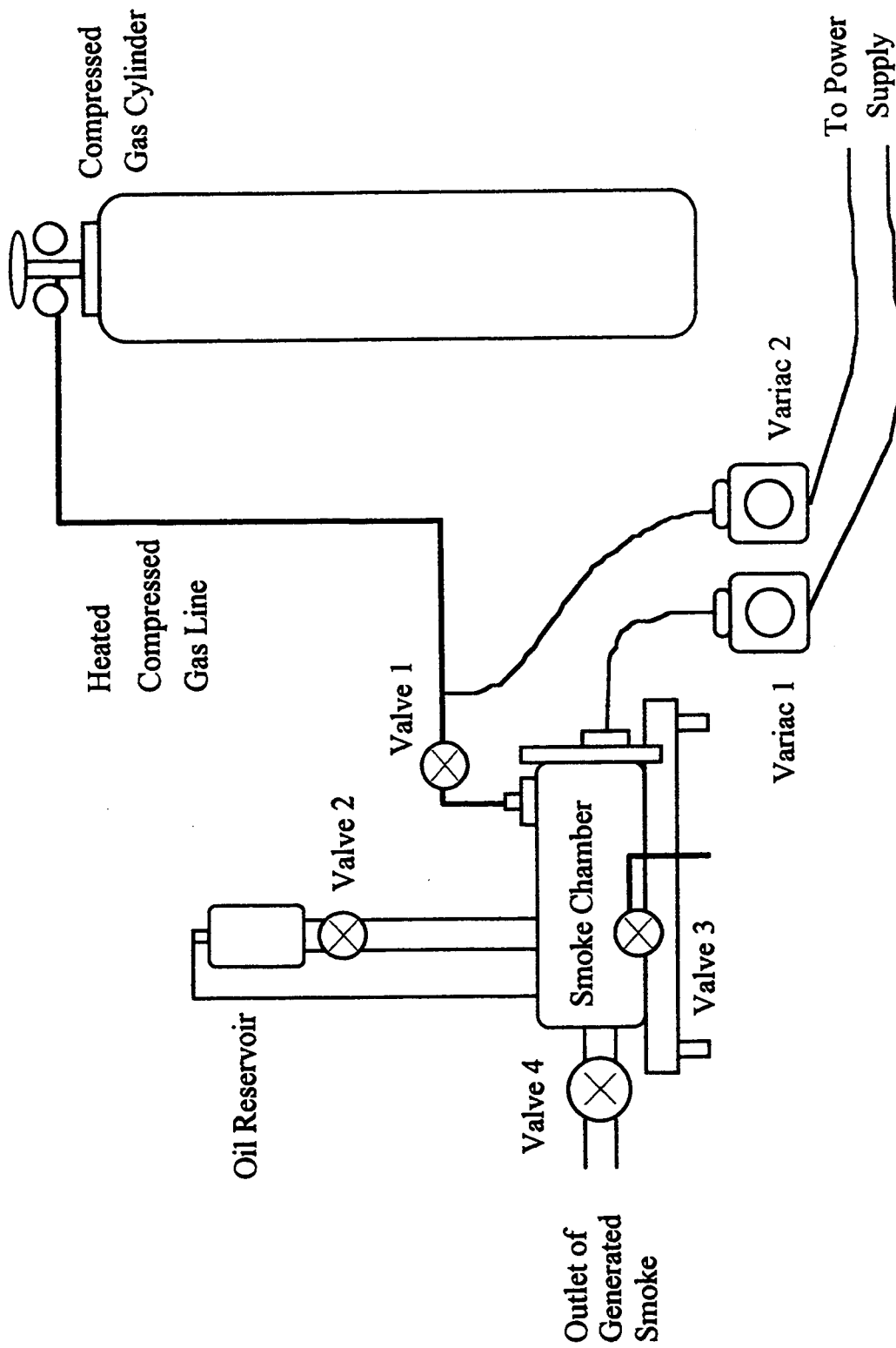


Figure F.1 Schematic of the Smoke Generator

## VITA

Robert Duran

Candidate for the Degree of

Master of Science

Thesis: IMPROVEMENT OF FLOW UNIFORMITY AND MODELING OF  
FILTRATION EFFICIENCIES FOR AUTOMOTIVE AIR FILTER TEST  
HOUSINGS

Major Field: Mechanical Engineering

### Biographical:

Personal Data: Born in Dallas, Texas, on October 4, 1969, the son of Felipe and Felicitas Duran.

Education: Graduated from W.T. White High School, Dallas, Texas in June 1988; received Bachelor of Science degree in Mechanical Engineering from the University of Texas, Austin, Texas in May 1993. Completed the requirements for the Master of Science Degree with a major in Mechanical Engineering at Oklahoma State University in July 1995.

Experience: Employed by The Dow Chemical Company, Plaquimine, Louisiana, from June 1995 to present as a mechanical engineer in the project engineering technical support group; employed by Oklahoma State University from August 1993 to June 1995 as a graduate research assistant and teaching assistant; employed by The Dow Chemical Company, Freeport, Texas, summer 1994; employed by the Texaco Chemical Company, Port Arthur, Texas, summer 1993; employed by the University of Texas, Austin, Texas from August 1990 to May 1993 as an undergraduate research assistant and an undergraduate grader within the Center of Energy Studies - Combustions Group and the ME Thermal/Fluids Division, respectively; employed by James Avery Craftsman Inc., summer 1990.

Professional Membership: Professional Engineer-In-Training, Society of Hispanic Professional Engineers, American Society of Mechanical Engineers, and the Society of Automotive Engineers